UNIVERSITY OF SOUTHAMPTON

Dusty Winds in AGN

by

Marta Venanzi

A thesis submitted in partial fulfillment for the degree of Doctor of Philosophy

in the

Faculty of Engineering, Science and Mathematics
School of Electronics and Computer Science

July 2021

Contents

List of Figures

List of Tables

Nomenclature

Physics Constants

G	Newtonian gravitational constant	6.6743×10^{-8} cm^3 g^{-1} s^{-2}
c	Speed of light (in vacuum)	$2.99792458 \times 10^{10}$ cm s^{-1}
σ	Stefan-Boltzmann constant	5.6704×10^{-5} g s^{-3} K^{-4}
h	Planck's constant	6.6261×10^{-27} cm^2 g s^{-1}
m$_p$	proton mass	1.6726×10^{-24} g
erg	erg (unit of energy)	1 cm^2 g s^{-2}

Astronomical Quantities

au	astronomical unit	$1.495978707 \times 10^{13}$ cm
pc	parsec	$3.0856775807 \times 10^{18}$ cm
yr	year	3.156×10^{7} s
$M_\odot$	Solar mass	1.98892×10^{33} g
$L_\odot$	Solar luminosity	3.839×10^{33} erg s^{-1}

Declaration of Authorship

I declare that this thesis and the work presented in it is my own and has been generated by me as the result of my own original research.

I confirm that:

1. This work was done wholly or mainly while in candidature for a research degree at this University;
2. Where any part of this thesis has previously been submitted for a degree or any other qualification at this University or any other institution, this has been clearly stated;
3. Where I have consulted the published work of others, this is always clearly attributed;
4. Where I have quoted from the work of others, the source is always given. With the exception of such quotations, this thesis is entirely my own work;
5. I have acknowledged all main sources of help;
6. Where the thesis is based on work done by myself jointly with others, I have made clear exactly what was done by others and what I have contributed myself;
7. Parts of this work have been published as: Venanzi et al. (2020), Williamson et al. (2019), Williamson et al. (2020).

Signed:..... Date:.....

Acknowledgements

First and foremost, I owe sincere gratitude to my supervisor Sebastian Hönig. Seb has given me the invaluable xopportunity to undertake this research in an internationally acclaimed astronomy group under his guidance. He has always been supportive and has created the best work environment around me to pursue my research, even during the challenging times due to the COVID-19 pandemic. Special thanks go to David Williamson. David has provided me with precious insights, he encouraged me all the way and he has always been there when I needed him. Thanks both Seb and David for helping me make the most out of my PhD. I am also grateful to the member of my research group: Daniel Asmus, Triana Almeyda, Bella Boulderstone, James Leftley, Ella Guise for taking part to insightful discussions around my work. Thanks to my office mate, Philip Grylls, for all the laughs and fun time we had together. Without him my PhD wouldn't be the same. I also thank my italian friends, Alessandra Costantino and Lorenzo Zanisi, for our office coffee breaks and dinners out (and for actually appreciating coffee and pizzas). Thanks go to my acro-friend Judith Gill, for sharing the same passions and for all the weekends spent doing sport at the park. I wish to thank my former mentor Giovanni Montani, with whom I had excellent and enjoyable work experiences prior to my PhD that helped me become better at what I do. A very special thanks go to Luca Ridolfi for always being physically present and encouraging me during the ups and downs of my PhD journey. Finally, I would like to thank my parents Anna and Vincenzo and my brother and sister Matteo and Cecilia for their continued support and love that allowed me to do what I have made so far. To them and Luca I dedicate this thesis.

This thesis work was funded by the European Research Council Grant ERC-StG-677117 DUST-IN-THE-WIND.

To my family and Luca

Chapter 1

Introduction

"I think Nature's imagination is so much greater than man's, she's never gonna let us relax!"

Richard Phillip Feynman

1.1 Active Galactic Nuclei

A rather small portion of the galaxies observed (∼10%, e.g. Capetti (2011)) appears characterized by an outstanding luminosity in their central regions, indicating a high level of activity which cannot be explained by star formation alone. These galaxies are defined as "active" and their central regions are called Active Galactic Nuclei (AGN). It is widely accepted that accretion of matter onto a supermassive black hole at the center of its host galaxy lies at the heart of this phenomenon. While stars in a normal galaxy generate radiation in the infrared (IR), optical, and ultraviolet (UV), and less significantly in the radio and X-rays, the AGN emission is spread widely across the electromagnetic spectrum, from the radio up to gamma rays, often peaking in the UV, but with significant luminosity in the x-ray and infrared bands. The luminosity emitted from AGNs range from about 10^{40} to more than 10^{47} erg s^{-1} and can vary up to a factor of 10 percents on timescales ranging from hours to years.

The investigation of these objects began in the 1940s when Carl Seyfert found out that a handful of spiral galaxies possessed extremely bright, starlike nuclei compared to normal galaxies and that their optical spectra showed the presence of broad emission lines of highly ionized species (Seyfert, 1943). These properties became the defining characteristics of the class of objects we now call Seyfert galaxies, which is one of the largest groups of active galaxies, along with quasars. Seyfert galaxies have typical luminosity $L_{bol} \sim 10^{42} - 10^{44}$ erg s^{-1} and are observed in nearby ($z \leq 0.1$) galaxies. The relatively low luminosity allows the host galaxy, typically spiral or lenticular galaxies (Weedman, 1977), to remain visible. Hence Seyfert galaxies appear like a normal galaxy with a bright, central, point-like core. Since the work of Khachikian and Weedman (1974) Seyfert galaxies are divided into two groups (see figure 1.1):

Seyfert 1 galaxies show two sets of emission lines in their spectra: broad permitted lines with (FWHM[1] $\geq$ 1000 km s^{-1}) and narrower forbidden lines (FWHM $<$ 1000 km s^{-1}). Their spectra are characterised by a distinct, nonstellar optical and UV continua.

Seyfert 2 galaxies contain narrow permitted and forbidden lines, and their optical and UV continua are dominated by the host galaxy, though through spectral polarimetry of Seyfert 2s, broad permitted lines and nonstellar continua have been detected in polarized light (Antonucci and Miller, 1985).

Intermediate types between Seyfert I and Seyfert II are possible, such as Type 1.5 Seyfert, which can be defined based on the relative strength of the broad and narrow lines (Osterbrock, 1981). The development of radio astronomy in the 1950s revealed new classes of strong energetic phenomena. The first radio maps allowed to resolve large-scales structure, such as lobes and jets, in radio galaxies, which are types of AGNs very luminous at radio wavelengths ($\sim 10^{44} - 10^{45}$ erg s^{-1} between 10 MHz and 100 GHz (Fanaroff and Riley, 1974)). A key discovery was the detection of quasars (Schmidt, 1963). Their name is a contraction for the term "quasi-stellar radio source" because at that time they could not be identified with known classes of objects. Quasars show similar characteristics of Seyfert galaxies but they are even more luminous ($L_{bol} \sim 10^{44} - 10^{48}$ erg s^{-1}). Unlike Seyferts, quasars are typically found in elliptical galaxies and are so bright that they outshine the entire galaxy. Typically, the luminosity of quasars varies

[1] FWHM stands for "full width at half maximum" and is a standard way of describing the broadness of the emission lines. It is defined as the width of a line shape at half of its maximum amplitude.

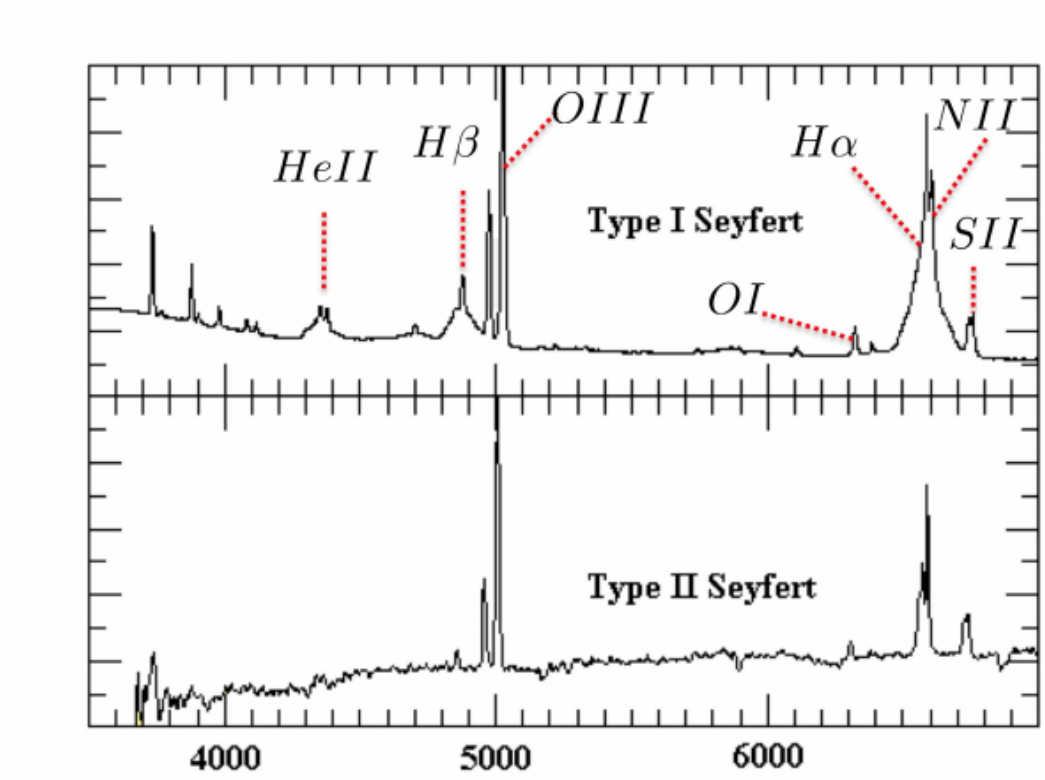

FIGURE 1.1: Optical emission lines of typical Seyfert galaxies: in the upper panel is shown the type I Seyfert galaxy NGC 4151 with broad emission lines (HeII, Hα, Hβ) and narrow forbidden lines (OI, OIII and NII).

on timescales of only a week, while Seyfert on timescales of less than a month (e.g. Gaskell and Klimek, 2003). Quasars are currently among the most powerful and distant source observed, detected up to a redshift of z=7.54 (Bañados et al., 2018).

As we can already see, there is a large number of ways an AGN can manifest itself. However, one can outline some important common properties which justify the identification of these objects as AGN: extremely bright and point-like nuclei with luminosity comparable or greater than the host galaxy; variability on timescales ranging from minutes upwards; highly ionized gas associated to broad emission lines (up to few thousands of km s^{-1}); occasional extended radio lobes and jets. It is important to note that not all these features are seen in all objects, either because of orientation effects (such as the observer's line of sight) or intrinsic differences in the sources (see section 1.5).

1.2 The central engine

The enormous luminosities observed in quasars indicated that the power source in AGN could not be ordinary stars. In addition, short time scales variability observed in the luminosity curves implies that the primary source of energy is a compact object, rather than a cluster of stars[2]. As an alternative to nuclear fusion in stars, an even more efficient way to power a large luminosity is the gravitational accretion of matter, in particular onto black holes. Accretion of matter onto a supermassive ($M \geq 10^6 M_\odot$) black hole (SMBH) can release 10% of its rest mass in radiation (Lynden-Bell, 1969), if that mass forms a thin accretion disk around the SMBH (Shakura and Sunyaev, 1973). Calculations of the mass-to-energy conversion efficiency are based on the following concepts. The luminosity of an accreting black hole is proportional to the rate at which it is gaining mass

$$L = \eta \dot{M} c^2 \tag{1.1}$$

where η denotes the efficiency of the accretion process. The amount of energy released if a mass m of gas is allowed to drop onto the compact object, starting at infinity, is

$$E = \frac{GMm}{R}. \tag{1.2}$$

In terms of the luminosity

$$L = \frac{dE}{dt} = \frac{GM\dot{M}}{R}. \tag{1.3}$$

Using equation 1.1 and 1.3 one can express the efficiency as

$$\eta = GM/(Rc^2) = R_s/2R, \tag{1.4}$$

where $R_s = 2GM/c^2$ is the Schwarzschild radius. Formally, this radius is called the event horizon because it is the furthest distance that a photon starting inside R_s can reach. By comparison, the mass-energy conversion in the thermonuclear fusion of hydrogen to helium operates with an efficiency of 0.007. Thus, accretion onto a compact object with

[2] Causality implies that an object that varies rapidly in time Δt must be smaller than the light-crossing time of the object, i.e. $R_{max} \sim c\Delta t$ (where c is the speed of light) and thus must be spatially small; if not, the variation would appear smoothed. Hence, if a quasar's luminosity varies on timescales of a hour, $R_{max} \sim 10\ au$.

$R \lesssim 70R_s$ is a more efficient mechanism than nuclear fusion of H to He. The actual efficiency estimated for disk accretion onto a black hole is $\eta = 0.06$ for a Schwarzschild black hole and $\eta = 0.42$ for a rotating (Kerr) black hole (Novikov and Thorne, 1973). A value of $\eta = 0.1$ is usually assumed. In this case, the mass flow needed to sustain a quasar with $L \sim 10^{46}$ erg s^{-1} is $\dot{M} \sim 2\ M_\odot$ yr^{-1}.

There is a minimum mass needed to produce the observed luminosity. Suppose that the gas around the back consists of ionized hydrogen and the accretion is spherically symmetric. At distance r, the outward radial force on a single electron is

$$F_{rad} = \frac{L\sigma_T}{4\pi r^2 c}, \tag{1.5}$$

where L is the luminosity of the central compact object and σ_T is Thomson cross section of the electron. As each electron moves outward, it drags a proton along with it in order to conserve charge neutrality. The inward force due to gravity on the electron - proton pair is

$$F_{grav} = \frac{GMm_p}{r^2}. \tag{1.6}$$

Setting $F_{rad} = F_{grav}$ and soving for L gives

$$L_{Edd} = \frac{4\pi GMm_p c}{\sigma_T} = 1.26 \times 10^{38} \left(\frac{M}{M_\odot}\right) \text{erg s}^{-1}, \tag{1.7}$$

which is known as the Eddington limit. This is an upper limit of the luminosity of a black hole of mass M, which is powered by spherical accretion of gas. Note that this is only an estimate. The calculation assumes that the accreting material is ionized hydrogen (good assumption) and the black hole is accreting uniformly from all directions (which is a less good assumption). The Eddington luminosity may be exceeded, if for example accretion has a preferential direction and the resulting radiation emerges anisotropically. However, it remains an important reference point for describing accretion processes. The Eddington limit is used to define the so-called Eddington ratio as

$$\lambda_{Edd} = \frac{L}{L_{Edd}} \tag{1.8}$$

which is an important parameter to describe AGN activity. One can invert the argument in eq. 1.7 and find the minimum mass that is needed to balance or overcome the radiation pressure. This gives the following lower limit of the mass

$$M_{Edd} = 8 \times 10^5 \left(\frac{L}{10^{44} \text{ erg s}^{-1}} \right) M_\odot. \tag{1.9}$$

A luminous Seyfert galaxy has $L \sim 10^{44}$ erg s^{-1}, implying that the black hole mass must be at least $\sim 10^6 M_\odot$. For a typical quasar luminosity, $L \sim 10^{46}$ erg s^{-1}, so that $M > M_{Edd} \sim 10^8 M_\odot$. This explains why these black holes are referred as *supermassive*. Finally, the accretion is predicted to flow through an accretion disc, because it is he most efficient process to transfer angular momentum outward and track the gas inward onto the vicinity of the black hole. If the disk pressure is not dominated by radiation, the global disk structure can be described by the optically thick geometrically thin accretion disk model of Shakura and Sunyaev (1973). This simplified representation predicts the following radial profile of the gas temperature in the disc:

$$T(r) \propto \left(\frac{M}{10^8 \ M_\odot} \right)^{-1/4} \left(\frac{\dot{M}}{\dot{M}_{Edd}} \right)^{1/4} \left(\frac{r}{R_s} \right)^{-3/4} \text{K}, \tag{1.10}$$

where $\dot{M}_{Edd}$ is the maximum threshold of the accretion rate, defined as

$$\dot{M}_{Edd} = \frac{L_{Edd}}{\eta \ c^2} \sim 2.2 \left(\frac{M}{10^8 M_\odot} \right) \left(\frac{\eta}{0.1} \right)^{-1} \ \text{M}_\odot \text{yr}^{-1}. \tag{1.11}$$

If the black hole has a mass as high as $10^8 M_\odot$ and the gas reaches the innermost last stable circular orbit ($r_{ISCO} = 3R_s$), then $T(r = 3R_s) \sim 10^5$ K. Blackbody emission at 10^5 K peaks in the optical and UV bands. Hence, the optical and UV bump observed in AGNs is generally interpreted as a superimposition of many different black body spectra, each corresponding to a given gas temperature.

1.3 Types of active galaxies

Seyfert galaxies, quasars and radio galaxies are just a few of the names appearing in the literature. Since their discovery, AGNs became an intense area of research and a

large number of classes and subclasses have been defined. Below I list the principal types of AGNs, organized according to their radio-loudness and their optical spectra, i.e., whether they show broad emission lines (Type 1), only narrow lines (Type 2), or weak or unusual line emission. The names and characteristics are summarized below and I am going to recall the ones I have already highlighted in the previous sections.

- **Radio quiet AGNs:** This class of AGNs shows very weak/no radio emission. Depending on other spectral properties they are further classified into several types such as the Seyfert galaxies, low ionization nuclear emission regions (LINERs) and quasars. Seyfert galaxies are further divided into Seyfert 1 (Sy1)/Seyfert 2 (Sy2) types depending on the presence/absence of the broad emission lines. Narrow emission lines are ubiquitous among the spectra of both types. As the name suggests, LINERs show only the weak nuclear emission line regions and show very low activity of accretion. It is not clear whether all LINERs are AGNs or not. Quasars are more distant and more luminous objects with properties similar to Seyfert.

- **Radio loud AGNs:** This type of AGNs exhibit strong radio emission associated with highly collimated bipolar jets and represents $\sim$ 15-20% of AGNs (Kellermann et al., 1986). Other spectral properties are very similar to that of the radio quiet AGNs. This class is further divided into Blazars, Fanaroff-Riley Class I (FR-I) and Fanaroff-Riley Class II (FR-II) galaxies. Blazars show an extremely short variability timescale ($\sim$ a few days) and high levels of continuum polarization. Blazars are further divided into BL Lac objects and optically violent variable (OVV) quasars, depending on if the optical/UV component is absent (BL Lac) or rapidly variable (OVV). FR-I galaxies have radio emission mostly coming from the core of the jet, while FR-II galaxies are those where the radio emission comes from large scales lobes.

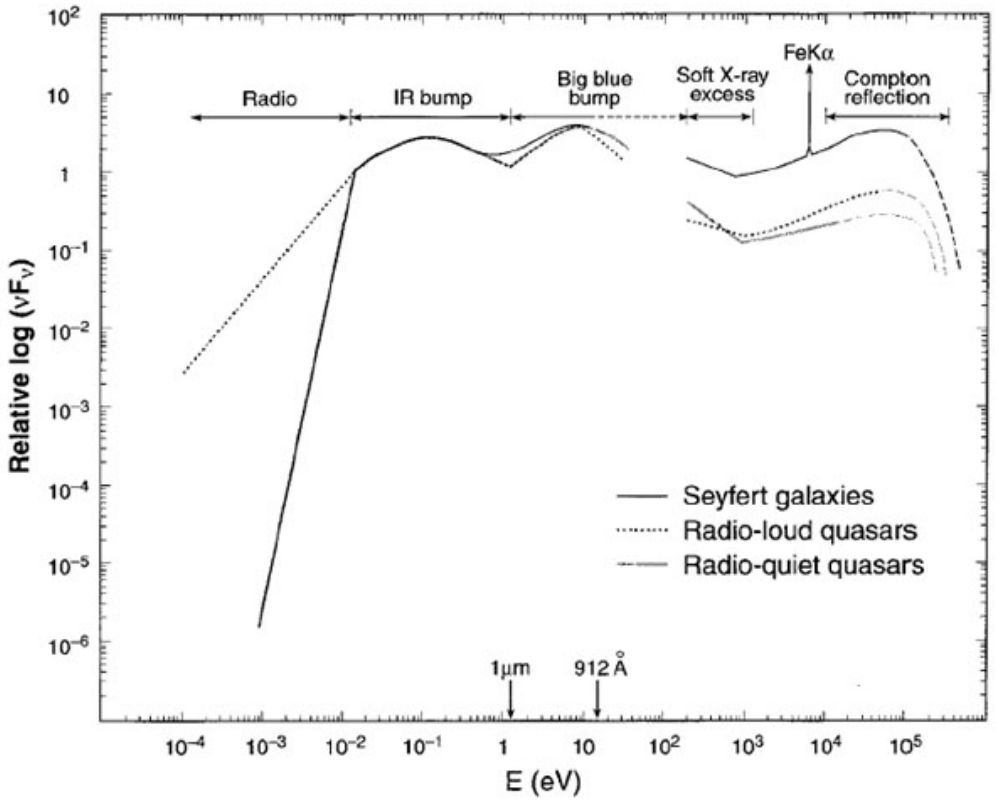

FIGURE 1.2: Schematic representation of the broadband continuum spectral energy distribution seen in the different types of AGNs. The radio-quiet spectrum can be divided into three major components: the infrared bump, which is thought to arise from reprocessing of the UV emission by dust; the big blue bump, produced by the accretion disk; and the X-ray region, which can be interpreted as the reprocessing of the "big blue bump" of the disk photons.

1.4 Spectral energy distribution of AGN

Figure 1.2 shows a schematic representation of an AGN SED from radio frequencies to hard X-rays. The spectral energy distribution (SED) of AGN can be decomposed into four main components: the primary optical/UV emission from the accretion disc, producing the "big blue bump" in the SED; the infrared radiation, due to thermal emission from the dust heated by the primary UV continuum; the high energy continuum, due to scattering and reprocessing of the optical/UV disk photons by a corona of hot electrons; the radio emission, due to synchrotron radiation, which can be relatively strong (radio-loud AGN) or weak (radio-quiet AGN). Below, the main spectral properties of AGN are described, although not all these properties are observed in all AGN.

• **Radio observations:** The radio band probes the jet emission. In the most powerful

radio sources, jets can propagate $\gtrsim$ 100 kpc and interact significantly with the circumgalactic medium (e.g. Boehringer et al., 1993). Radio loudness is one of the most common features to find AGNs with jets. The usual definition of radio-loudness is that the radio (5 GHz) to optical (B-band) flux ratio $\gtrsim$ 10. The radio spectrum takes the form of a power-law and is thought to be formed through Synchrotron radiation (ultra-relativistic electrons in a magnetic field) (Jones et al., 1974).

- **Infrared observations:** The SED is characterised by a broad infrared bump which extends from $\sim$ 1 μm to $\sim$ 100 μm, interpreted as thermal radiation dust with temperature in the range of 10-1800 K located from few up to hundreds of parsecs distance from the central UV source (e.g. Barvainis, 1987a; Sanders et al., 1990; Pier and Krolik, 1993; Asmus, 2019). The turnover at 2 μm is then naturally explained as being due to the finite sublimation temperature of dust graphite grains ($\sim$ 1500 K) (e.g. Rees et al., 1969). The fact that the IR continuum seems to vary in the same manner as the optical/UV emission, but with a time delay corresponding to the light travel-time from the UV source and IR emitting region, provides further evidence that the dust is responsible for the infrared bump (Clavel et al., 1989).

- **Optical and UV observations:** Figure 1.4 shows a typical spectrum of a type I AGNs in the optical-UV, which was generated from the Sloan Digital Sky Survey's quasar sample (Vanden Berk et al., 2001). As can be seen, the spectrum features prominent emission lines, including the Hydrogen Lyman and Balmer series as well as lines of various ionized metal species, such as MgII, CIII, CIV, OIII, etc. Near-IR observations reveal similar lines. These spectra show two different types of optical lines: broad (FWHM $>$ 1000 km s^{-1}) and narrow (FWHM $<$ 1000 km s^{-1}). It is the permitted lines (e.g., Lyα, C IV λ 1549, C III λ 1909, Mg II λ 2798, Hα, , Hβ,) which are sometimes observed to be broad, while forbidden lines (e.g., [O III] $\lambda\lambda$ 4959, 5007; [OII] λ 3727) are observed to be narrow. The line broadening is generally interpreted as Doppler shift, and thus can give an indication of the

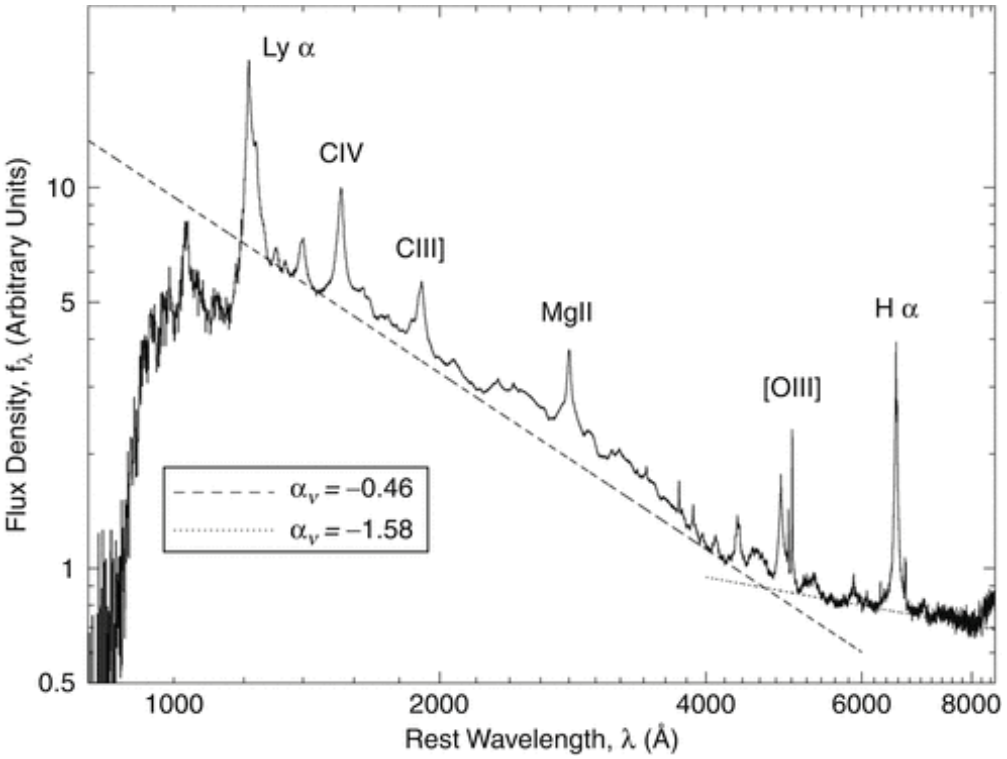

FIGURE 1.3: Figure taken from (Vanden Berk et al., 2001). Composite quasar spectrum, constructed from over 2 200 quasars in the Sloan Digital Sky Survey. The dotted line indicates the power-law fits used to estimate the continuum spectrum.

motion of the line-emitting gas. Then, the broad lines are associated with fast-moving gas close to the black hole, while narrow lines are produced in slower gas at a much greater distance. These emission lines are very different from what is typically found in normal galaxies. Figure 1.4 compares the spectrum of Seyfert 1 and 2 galaxies, as well as a LINER galaxy, a BL Lac object, broad- and narrow-line radio galaxies (BLRG and NLRG, respectively), and a normal galaxy. The discovery that NGC1068 (Antonucci and Miller, 1985) and other Seyfert 2 galaxies (Miller and Goodrich, 1990), when observed in polarized light, also show broad lines, triggered the idea of Unified Scheme of AGN (see below).

- **X-ray AND γ-ray observations:** Figure 1.5 shows an average total X-ray spectrum of a type I AGN. The main component of the x-ray spectrum is a power law with an exponential cut-off at high energies. This component is thought to be produced by Compton-up scattering of the accretion disc photons with relativistic electrons of a corona located above the disc.

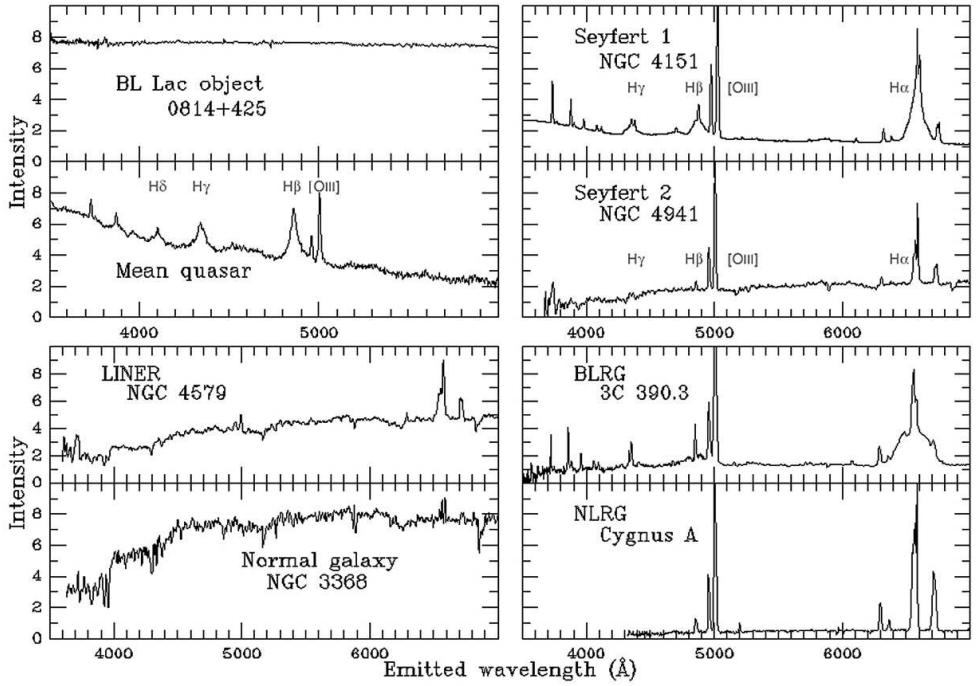

FIGURE 1.4: Optical spectrum of several different types of active galaxies as compared to a normal elliptical. Note the strong emission lines present in all types except the BL Lacs and LINERs, where they are either weaker or absent. Note also that narrow-line objects completely lack the broad lines found in Seyfert 1 or BLRG-type objects (Figure taken from Keel, http://astronomy.ua.edu/keel/agn).

Further examination reveals that considerable complexity underlies this power law. In the soft X-ray region, many objects show a "soft X-ray excess", whose origin is still unclear. The main absorption features observed in the soft X-ray spectrum are thought to be imprinted by a partially ionized plasma, called "warm absorber" (e.g., Halpern, 1984), with speeds from ~ 20 km s^{-1} to ~ 700 km s^{-1} (e.g., Kaastra et al., 2000), seen in $\sim 50\%$ of Seyfert 1 galaxies (Reynolds, 1997). Assumed to be isotropic, a fraction of the radiation produced in the corona is directed towards the disc, where it is scattered generating a secondary emission called "Compton hump" peaking around 20-40 keV (e.g. Guilbert and Rees, 1988), plus fluorescence lines, the prominent one being the Fe Kα emission line at 6.4 keV.

1.5 Unified model of AGN

Besides the large list of AGN observational properties outlined in the previous sections, it is now accepted that most of those features can be explained through a single, unified

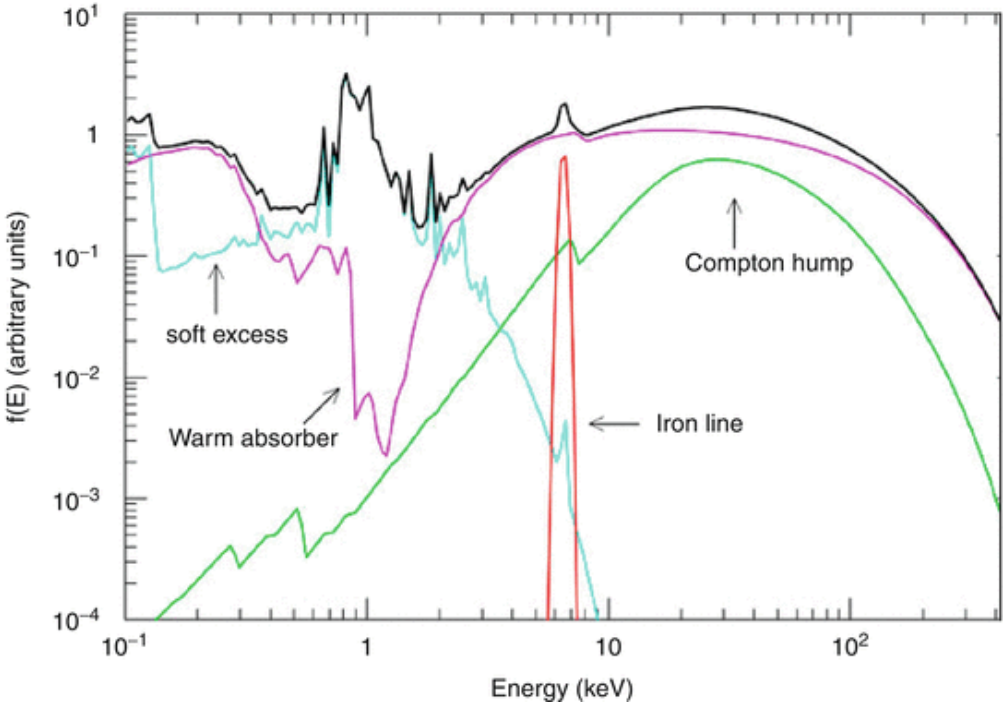

FIGURE 1.5: Average total spectrum (thick black line) and main components (thin grey lines) in the X-ray spectrum of a type I AGN. The main primary continuum component is a power law with a high energy cutoff at E $\sim$ 100-300 keV, absorbed at soft energies by a warm absorber. A cold reflection component is also shown. The most relevant narrow feature is the iron Kα emission line at 6.4 keV. Finally, a "soft excess" component is shown. (Figure taken from (Risaliti and Elvis, 2004)).

picture, which has a small number of assumptions. The basic principle of the unified model is that the underlying physical scenario of all AGNs is intrinsically similar and AGNs diversity is just a geometric effect caused by the inclination angle at which they are observed (Antonucci, 1993; Urry and Padovani, 1995, see figure 1.6). The first evidence of unification came from polarisation measurements performed on the Seyfert 2 NGC 1068 (Antonucci and Miller, 1985). The scattered light in the nuclear region revealed broad lines, like those seen ubiquitously in Seyfert 1 galaxies. The implication of this finding is the broad line emitting gas is present in both Type 1 and Type 2 Seyfert galaxies, but this fast-moving gas clouds are hidden from direct view in Type 2, and are only visible through scattering. The most plausible framework to explain this apparent suppression of broad emission lines appeared to be given by a toroidal dusty obscuring structure. This led to the idea which is known as AGN Unification. A unified structure, made up of several components, each responsible for one or more emission features, has the ability to explain the vast phenomenology observed. According to this model, all

AGNs are powered by the accretion onto a central black hole with mass between 10^6 and 10^{10} $M_\odot$. In the immediate surrounding, the conservation of angular momentum forces the gas into a geometrically thin, hot accretion disk. The gas gradually feeds the black hole by losing angular momentum via turbulent and viscous processes and part of the gravitational potential is converted to radiation. The characteristic temperature of its innermost regions is a few times 10^5 K - 10^6 K, so it emits mostly in the UV. The interaction of these UV photons with a plasma of relativistic hot electrons in the Corona, which is confined within tens of gravitational radii of the SMBH, is supposed to produce the observed X-ray emission. Above and below the accretion disk, gas clouds are rotating around the supermassive black hole. The gas is ionised by the radiation coming from the accretion disk. Assuming Keplerian motion, the clouds which are closer to the black hole have higher temperature and velocity which cause the observed broad lines, hence form the so called **Broad Line Region (BLR)**. Here, the gas density is at least 10^9 cm^{-3}, as judged from the absence of strong, broad forbidden lines (Osterbrock and Ferland, 2006)[3]. BLR gas has characteristic velocities of 3000-10000 km s^{-1}. The size of the BLR is $\sim 10^{-3} - 10^{-1}$ pc, as deduced from the broad line variability (e.g. Kaspi et al., 2000; Bentz et al., 2009). Dust cannot survive in this region due to the intense radiation. More distant clouds, located beyond the dust sublimation radius, form the **dusty torus**, an optically thick molecular structure consisting of a large mass of dust. The dust blocks and reprocess the optical and UV light coming from the central source and re-emits in the infrared. According to the classical unified model (Antonucci, 1993; Urry and Padovani, 1995), this obscuration is assumed as having a uniform, toroidal structure. This geometry has been inferred to explain the presence of scattered light from the central region, visible in polarized light in Type 2 AGNs (Antonucci and Miller, 1985). However, this toroidal configuration is by no means required, and in fact most recent spectropolarimetric studies indicate that a disk+wind geometry is equally possible (e.g. Marin and Goosmann, 2013). This obscuration region would need to be dusty and possibly molecular gas-rich, but whatever its geometry, has gained the name of "torus" in the literature (Krolik and Begelman, 1986). The dusty

[3]Forbidden lines arise when downward transitions occur from metastable energy levels in neutral or ionised atoms. In high density environments ($n_e \gtrsim 10^9$ cm^{-3}) the collisions between atoms carry away the energy before a downward transition can occur.

region is thought to intercept the isotropic emission of the accretion disk along the torus equatorial plane. The ionizing photons are therefore allowed to reach only the clouds within an **ionization cone** extended along the AGN symmetry axis on ~ 10 pc to ~ 100 pc scales. These clouds have lower densities (gas electron density $n_e \sim 10^2 - 10^6$ cm^{-3}) and lower velocities (FWHM < 1000 km s^{-1}) if compared to BLR clouds and form the so called **Narrow Line Region (NLR)**. In some AGNs, relativistic jets emerge from the central region along the disc axis, emitting synchrotron radiation. These "radio galaxies" represent roughly 10-20% of the population (Kellermann et al., 1986; Ivezić et al., 2002). The torus is responsible for the difference between narrow-line radio galaxies and broad-line radio galaxies in a manner directly analogous to the Seyfert Type I and Type 2 unification (Urry, 2003; Tadhunter, 2008). In addiction, the beaming of the jet can change the appearance of the radio galaxies. For example, in BL Lac objects the jet axis is oriented at the observer's direction giving a unique radio emission spectrum.

1.6 The dusty torus

While the term "torus" implies a specific geometry, three decades of observations have brought to the conclusion that this description is far too simplistic. Recent high angular resolution observations of local Seyfert galaxies in the infrared with the Very Large Telescope Interferometer (VLTI) made it possible to show that the parsec-scale dust distribution does not consist of a single, toroidal entity (Hönig et al., 2012, 2013; Tristram et al., 2014; Lopez-Gonzaga et al., 2014, 2017; Leftley et al., 2018). Instead, a two component model seems to be favoured with an equatorial, thin disk and a polar dusty wind in the form of a hollow cone (Hönig and Kishimoto, 2017; Stalevski et al., 2017, 2019) and possibly extending up to 100 pc (Asmus et al., 2016). The wind has the ability to collimate the AGN ionizing radiation and induce the biconical shape of the ionization cone (Tristram et al., 2014). In parallel, the Atacama Large sub-Millimeter Array (ALMA) interferometer (Gallimore et al., 2016a; Imanishi et al., 2016; García-Burillo et al., 2016; Alonso-Herrero et al., 2018, 2019; Combes et al., 2019; Impellizzeri et al., 2019) imaged the molecular phase of the torus on similar scales and probed its dynamical nature. These observations show sign of rotation, inflows, outflows or even

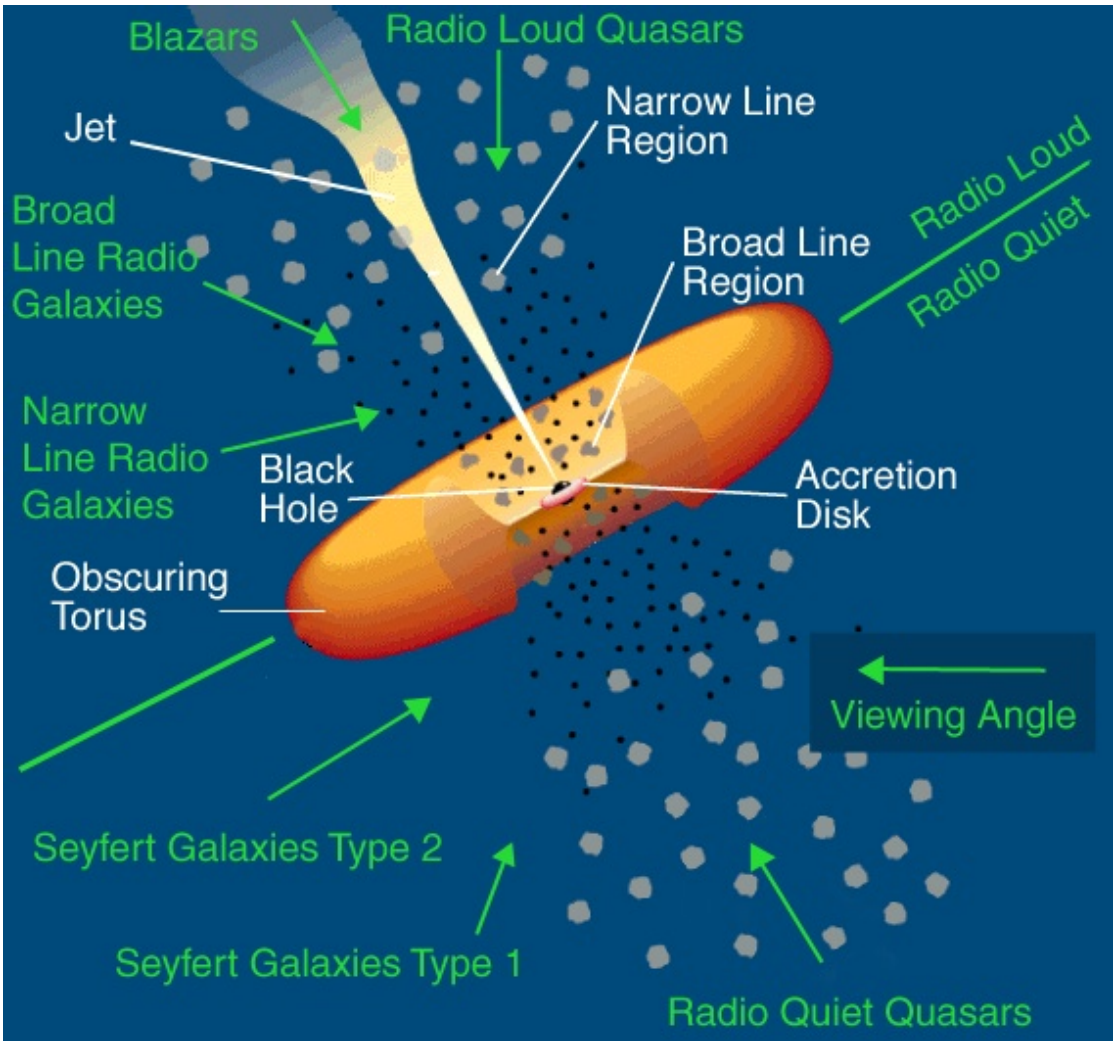

FIGURE 1.6: Schematic diagram of the AGN unification picture, not to scale, reproduced from Urry and Padovani (1995). For details, see text.

counter-rotating and misaligned disks, leaving it unclear weather or not these sb-mm data are compatible with the elongated dust shapes seen in the infrared. The study of X-ray emission in AGN also provides important information about the structure and physical properties of the torus and its contribution to AGN obscuration (for a comprehensive review of nuclear obscuration in AGN from the X-ray and infrared point of view see Ramos Almeida and Ricci, 2017b). While nuclear obscuration is mostly associated with the dusty torus, important contributions also come from dust-free gas within the BLR, suggesting that X-ray obscuration is likely produced by multiple absorbers on various spatial scales (Risaliti et al., 2007; Maiolino et al., 2010). Studies of X-ray selected AGN have shown that the parameter that drives the evolution of the covering factor of the obscuring material is the Eddington ratio (Ricci et al., 2017).

In the following, I will summarize the most relevant observations in the infrared, sub-mm and X-ray regime to finally combine them together.

1.6.1 The infrared view: the disk+wind model

About 40 nearby AGN have been observed with IR interferometry in the near-IR or mid-IR. The 4 objects that have been studied in most detail are NGC 1068 (Raban et al., 2009), NGC 424 (Hönig et al., 2012), NGC 3783 (Hönig et al., 2013), and Circinus (Tristram et al., 2014), with observations at many position angles and baseline lengths. In all four sources, the dusty emission is always found along the polar direction and accounts for 60-80% of the mid-IR emission (see figure 1.7). More recently, López-

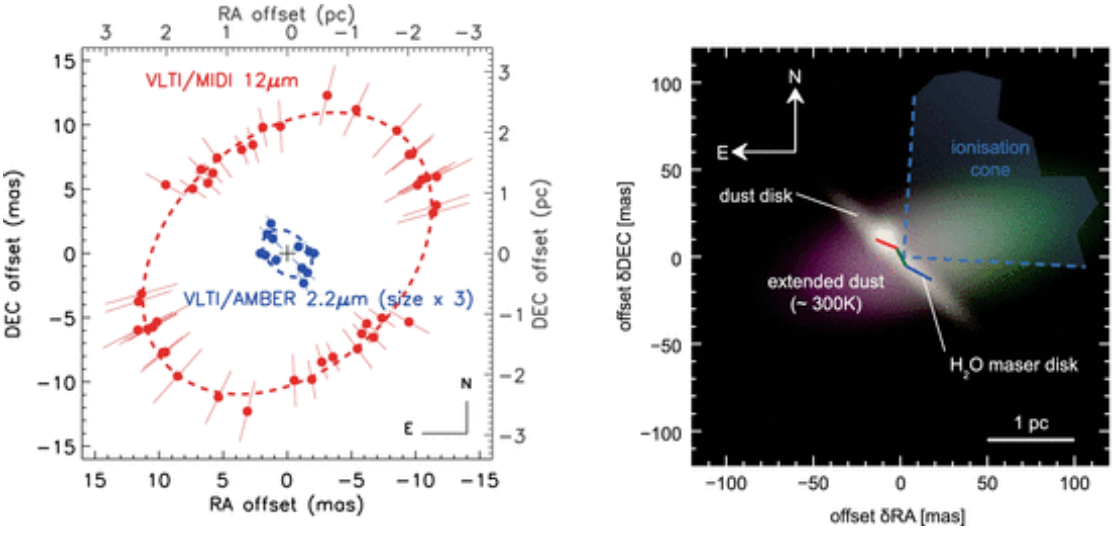

FIGURE 1.7: Left: Position-angle dependent sizes of the near-IR (blue) and mid-IR (red) emission in NGC 3783 as observed with VLTI/AMBER and VLTI/MIDI. The mid-IR ellipse is elongated toward the polar region while the near-IR emission is aligned with the plane of the AGN (Hönig et al., 2013). Right: Model image of the dusty environment in the Circinus galaxy based on the mid-IR interferometry data from (Tristram et al., 2014). Figure adapted by (Hönig, 2016).

Gonzaga et al. (2016) analyzed the mid-infrared interferometric data of 23 sources with the specific aim of detecting elongated mid-infrared emission. This feature has been found in other 3 Seyfert Type 2 galaxies: NGC 5506, NGC4507 and MCG-5-23-16, with significant polar elongation detected in NGC 5506. While one may argue that possible obscuration/extinction effects play a role in this appearance for the two Type 2 sources, this argument becomes less convincing for NGC 3783, which is a Type 1 AGN. This polar feature can be detected also in single-telescope mid-IR imaging data and has been

reported in 21 nearby AGN, with an elongation traced up to 100 pc (Asmus et al., 2016, see figure 1.8).

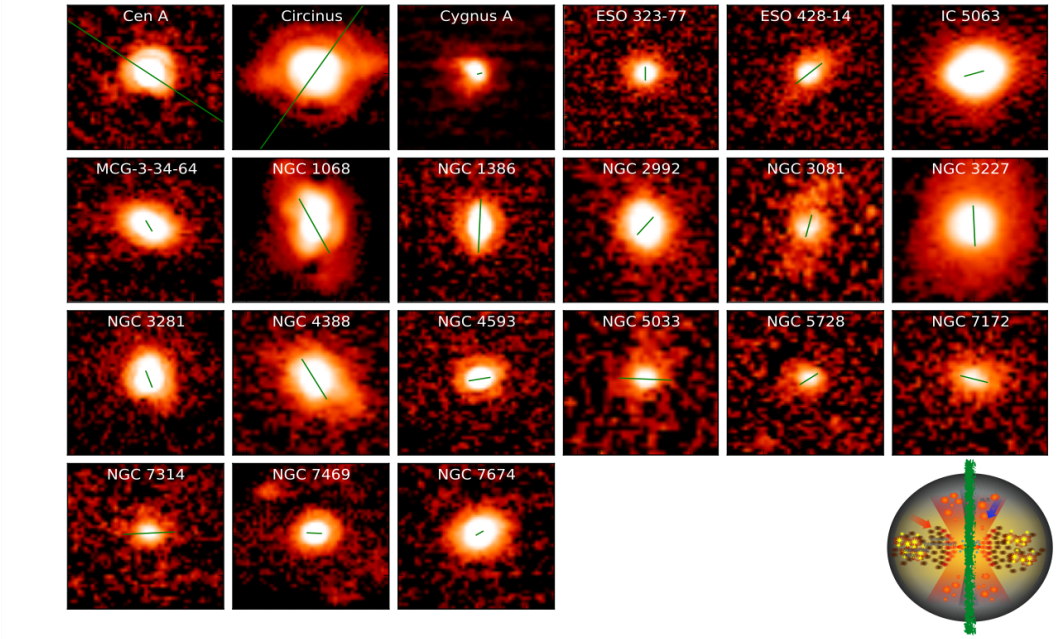

FIGURE 1.8: Nuclear MIR emission images of the MIR-extended Seyferts from Asmus et al. (2016). The green line traces the system axis.

New observational evidence suggests that polar dust is indeed not only ubiquitous in AGN but also an integral part of its structure, and its appearance is only limited by the lack of sufficient high-quality mid-infrared data (Asmus, 2019). The interferometric observations, combined with radiative transfer modelling, imply that the dusty environment consists of two separate entities: (1) a geometrically thin disc in the equatorial plane of the AGN, potentially dominating the near-IR fluxes, and (2) a cooler polar component, contributing most of the mid-IR emission, which may originate from a dusty wind forming a hollow cone and defining the edges of the narrow line region (Hönig and Kishimoto, 2017; Stalevski et al., 2017). Qualitatively, the shape of the wind is expected to be hyperbolic, as implied by detailed modelling of the Circinus galaxy (Stalevski et al., 2019, see figure 1.9). It has been suggested that the main wind driver mechanism is represented by the radiation pressure on the dust grains close to the sublimation radius (Hönig et al., 2012). Radiation-hydrodynamical simulations demonstrate that such radiation-pressure driven dusty winds are indeed viable in AGN (e.g. Dorodnitsyn et al.,

2012; Wada et al., 2016; Chan and Krolik, 2016; Williamson et al., 2019), but further work is required to support these ideas, which is the central goal of this dissertation.

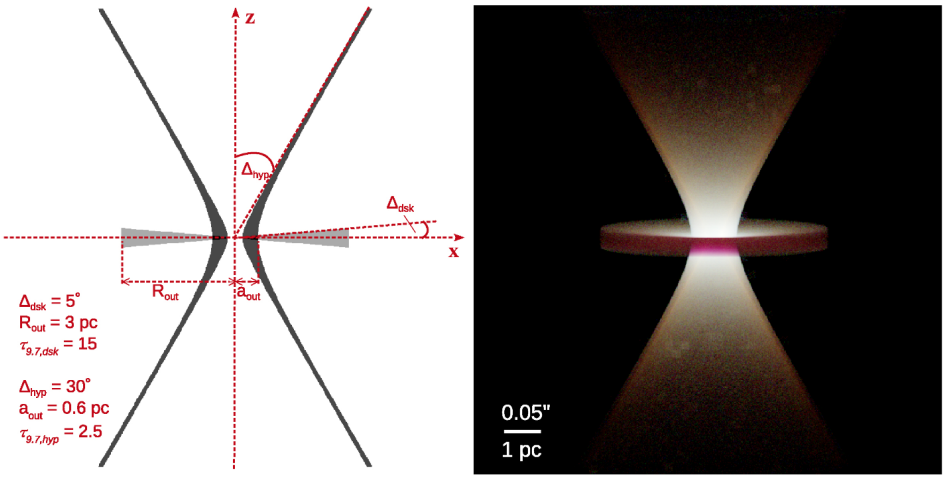

FIGURE 1.9: Left: schematic of the model geometry for Circinus, i.e. dust density cut through the xz plane: a geometrically thin dusty disc and a polar dusty wind in a form of a hyperboloid shell. The schematic and the values of the parameters correspond to the best model presented to fit the interferometric data. The dust density is constant both in the disc and in the hyperboloid. Right: a colour composite image (in logarithmic scale) of the best disc+hyperboloid model made by mapping the 8, 10, and 13 μm flux images obtained with radiative transfer simulations. Figure taken from (Stalevski et al., 2019).

1.6.2 The molecular view

The Atacama Large Millimeter Array (ALMA) can trace the molecular component of dust clouds in the submillimeter wavelength range with a spatial resolution of the order of a few to 10 pc, i.e. only slightly lower than the VLT interferometer in the IR (e.g. Combes et al., 2013, 2014; García-Burillo et al., 2014; Imanishi et al., 2016; Gallimore et al., 2016b; García-Burillo et al., 2016; Audibert et al., 2017; Imanishi et al., 2018; Alonso-Herrero et al., 2018; Combes et al., 2019; Alonso-Herrero et al., 2019). Most of these observations specifically target various rotational bands of CO, HCN, and HCO+, tracing gas densities of a few $\times 10^4$ cm^{-3} up to 10^6 cm^{-3}. Figure 1.10 is taken from the work of García-Burillo et al. (2016) and presents the images obtained of the dust continuum and molecular gas from the 300 pc-sized circumnuclear disk of NGC 1068, with a spatial resolution of 4 pc. The full-scale kinematics observed in the molecular emission can be complex. For example, NGC 1068 reveals signs of turbulent structures in

the CO emission (García-Burillo et al., 2016) and even counter-rotating and misaligned disks in the HCN emission (Impellizzeri et al., 2019). However, these observations do

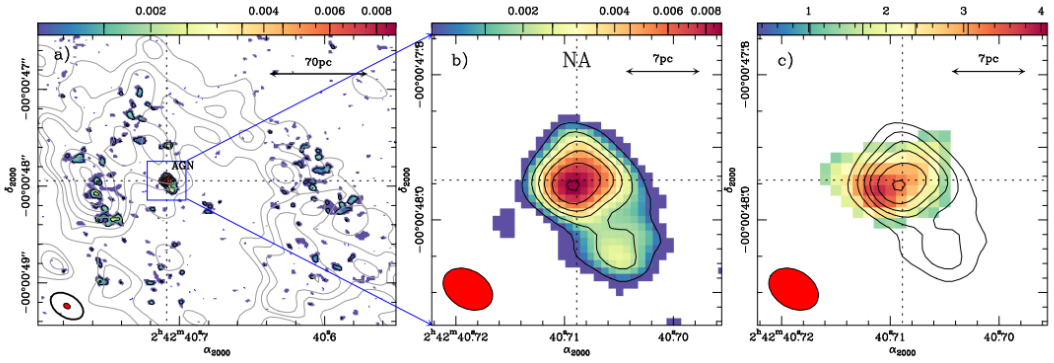

FIGURE 1.10: ALMA maps of the dust continuum and molecular gas in the nucleus of NGC 1068. (a) ALMA natural (NA)-weighted map of the dust continuum emission at 432 μm in the circumnuclear disk of NGC 1068. (b) Close-up of the dust continuum emission shown in the left panel. (c) Overlay of the continuum emission contours shown in panel (b) on the CO(6–5) emission from the torus. The red-filled ellipses at the bottom left corner of panels (b) and (c) represent the ALMA beam size at 694 GHz. The dashed lines highlight the AGN location. Figure taken from García-Burillo et al. (2016), adapted by (Ramos Almeida and Ricci, 2017a).

have in common that the inner 30-50 pc show clear rotation patterns for the bulk of the CO gas[4]. Assuming a disk in hydrostatic equilibrium, it is possible to estimate the scale-height of the CO emission in terms of the inferred rotational velocities v_{rot}, and gas velocity dispersion σ found in the literature. As shown in Hönig (2019), the typical scale-height of the CO line in those ALMA observations are $H/R \sim 0.15 - 0.3$.

Resolution at similar scales as with ALMA has been obtained also for the near-IR H_2 molecule using VLTI/SINFONI and Keck/OSIRIS. The H_2 line traces hotter gas than the CO line (1000-2000 K compared to 20-50 K). As estimated in Hönig (2019), the H_2 emission has a higher scale height than the CO lines, due to its higher observed velocity dispersion and might be due by a combination of outflow and rotation, which is difficult to disentangle. The estimated value for H_2 is $H/R \sim 1.2 - 1.4$, which, converted into covering factor[5], gives a quasi-spherical distribution. Finally, H_2O maser emission is known in NGC1068 and Circinus (e.g. Greenhill and Gwinn, 1997; McCallum et al.,

[4]As noted in (Hönig, 2019), the various rotational bands of CO are currently the ones which provide the best observational coverage across Seyfert galaxies. When comparing CO to other molecular lines, e.g. HCN, in some of the publications, the kinematics properties are similar, though the spatial distribution may vary. Hence, CO can be used as a proxy.

[5]The covering factor represents the fraction of sky covered by photoionized gas clouds, as seen from the center.

2009). These features are seen in very thin disks at much smaller, sub-pc, scales and trace very dense gas (hydrogen density $n_H > 10^9$ cm^{-3}).

1.6.3 The X-ray view

The level of low-ionization absorption in the X-rays is typically parametrized in terms of the line-of-sight column density, and AGN are considered to be obscured if $N_H \geq 10^{22}$ cm^{-2}. While obscuration strongly depletes the X-ray flux at E<10 keV, emission in the hard X-ray band (E$\gtrsim$10 keV) is less affected by obscuration (Ramos Almeida and Ricci, 2017a). Studies conducted in the hard X-ray band have shown that 70% of local AGN are obscured (Burlon et al., 2011; Ricci et al., 2015). The columns of material implied by X-ray absorption is comparable or larger than those inferred from infrared observations, suggesting that dust free gas within the BLR also participates in obscuration, although in smaller measure with respect to the dusty torus. Indeed, it is likely that X-ray obscuration is produced by multiple absorbers located at different distances from the AGN (e.g. Risaliti et al., 2007; Maiolino et al., 2010). The evolution of the covering factor of the obscuring material has been long debated (Elitzur and Shlosman, 2006; Merloni et al., 2014). In the X-ray the covering factor can be estimated using a statistical argument and studying a large sample of AGN. In fact, the probability of seeing an AGN as obscured is proportional to the covering factor of the gas and dust. Studying a large sample of objects within a certain column density range allows us to obtain the corresponding average covering factor for that specific N_H interval. Studies of a large and complete sample of accreting black holes, with additional information on gas column density, luminosity and mass have shown that the evolution of the covering factor strongly depends on the Eddington ratio (Ricci et al., 2017, see figure 1.11). In particular, the fraction of obscured Compton thin ($N_H = 10^{22} - 10^{24}$ cm^{-2}) sources decreases with Eddington ratio. On the other hand, Compton thick ($N_H > 10^{24}$ cm^{-2}) material does not follow the same trend and remains constant. Figure 1.11 shows that AGN can typically be dived in two types: AGN with $\lambda_{Edd} < 10^{-1.5}$ have obscurers with a large covering factor (about 85%), whereas those with $\lambda_{Edd} > 10^{-1.5}$ have outflowing

material and a smaller covering factor (about 40%), half of which is associated with Compton-thick material.

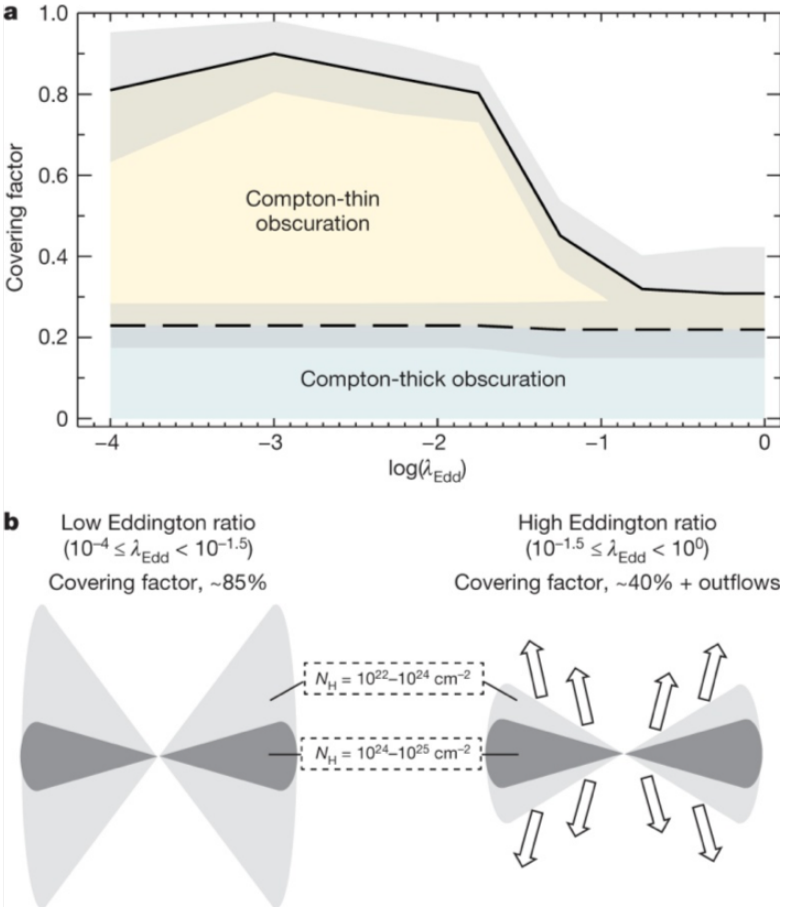

FIGURE 1.11: **a**. Relation between the covering factor of the circumnuclear material and the Eddington ratio. **b** Schematic representation of the material surrounding supermassive black holes for different ranges of the Eddington ratio. Figure taken from Ricci et al. (2017).

1.6.4 A unified view of the torus in the infrared, sub-mm and X-ray

The previous sections demonstrated that different structures emerge from multiwavelengths observations of the torus at the (sub-)parsec scales and tens of parsec scales. Molecular lines show large, massive disks while mid-IR observations show a strong polar component, which is interpreted as a dusty wind. On the base of general physical principles, Hönig (2019) proposed a unifying picture putting together the observed sub-mm and IR properties shared by AGN. Figure 1.12 has been taken from his paper and shows a schematic of the observed phases plotted on top of each other. The arrows denote

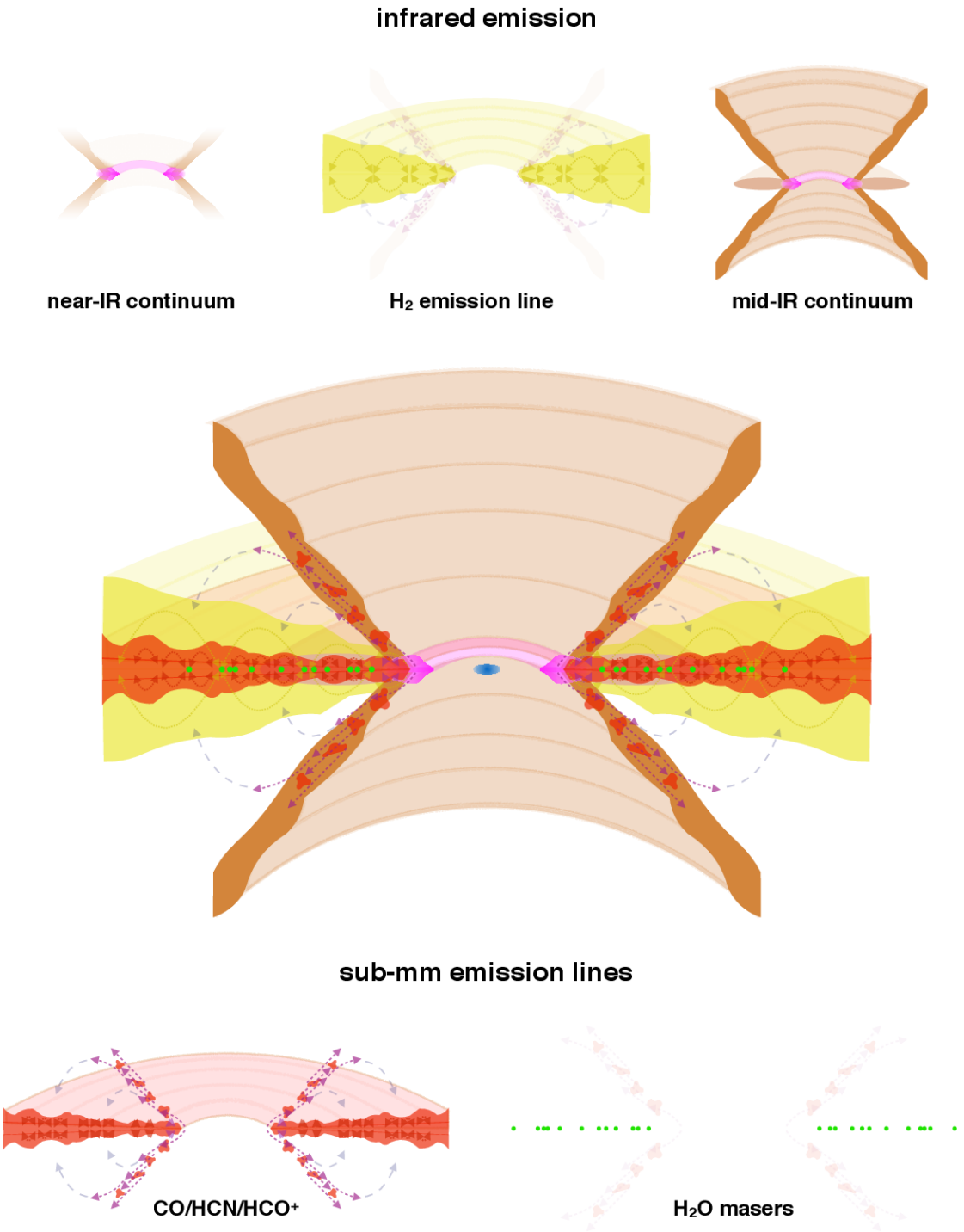

FIGURE 1.12: Schematic view of the multi-phase dusty molecular environment of an AGN. The central picture has all empirically identified components plotted on top of each other. The top row shows those components of the multi-phase structure that can be detected by IR continuum observations (top left: near-IR, top right: mid-IR) and near-IR H2 emission lines (top-middle panel). The bottom row shows the view in commonly observed sub-mm molecular lines (bottom-left) as well as by the H_2O maser emission. The arrows indicate the kinematics of the respective emission lines (without the rotational component). Figure taken from Hönig (2019).

the dynamics of the respective component, combining the observed kinematics and theoretical expectations. Two-sided arrows indicate turbulent motion, either due to cloud scattering, thermal processes, or IR radiation pressure, while single-sided arrows mark wind/outflow motion primarily due to AGN radiation pressure. Including the results obtained in the X-ray, the major conclusions about the nature of the torus from an observational point of view can be summarized as follows:

- Dusty molecular gas flows in from galactic scales of 100 pc to the sub-pc environment via a disk with small to moderate scale height. Higher density gas in the radial direction is observed closer to the AGN and in the vertical direction closer towards the mid-plane.

- The hot, inner part of the disk inflates due to IR radiation pressure and unbinds gas with hydrogen column densities $N_H \lesssim 10^{22}$ -10^{23} cm^{-2} which is in turn swept out in a dusty wind by radiation pressure from the AGN.

- The dusty wind feeds back mass into the galaxy at a rate of the order of 0.1-100 $M_\odot$ depending on AGN luminosity and Eddington ratio.

- Angle-dependent obscuration as required by AGN unification is provided by a combination of disk, wind, and wind launching region.

- The distribution of the bulk of the obscuring dust and gas is ultimately regulated by the Eddington ratio: material with column density values $N_H = 10^{22} - 10^{24}$ cm^{-2} is mostly found in form of outflows and its covering factor decreases with Eddington ratio, while a Compton-thick ($N_H > 10^{24}$ cm^{-2}) obscuration is always present and associated with a small covering factor.

1.7 Dynamical torus models

The observational evidence that dusty winds contribute to defining the obscuration properties of AGNs has motivated a number of radiative hydrodynamic (RHD) simulations, with a particular focus on the role of radiation pressure (e.g. Dorodnitsyn et al., 2012; Wada et al., 2016; Chan and Krolik, 2016; Namekata and Umemura, 2016; Chan and Krolik, 2017; Williamson et al., 2019, 2020). The general consensus is that outflows naturally emerge in the dusty environment of AGN and are driven by radiation pressure (either UV or re-radiated IR). X-ray heating and supernovae can contribute to this simulated outflow (Wada et al., 2016). However, the approaches behind those models are very different and produce a variety of wind scenarios.

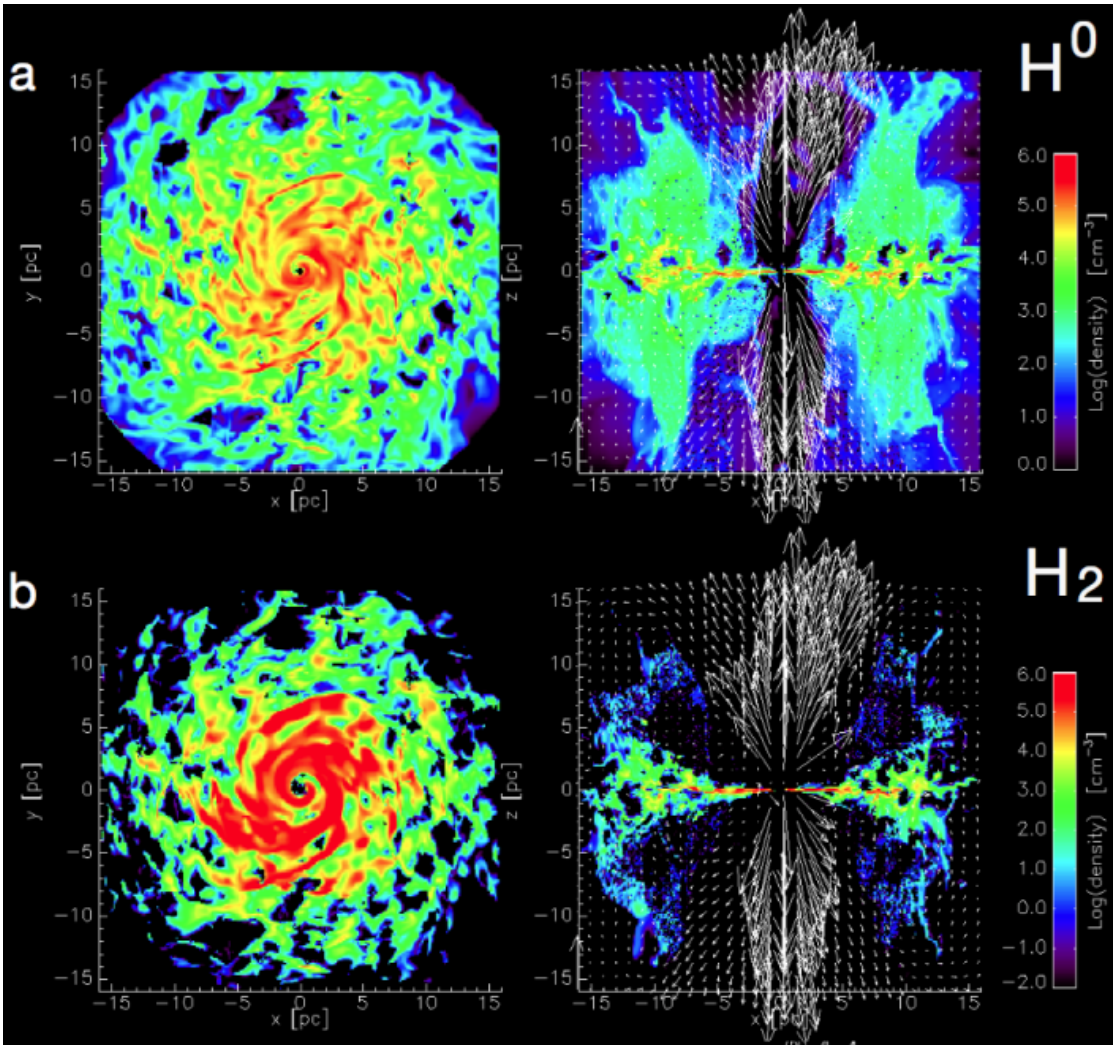

FIGURE 1.13: Density distributions of atomic (upper) and molecular (lower) gas in the radiation-driven fountain model. Left and right panels correspond to face-on and edge-on views, respectively. Figure taken from Wada et al. (2016).

Wada et al. (2016) presented a radiation-driven fountain model at large-scales (32 pc) (see figure 1.13). The simulations starts with a small ($2 \times 10^6 M_\odot$) black hole surrounded by an initially thin gas disk. The emerging structure is a combination of outflows and inflows or failed wind. The wind is driven by anisotropic UV radiation and X-ray heating, while IR radiation pressure is not included in the model. Figure 1.13 shows the distribution of atomic and molecular gas. The distribution of atomic (H^0) gas shows a hollow cone structure surrounded by a geometrically thick disk. Dense molecular gases are distributed near the equatorial plane, and energy feedback from supernovae enhances their scale height. The model is large-scale and has the advantage to be directly comparable with actual observations. However, it is limited in its ability to resolve the wind generation region, because based on a coarse resolution of 0.125 pc[6].

Other RHD simulations have mostly been performed in the sub-parsec regime. This domain size contains the sublimation radius, where the effect of radiation pressure is most extreme and wind generation can be resolved (Williamson et al., 2019).

Namekata and Umemura (2016) performed a 2-dimensional RHD simulation, taking into account the effects of metal cooling, self-gravity, anisotropic accretion disc, X-ray heating and radiative transfer of IR. They found that metal cooling suppresses the vertical support from IR and, contrary to Krolik (2007), the disc is almost supported by thermal pressure. However, a wind is produced whose properties depend on the dust distribution. These simulations were performed at Eddington ratio $\lambda_{\rm Edd} \sim 0.77$, higher than the values where AGNs with polar outflows have been observed by interferometry. Dorodnitsyn et al. (2016) presented a 2-dimensional radiation-driven wind model including UV radiation, X-ray heating, dust sublimation and IR radiation, treated in the flux-limited diffusion. Alongside the wind, a puffed-up torus is produced in these simulations, which is not clear if it is a numeric artifact or not, as the flux-limited diffusion algorithm is known to smooth out the structures surrounding the central radiation source. Chan and Krolik (2016) performed 3-dimensional RHD simulations of an initially smooth dusty torus in which IR and UV radiative fluxes are not approximated using overly simplistic

[6]Using the simplified relation $R_{sub} = 0.5 L_{45}^{1/2}$ (see e.g. Hönig and Beckert, 2007), an accreting black hole with $10^6 M_\odot$ and $\lambda_{\rm Edd} = 0.01$ is expected to have a sublimation radius of R_{sub} ~0.015 pc, which gives the order of magnitude of the wind generation region.

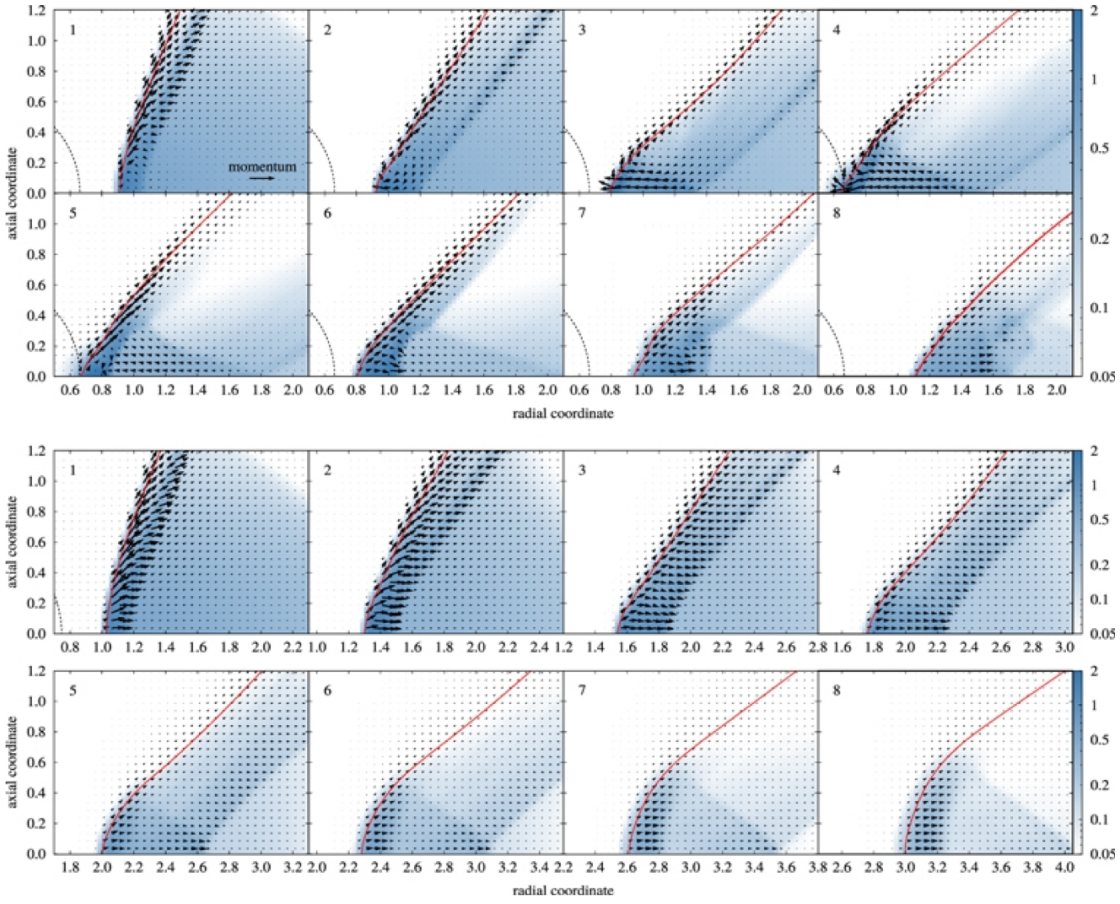

FIGURE 1.14: Gas density evolution of the torus as presented in the Chan and Krolik (2016) model. Gas density is presented on a logarithmic scale as blue intensities (see color bar along the right edge). The dust sublimation surface is the dashed black curve around the origin, and the red contour traces the surface on which $\tau_{\rm UV}$=1. Momentum density is shown by the arrows. Top grid: Plot of the $L_{\rm UV}/L_{\rm Edd} = 0.11$ simulation. Bottom grid: Plot of the $L_{\rm UV}/L_{\rm Edd} = 0.14$ simulation. Figure taken from Chan and Krolik (2016).

prescriptions. In fact, the model is based on the variable Eddington Tensor approximation, which is one of the most advanced methods available to solve the radiative transfer equations, allowing to model the re-radiated IR radiation pressure with great accuracy. As shown in figure 1.14 which is taken from their paper, the UV radiation pressure on dust launches a strong wind, peeling off the inner radius of the torus. The radial motion subsequent to the initial phase depends on L_{UV}, which determines the IR radiative flux across the torus. In the bottom grid of figure 1.13 the IR radiative flux is strong enough that gas velocity is radially outward in the torus body almost all the time, and the torus is driven outward. In contrast, in the top grid of figure 1.13, a region develops in which the sum of the radial components of IR and centrifugal accelerations falls slightly short

of counteracting gravity, and thus the radial component of velocity is negative, creating an inflow-outflow structure. Altough the behaviour of the IR radiation is treated in great detail and fundamental insights are offered, the Chan and Krolik (2016) simulations also present some limitations. In fact, the cost of such an advanced algorithm to describe UV and IR radiation is the necessity of a coarser temporal resolution to complete the simulations in a reasonable time. Some of the approximations include the use of the reduced speed of light approximation and scale down the AGN parameters to unrealistic values.

To summarize, these simulations all use different approaches, focus on different scales and often lead to drastically different conclusions about the outflow properties. This leaves the nature of the obscuring structure essentially unconstrained, as it depends not only on the physical properties of the illuminated material (e.g., dust population, stellar feedback, etc.) and the radiation pattern of the AGN accretion disk, but also on the numerical treatment of radiative transfer and resolution issues.

1.8 Aim of this work

High-angular resolution IR, sub-mm interferometry and X-ray observations add several important pieces of information to test the unification model of AGNs. IR interferometry allows resolving the torus structure, sub-mm observations probe the molecular phase while X-ray provides information about the Eddington ratio dependence. The picture drawn by Hönig (2019) offers a unifying view of the torus dynamics and structure, derived from the similarities shared by the various AGN observations in the infrared and sub-mm regimes but further theoretical work is required to support these findings. Radiation hydrodynamics torus models agree on the emergence of outflows driven by radiation pressure but the numerical strategies adopted vary significantly between models, making it difficult to find a converging picture. The goal of this Thesis is to critically assess the origin of dusty winds detected on the parsec-scales environment around AGN, with particular reference to the role of radiation pressure, and make progress towards understanding the broad picture of AGN activity.

In Chapter 2 a new dynamical model is presented, using a three-dimensional radiation hydrodynamics algorithm. These simulations have the specific aim to explore the role of radiatively-driven outflows. The model consists of a disk of gas and particles fully exposed to the AGN radiation field. The dynamical evolution of such a system is presented first in the small scales regime, where the wind is produced, then in a larger scales model which allows a direct comparison to observations. A strong point of the radiation hydrodynamics model is that it includes all the complex physics and chemistry operating at smaller scales in a form of look-up tables, developed with the use of the photoionization code Cloudy (Ferland et al., 2013, 2017). This chapter describes the main features of the simulations and how the Cloudy models have been designed and properly tabulated.

In Chapter 3 a semi-analytical model is presented to investigate the role of the IR radiation pressure in shaping the dusty environment of AGNs. The model consists of an AGN and an infrared radiating dusty disk. It examines the trajectories of dusty gas clumps in this environment, accounting for both gravity and the AGN radiation as well as the re-radiation by the hot dusty gas clouds themselves. This investigation allows to make predictions on the final morphology expected and offer insights on the obscuration properties of AGNs.

In Chapter 4 Using the results from the previous chapters, the case of a possible connection between dusty winds and obscuring outflows observed in the UV is examined, to test whether or not these kinds of outflows could actually represent different parts of a single, multiphase outflow.

In Chapter 5 results and conclusions from this PhD thesis are summarized and an outlook for future work is given.

Publications related to the individual chapters are noted and the most significant contributions in the framework of this PhD Thesis have been indicated at the beginning of the chapter.

Chapter 2

Photoionisation in the Radiative Hydrodynamics model

> "He who receives an idea from me, receives instruction himself without lessening mine; as he who lights his taper at mine, receives light without darkening me."
>
> Thomas Jefferson

This chapter is based on a work published in the papers Williamson et al. (2019) and Williamson et al. (2020). I contributed to the photoionisation modeling which forms the foundation of the radiation hydrodynamics simulations presented in the published papers. The work presented in this chapter describes my own original contribution.

2.1 Overview and context

Observations of the dusty torus reveal a structure which is complex and dynamical. Radiation hydrodynamic simulations aiming to interpret these observations are forced to reduce the physical components involved as a compromise with computational expenses. Some of the computational challenges include the modeling of the IR radiation pressure,

the anisotropy of the AGN radiation field, the numerical treatment of radiative transfer and the spatial scales considered. In particular, most of the simulations focus on the wind-generation region, which is difficult to link to actual observations. Hence, there is motivation to probe the dynamics of the torus at various spatial scales adopting a method which is coherent across different domain sizes.

In the followings, our 3-dimensional RHD model is presented (published in Williamson et al. (2019) and Williamson et al. (2020)). The problem here is approached both in the small-scales (paper 1) and in the large-scales regime (paper 2), offering a comprehensive view of the matter at hand. Among the distinguishing features of the model is the fact that is based on a lagrangian formulation of hydrodynamics, which has the ability to provide very high resolution in dense regions while simultaneously capturing large length scales accurately. Another unique element is the incorporation of heating, cooling, and radiation pressure on gas and a physically consistent composition of dust, including differential sublimation, through the use of CLOUDY (Ferland et al., 2013, 2017), which is one of the most accurate radiative transfer and photoionisation codes available. This is the aspect on which I worked most closely in this research work and represents my main contribution to the RHD simulations.

Dissipation of energy through radiative cooling is a crucial ingredient to model the evolution of astrophysical systems and the appearance of outflows. These processes depend on the properties of the gas and the radiation field in a potentially complex way and their detailed treatment is impractical and too time-consuming to be performed "on the fly" during the simulations, so they are either ignored or other strategies or approximations are adopted. For example, Namekata and Umemura (2016) takes into account standard cooling processes pertaining to hydrogen, helium and dust, while the effect of metals is considered in an approximate way through a cooling function. A more realistic treatment of heating and cooling rates has been done by Wada et al. (2016). The rates are calculated using a radiative transfer model of photo-dissociation regions and self-consistently changed in the simulations based on the values of temperatures, H_2 abundances, intensity of the radiation source and density.

In Williamson et al. (2019, 2020), we adopted a different strategy. Heating and cooling are incorporated in form of look-up table, based on a large grid of CLOUDY models

which I developed. The table also includes a number of important physical quantities, such as the temperature of the dust, the dust to gas mass ratio, radiative acceleration, opacities and emissivities of several lines (see section 2.4). These quantities have been then interpolated to determine the appropriate value. This allows the simulations to be computationally fast while providing an unprecedented level of detail in the context of RHD modeling of dusty regions in AGN. The following sections describe the main features and results of the simulations and how the CLOUDY models have been designed and properly tabulated.

2.2 The RHD model

The dynamical simulations are based on the emerging picture that many of the observed obscuration properties of AGN are a result of a disk, a wind and a puffed region (see section 1.6.4), where the dynamics is dominated by radiation pressure effects. To approach this problem we performed two separate sets of simulations. The first work published in Williamson et al. (2019) is a small-scales model that is focused on the wind generation region close to the sublimation radius. The second work published in Williamson et al. (2020) extends these high resolutions to a larger scales model, so that results can be directly compared to observations. These simulations consider the radiation pressure coming from the central AGN, neglecting the re-radiation of dust in the infrared. The effect of the infrared is treated separately through an analytical model in Chapter 3. These two sets of simulations implement the same numerical methods, with some additions and modifications in the large-scales runs. The dynamical evolution is solved using smoothed particle hydrodynamics, which is a novel element with respect to previous RHD models and has several advantages in terms of resolution, as we shall see below.

2.2.1 RHD simulations methods

Both the small and large-scales simulations are based on the public version of the N-body+hydrodynamics code GIZMO (Hopkins, 2015) in pressure smoothed-particle

hydrodynamics (SPH) mode. SPH is a reliable particle-based approach to solve the hydrodynamic equations and especially suited to resolve high-density region using a Lagrangian mesh-free formulation. The SPH method works by dividing the fluid into a set of discrete moving elements, referred to as particles. These particles have a spatial distance (the "smoothing length", typically denoted by h), over which their properties are "smoothed" through convolution with a kernel function (typically represented by W). Commonly used kernel functions are the gaussian function and the cubic spline (as used in our model). For a visual representation of a kernel function, see figure 2.1. The

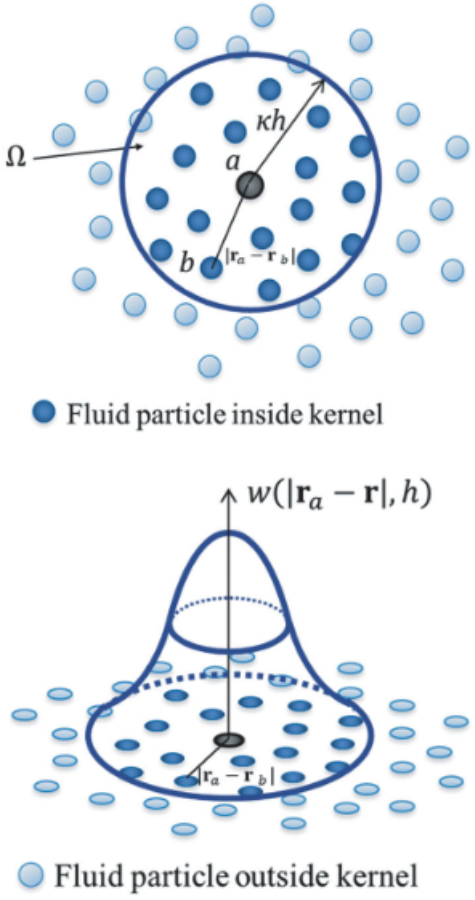

FIGURE 2.1: Visual representation of a SPH kernel function. Figure taken from Eriksson (2018).

resulting convolutions are evaluated numerically by approximating the integrals with

discrete sums according to the following expression

$$A(r) = \sum_j \frac{m_j}{\rho_j} A_j W(|r - r_j|, h), \tag{2.1}$$

where the summation over j includes all particles in the simulation, V_j is the volume of the particle j, A_j is the value of the quantity A for particle j and r denotes position. The advantage of SPH is that the smoothing distance can be adapted in the simulation. For example, in regions where many particles are close together the smoothing distance can be relatively short, producing high spatial resolution. Conversely, in regions with a low number of particles the smoothing distance can be increased, saving computational resources. SPH is a pure Lagrangian method, in contrast to Eulerian methods which

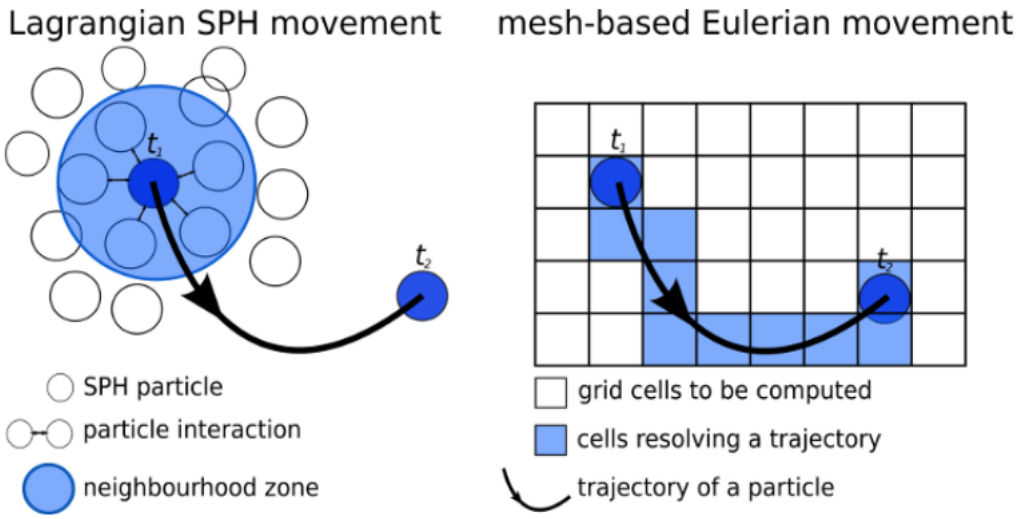

FIGURE 2.2: Difference between Eulerian and Lagrangian methods. Figure taken from Gupte (2018).

are grid based methods. The main difference between the two methods is related to time derivatives. In the Eulerian picture time derivatives are calculated at a fixed point in the space, on the other hand in the Lagrangian description they are calculated in a coordinate system attached to a moving fluid element. The Lagrangian derivative D/Dt is related to the Eulerian derivative $\partial/\partial t$ by

$$\frac{D}{Dt} = \frac{dx^i}{dt}\frac{\partial}{\partial x^i} + \frac{\partial}{\partial t} = \mathbf{v} \cdot \nabla + \frac{\partial}{\partial t}, \tag{2.2}$$

where the term $\mathbf{v} \cdot \nabla$ is the term capturing the change in particles properties as they move.

The previous simulations of the AGN torus region mentioned in Section 2.1 were performed with an Eulerian formulation on a fixed grid in two or three dimensions. By choosing a Lagrangian description, we are providing an almost orthogonal perspective to existing studies. In fact, despite being fundamentally different, SPH and grid methods have complementary strengths and weaknesses. On one hand, Eulerian methods are limited by length resolution, and therefore resolve high density region poorly. On the other hand, Lagrangian methods are limited by mass resolution, therefore resolve low density fluid poorly[1]. In this particular context, the RHD model will not effectively resolve low-density winds in the ionisation cone of the AGN. However, it will efficiently resolve the denser gas that contributes the most to the opacity and infrared luminosity of the torus region.

The basic equations of motion to be solved are the compressible Euler equations. SPH guarantees conservation of mass without extra computation since the particles themselves represent mass. The only equations that need to be solved are the momentum and energy conservation equations:

$$\frac{D\mathbf{v}}{Dt} = -\frac{\nabla P}{\rho} + \mathbf{g} + \mathbf{a_r}, \tag{2.3}$$

$$\frac{Du}{Dt} = -\frac{P}{\rho}\nabla \cdot \mathbf{v} + H \tag{2.4}$$

where P, ρ, u, and $\mathbf{v}$ are the pressure, density, internal energy, and velocity of the fluid, $\mathbf{g}$ is the acceleration from gravity, $\mathbf{a_r}$ is the radiative acceleration, and H is the combination of all heating and cooling effects.

Dust is treated in the simulations as an additional gas property, meaning that the gas and dust components are evolved together. Simulations also include self-gravity, star formation and supernovae. Self-gravity hydrodynamics are solved in GIZMO with a Barnes-Hut oct-tree (Barnes and Hut, 1986), an algorithm able to reduce the total

[1] Although in SPH there is no spatial resolution limit for the smoothing length, there is a fixed mass resolution limit. The variable smoothing lengths of particles are constrained to contain a roughly constant number of particles and, hence, a certain mass (Bate and Burkert, 1997).

number of pair interactions and hence execution time[2]. A raytracing technique has been implemented for radiative transfer from the central AGN engine, which is assumed to consist of anisotropic emission from a luminous accretion disc plus a small isotropic contribution from a corona. As mentioned in section 2.1, the effects of radiation (heating, cooling, and radiation pressure) are pretabulated using CLOUDY (Ferland et al., 2013, 2017) and the work behind it represents my main contribution to the RHD model. The followings sections will describe the characteristics of the CLOUDY code as well as its implementation into the RHD simulations.

2.3 Cloudy

The physical conditions within an astronomical plasma are set by a large number of microphysical processes. Together, all these processes set the ionisation and thermal structure of the gas. The observed spectrum is the result of radiation propagating through the depth-dependent physical conditions of the gas. No analytical solution is possible, and one needs a sophisticated numerical code to study it. CLOUDY (Ferland et al., 2013, 2017) is an open-source photoionisation code which has been designed for this purpose. It models the physical conditions of gas and predicts the observed spectrum. CLOUDY is continually being developed to improve the treatment of the microphysical processes and the database of fundamental data that it uses. An optically thick slab of gas is divided into a large number of zones, chosen so that conditions are fairly constant across each. CLOUDY determines the ionisation and excitation state of all constituents self-consistently by balancing all ionisation and excitation processes. Ionisation processes include photo, Auger and collisional ionisation and charge transfer. Recombination processes include radiative, low-temperature dielectronic, high-temperature dielectronic, three-body recombination, and charge transfer. The free electrons are assumed to have Maxwellian velocity distribution with a kinetic temperature set by the balance of heating and cooling processes. This approach has energy conservation as its foundation.

[2]The key idea of the Barnes-Hut algorithm is to approximate long-range forces by replacing a group of distant points with their center of mass. Source: https://jheer.github.io/barnes-hut/.

2.3.1 What must be specified

CLOUDY needs a minimum few parameters before it can predict the conditions within a cloud. These are:

- The shape and brightness of the radiation field striking the cloud.
- The total hydrogen density.
- The composition of the gas and whether grains are present.
- The thickness of the cloud.

The hydrogen density is given by the total density of H in all forms (including molecular)

$$n(H) = n(H^0) + n(H^+) + 2n(H_2) + \sum_{other} n(H_{other}) \text{ cm}^{-3}. \quad (2.5)$$

Unless otherwise specified the gas-phase abundances will be close to solar values and grains will not be included. The cloud will have a plane-parallel geometry. The total hydrogen density will be kept constant across the cloud since this is the default. One can test different models, including constant pressure, constant temperature (as in our tables), hydrostatic equilibrium, wind models and several other geometries.

2.4 The Cloudy models in the RHD simulations

The RHD code considers a large suite of CLOUDY models and it is developed in a way that the relevant physical properties can be easily accessed during the simulations. This procedure has the double advantage to optimise the computational load of the RHD simulations and speed them up while offering a microphysical rich and complete picture of the dust and gas mixture, which could otherwise not be accounted for, including ionisation, charge transfer and molecular and dust chemistry.

My CLOUDY models take three parameters as input: the volumetric density of the cloud, the incident AGN radiation field and the temperature of the gas. Accordingly, the gas

and dust temperatures are not necessarily in thermal equilibrium with the AGN. For a given set of the three input parameters, we compute and tabulate several physical quantities. Those are:

1. the heating and cooling rate
2. the temperature of the dust
3. the dust to gas mass ratio
4. the radiative acceleration due to the continuum
5. the flux-weighted opacities and optical depth
6. emissivities of two CO lines (CO(3-2) 866.727 μm, CO(6-5) 433.438 μm), two HCN lines (HCN(4-3) 845.428 μm, HCN(8-7) 422.796 μm) and three vibrational transitions of H_2 (H_2 (1-0) S(1) 2.121 μm, H_2 (0-0) S(3) 9.66 μm, H_2 (0-0) S(0) 28.18 μm)

In this section, I describe the physical parameters used in the photoionisation modeling of the emitting and absorbing gas studied in this Thesis.

2.4.1 The shape and brightness of the incident radiation field

The external radiation field is usually specified in CLOUDY with two different commands. One specifies the shape of the incident radiation field. A second command will set the brightness of the light. There are two ways to specify the brightness of the external radiation field, either using the intensity or luminosity. In this Thesis I used the intensity case as described below.

2.4.1.1 Intensity

In the intensity case the energy flux (erg $cm^{-2}s^{-1}$) striking a unit area of the cloud is set. The intensity is defined by the expression

$$I = \frac{F}{\pi} \quad , \tag{2.6}$$

where F is the flux which is related to the total luminosity L by

$$F = \frac{L}{4\pi R^2} \quad , \tag{2.7}$$

with R being the inner radius of the cloud. The inner radius does not need to be specified in CLOUDY, although it is possible to do so. The predicted emission-line spectrum is then given in intensity units. In my models I do not fix the inner radius, because the intensity itself gives information about the distance of the cloud if a dusty model is assumed. In fact, the presence of dust grains, mixed with the gas, is determined by the flux of incident radiation: below a given value, dust grains can survive. This location actually depends on dust composition and grain size, which is fixed in my case. In my model I tabulate a total of 19 intensity values, starting from the intensity at the sublimation radius. This has been determined by running several CLOUDY models with fixed luminosity (I used $L_{AGN} = 2.2 \times 10^{43}$ erg s^{-1}) and including differential dust sublimation in the calculation. Then I looked for the distance of the cloud for which the illuminated face is at $T_{sub} \sim 1750$ K, the maximum temperature at which large graphite grains can survive before being sublimated. I double-checked that all grain types were missing in the first cell of the computation. The value obtained for the incident sublimation intensity is $I_0 = 5.6 \times 10^7$ erg cm^{-2} s^{-1},

2.4.1.2 SED

One of the most important parameters in any photoionisation computations of an irradiated medium is the broad band spectral energy distribution (SED) of the source. It has been shown that the shape of the SED affects the ionisation and thermal structure of the photoionised gas, and hence the properties of AGN winds (e.g. Dyda et al., 2017), but I focus on a single SED in this work. CLOUDY has a built-in AGN continuum command, which is meant to reproduce the SED similar to typical radio quiet active galaxies. However, the shape given is very simplistic and the authors of CLOUDY themselves suggest adopting a different shape. Then, we generate a custom AGN SED having a Big Blue Bump modeled by a black body and two broken power laws. The black body has a temperature of $T = 10^{5.5}$ K and an X-ray to UV flux ratio -1.40. The slope of the Big Bump

and the slope of the X-Ray component are left at the CLOUDY default values of −0.5 and −1.0. This produces less strong inverse Compton scattering of the X-ray photons to radio wavelengths with respect to the CLOUDY built-in AGN continuum command. I also include the cosmic ray background and a stellar background, the latter with an integrated intensity of 1000 Habing units[3], which accounts for the nuclear clusters found in the centers of galaxies.

2.4.2 Gas density, column density and temperature

The gas density, denoted by $n_{\rm H}$, is another important parameter in the simulations of the photoionised gas. In this Thesis I assume constant density values, which means it remains the same across the depth of the cloud. The total thickness of the cloud is set by assigning the column density $N_{\rm H}$ in such a way that $\mathrm{d}N_{\rm H} = n_{\rm H}\ \mathrm{dz}$, where dz is the geometrical thickness of an individual layer. In my models I fix the maximum column density to $N_{\rm H}$=10^{26} cm^{-2}. I note that some models do not converge up to such a high value, therefore I need to interpolate those results. Since the temperature is an input parameter for my tables, the models are all constant gas temperature, allowing the dust temperature to reach equilibrium with the radiation field. In some models the temperature can go down to very low temperatures (10 K), and hence cannot converge because beyond the CLOUDY default stopping criterion (4000 K). Then, all my models include the CLOUDY command "stop temperature off" to switch off this limit and force a converging solution even in the extremely low temperatures regime.

2.4.3 Gas-phase abundances

In any photoionisation computations, chemical abundances are very essential for the correct modeling of the interactions of photons with individual ions. Unless otherwise specified, CLOUDY assumes solar abundances. In this Thesis, I use the ISM gas abundances sets stored in the code, as shown in figure 2.3. Abundances are always specified relative to hydrogen.

[3] 1 Habing unit corresponds to the integrated flux in the wavelength range from 91.2 to 111.0 nm of 1.6×10^{-3} erg cm^{-2} s^{-1}.

FIGURE 2.3: The chemical abundances of the first 30 gas elements used in the photoionisation computations.

Atomic number	Element	ISM abundances
1	Hydrogen H	1.00E+00
2	Helium He	9.80E–2
3	Lithium Li	5.40E–11
4	Beryllium Be	2.63E–11
5	Boron B	8.90E–11
6	Carbon C	2.51E–04
7	Nitrogen N	7.94E–05
8	Oxygen O	3.19E–04
9	Fluorine F	2.00E–08
10	Neon Ne	1.23E–04
11	Sodium Na	3.16E–07
12	Magnesium Mg	1.26E–05
13	Almunium Al	7.94E–08
14	Silicon Si	3.16E–06
15	Phosphorus P	1.60E–07
16	Sulphur S	3.24E–05
17	Chlorine Cl	1.00E–07
18	Argon Ar	2.82E–06
19	Potassium K	1.10E–08
20	Calcium Ca	4.10E–10
21	Scandium Sc	1.00E–20
22	Titanium Ti	5.80E–10
23	Vanadium V	1.00E–10
24	Chromium Cr	1.00E–08
25	Manganese Mn	2.30E–08
26	Iron Fe	6.31E–07
27	Cobalt Co	5.90E–09
28	Nickel Ni	1.82E–08
29	Copper Cu	1.50E–09
30	Zinc Zn	2.00E–08

2.4.4 Dust properties

I adopt the built-in interstellar medium dust grain model in CLOUDY including differential sublimation, added using the command "function sublimation". The grain model includes graphites and silicates covering a broad range of sizes, whose distribution is described by the so-called *MRN* distribution derived by Mathis, Rumpl and Nordsieck on the basis of the observed interstellar extinction from ultraviolet to infrared wavelengths (Mathis et al., 1977). The resulting distribution has a power-law trend following $n(a) \propto a^{-3.5}$, where $n(a)$ is the number density of grains with radius a between $0.005 < a < 0.25$ μm. This broad size range is represented in CLOUDY by 10 log-equally spaced bins da of length 0.167 dex, meaning that it separately models 10 different optical properties for each graphite and silicates components, for a total of 20 grain species. Since the temperatures of the dust and mass ratio strongly depend on the size, these two properties are calculated and saved by CLOUDY or each species and not as a mean quantity. My goal is to have a single value of the dust properties as a function of column density, so it can be tabulated. I have adopted two different procedures for the dust temperature and the dust to gas mass ratio. For the dust to gas mass ratio, I have simply computed the arithmetic mean. For the dust temperature, instead, I have taken an area-weighted average over the entire dust population. Then I describe the temperature for all the dust population by considering a single grain of average size

$$\pi < a^2 >= \frac{\int \pi a^2 a^{-3.5} da}{\int a^{-3.5} da} \quad \Rightarrow \quad < a >= \sqrt{\frac{\int a^2 a^{-3.5} da}{\int a^{-3.5} da}} \tag{2.8}$$

This calculation gives $< a >= 0.010$ μm which falls in the second bin of the CLOUDY grain species size array.

2.4.5 Cloudy tables

For our RHD simulations, I have produced three tables: a 'dusty' table, a 'sputtered' table, and a 'high density' table. The 'dusty' and 'high density' tables include grain molecules, while the 'sputtered' table does not. The sputtered table is used for particles with temperatures $10^5 - 10^8$ K, the 'high density' table is used for particles with

temperatures $10^1 - 10^3$ K and densities $10^8 - 10^9\,\mathrm{cm}^{-3}$, and the 'dusty' table is used otherwise. I interpolate between the tables where appropriate. The high-density table only contains cool-warm gas. Hot dense gas does not exist in the RHD simulations, and it was difficult for the CLOUDY runs to converge at these high densities.

The main 'dusty' table includes 8 densities from $10^0 - 10^7\,\mathrm{cm}^{-3}$, equally spaced in log space. The temperature from $10^1 - 10^5$ is tabulated in 20 log-spaced steps, with a step size of 0.25 dex for $\log \mathrm{T} < 5$, and a larger step of 1 dex at higher T. Radiation intensity is tabulated from $10^{1.25} - 10^{9.25}$ erg cm$^{-2}\,s^{-1}$ in 17 equally log-spaced steps. Each CLOUDY run outputs a large number of cells at different column density which we interpolate to 256 log-spaced steps up to $N_H = 10^{26}$ cm^{-2}.

In total I carried out and interpolated for tabulation $\sim$ 4000 CLOUDY simulations, covering each combination of intensities, temperatures and densities.

2.5 Cooling and Heating

In this section I will briefly outline the main heating and cooling processes included in CLOUDY, with particular reference to the ones relevant to RHD simulations of the dusty environment of AGN.

The balance between heating and cooling processes determines the temperature of the interstellar gas. The temperature used to describe the gas is normally the kinetic temperature of free electrons, which very quickly thermalize through collisions and setup a Maxwellian velocity distribution. Heating is any process that gives energy to the gas, increasing the temperature. Cooling is any process that removes energy from the gas, lowering the temperature. This usually happens by radiative cooling. That is, photons having an excess in energy will escape from the medium, therefore cooling it. Depending on the temperature, density, and ionisation state of a portion of the ISM, different heating and cooling mechanisms determine the temperature of the gas.

2.5.1 Heating mechanisms

In practice, the major heating mechanism in the ISM is any process that involves transferring kinetic energy to free electrons. These electrons quickly thermalize with other gas particles through collisions, redistributing energy in excess and thus inducing heating. Fast free electrons can be ejected from particles by a large variety of mechanisms. We will outline the most relevant ones in the context of my cloudy models.

- **Photoionisation**: in this process, the absorption of a photon (typically UV) gives rise to an electron with energy $E' = E_{photon} - E_{ionisation}$. Photons having energy 11.26< $h\nu$ <13.6 eV are likely to ionise a carbon atom. More energetic photons with $h\nu > 13.6$ eV will end up ionising the more abundant hydrogen atoms. This method of heating dominates ionised regions having T $\sim 10^4$ K.

- **Photoelectric heating by grains**: this mechanism dominates the dusty ISM. Similar to ionisation, the UV radiation can remove electrons from dust grains. This method of heating is dominated by the smallest dust grains, since the distribution of the grain areas $a^2 n(a) \propto a^{-1.5}$, and is typical in the cold neutral medium (cold dense gas with T $\sim$ 100 K) and the warm neutral medium (diffuse gas with T $\sim 10^4$ K). The photon is absorbed by the dust grain, and some of its energy is used to overcome the potential energy barrier (the work function) and remove the electron from the grain. The work function for a small dust grain is $w \sim 5$ eV. Thus, photons having energy > 5 eV can eject photoelectrons from small dust grains. The remainder of the photon's energy gives the ejected electron kinetic energy, which heats the gas through collisions with other particles.

2.5.2 Cooling mechanisms

- **Cooling by interstellar dust grains:** As well as a heat source, dust is also an important coolant in the interstellar medium. Dust absorbs optical and UV photons and re-emits in the infrared, contributing thereby to cooling.

- **Cooling by electron-ion collisional excitation:** Collisionally excited emission lines is the dominant cooling mechanism in most regions of the Interstellar Medium,

except regions of hot gas and regions deep in molecular clouds. It involves collisions between one free electron and an ion to form a highly excited state. The excited state can decay via recombination, emitting radiation which may escape the region and thus cooling it. Some of the most important ions are O II, O III, N II and N III.

- **Cooling by electron-hydrogen excitation:** For high temperatures T $\gtrsim 10^3$ K loss by energy by excitation of neutral hydrogen is an important cooling mechanism, especially the $n = 2$ level due to collisions of thermal electrons. The excited atom decays, emitting a Lyman α photon.

- **Thermal Bremsstrahlung:** this can be a significant coolant mechanism in an ionised gas at T $> 10^6$ K. Free electrons are accelerated by charged particles, emitting "braking radiation".

- **Cooling by molecules:** Collisional excitation and de-excitation of vibrational and rotational states of molecules is an important cooling mechanism. The most important molecules are H_2, H_2O and CO. Molecular hydrogen is the most abundant molecule and a dominant coolant for temperatures 10^4 to 10 K. Additionally, H_2 plays an important active role in fuelling a chemistry that provides molecular coolants that are capable of cooling to the lowest temperatures, like H_2O and OH. It worth mentioning that H_2 is a symmetric molecule and thus the vibrational or rotational transitions are very weak and hard to observe. CO is the next most abundant molecule after H_2, and an important coolant at temperatures T $\lesssim 100$ K.

2.6 Radiative acceleration and opacities calculations

The radiative acceleration and opacities are an essential ingredient to determine the amount of energy deposited into the illuminated gas, and thus characterise its dynamical evolution. One issue I encountered using CLOUDY is that code does not isolate the AGN radiation from the re-radiation of the hot gas, while the RHD model requires the contribution to the acceleration and opacities of the central radiation source only. In

addition, opacities are saved as a function of frequency for the last computed zone, while the RHD model needs a frequency integrated value as a function of column density or depth into the cloud. Nevertheless, I worked out an effective solution to tackle these problems. There is a command in CLOUDY that saves the continuum volume emissivity, as well as the local absorption and scattering opacity (in cm^{-1}), as a function of depth into the cloud (in cm). The opacities printed out are the total gas and dust opacities, which incorporate anisotropic scattering factors for dust. However, this works for a specific frequency only, out of the total 5277 frequencies values in CLOUDY (version c17). Therefore, the only way to generate tabulated opacity data for each zone is to call this command 5277 times, i.e. for every single frequency. To do so, it was necessary to modify the source code in order to extend the code capabilities and save more than the default limit of 100 outputs at once. Once all the CLOUDY and system extensions have been properly set, it is possible to extract all the properties of the incoming AGN flux explicitly.

First, I generate an optical depth table as follows

$$\tau(\nu, r = \bar{r}) = \int_0^{\bar{r}} k_{abs}(\nu, r) + k_{scat}(\nu, r)\, dr \tag{2.9}$$

where $\bar{r}$ is the specific zone at which the optical depth τ is evaluated and k_{abs} and k_{scat} are respectively the absorption and scattering opacities as printed from CLOUDY. The result is a two-dimensional matrix of the form

$$\tau_{r,\nu} = \begin{pmatrix} \tau_{r_0\nu_0} & \cdots & \tau_{r_0\nu_n} \\ \vdots & \ddots & \vdots \\ \tau_{r_m\nu_0} & \cdots & \tau_{r_m\nu_n} \end{pmatrix}$$

where the subscript m represents the number of zones, which is actually dependent on the CLOUDY model, and ν_n are the number of frequencies. Table 2.1 shows the resulting $m \times n$ optical depth matrix. The result is an array showing the opacities for each zone into the cloud and for each frequency. For simplicity, I define $k_{tot} = k_{abs} + k_{scat}$. Notice that the first zone has always $\tau_{r_0,\nu} = 0$ since the integral $\int_{r_0}^{r_0} dr = 0$. This is also consistent with the fact that the first zone corresponds to the illuminated face of the

cloud, so the continuum must correspond to the incident continuum.

$\tau_{r,\nu}$				
	ν_0	ν_1	$\dots$	ν_N
r_0	0	0	$\dots$	0
r_1	$\int_{r_0}^{r_1} k_{tot}(\nu_0, r)dr$	$\int_{r_0}^{r_1} k_{tot}(\nu_1, r)dr$	$\dots$	$\int_{r_0}^{r_1} k_{tot}(\nu_N, r)dr$
$\vdots$	$\vdots$	$\ddots$	$\ddots$	$\vdots$
r_m	$\int_{r_0}^{r_m} k_{tot}(\nu_0, r)dr$	$\int_{r_0}^{r_m} k_{tot}(\nu_1, r)dr$	$\dots$	$\int_{r_0}^{r_m} k_{tot}(\nu_n, r)dr$

TABLE 2.1: Array created to compute the optical depth as a function of frequency and distance from the AGN.

Using the matrix 2.6, we calculate the attenuation of the incident continuum $I_\nu(r_0)$ as

$$I_{r,\nu} = I_\nu(r_0)\, e^{-\tau_{r,\nu}} \,. \tag{2.10}$$

The expression above corresponds to multiply two-dimensional matrices for each frequency and radius as follows

$$I_{r,\nu} = \begin{pmatrix} I_{r_0,\nu_0} \\ I_{r_0,\nu_1} \\ \vdots \\ I_{r_0,\nu_n} \end{pmatrix} \begin{pmatrix} e^{-\tau_{r_0\nu_0}} & \dots & e^{-\tau_{r_0\nu_n}} \\ \vdots & \ddots & \vdots \\ e^{-\tau_{r_m\nu_0}} & \dots & e^{-\tau_{r_m\nu_n}} \end{pmatrix}^T \tag{2.11}$$

This allows to extract the emergent continuum for each zone and each frequency. I note that what CLOUDY indicates as intensity is actually $I_{\nu,\text{CLOUDY}} = \nu I_\nu$, so all the values need to be scaled by the frequencies.

The RHD model needs a flux weighted average for both absorption and scattering opacities, as well as for the optical depth. Hence, using the intensity matrix 2.10, we tabulate

both absorption and scattering opacities as

$$< k_r >= \frac{\int k_{r,\nu} I_{r,\nu} d\nu}{\int I_{r,\nu} d\nu} \tag{2.12}$$

and the flux weighted optical depth as

$$< \tau_r >=< k_{abs,r} > + < k_{scat,r} > \quad . \tag{2.13}$$

Then, I tabulate the radiative acceleration as follows

$$a(r)_{rad} = \frac{1}{c} \int \left(k_{tot}(\nu, r) + k_{scat}(\nu, r) \right) \pi I(r, \nu) d\nu \quad . \tag{2.14}$$

The radiative acceleration, the intensity mean opacities, the total optical depth and the intensity of the AGN radiation for each zone of the cloud have been interpolated and added to the gas and dust properties tables that form the basis of the RHD simulations.

2.7 Interpolation method

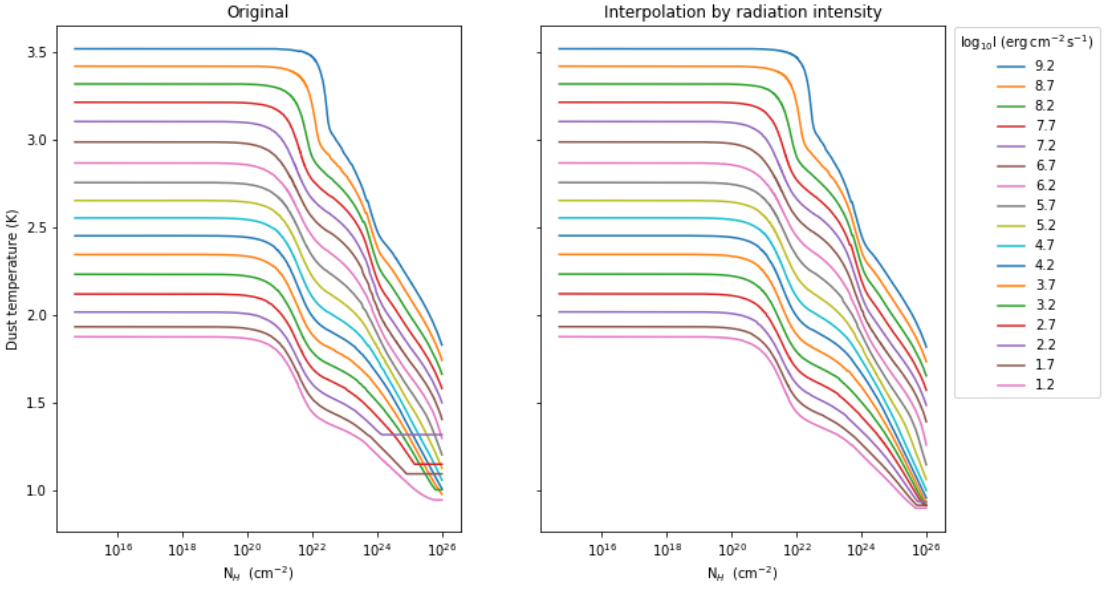

FIGURE 2.4: Example of interpolation using the radiation intensity trends for non-converged CLOUDY results at high density and low gas temperatures. Here it is shown the dust temperature profile at different radiation intensity for the case $n_H = 10^6$ cm^{-3} and T_{gas}=10 K.

Each CLOUDY simulation produces a different number of zones, depending on the specific model. Thus, the quantities relevant to the RHD simulations need to be interpolated to a fixed column density grid. This grid has been chosen by looking at the typical number of zones and spacing that most CLOUDY calculations produce. Specifically, I took the column density grid of a model having density 10^2 cm^{-3}, radiation intensity $10^{7.75}$ erg cm^{-2} s^{-1} and temperature 10 K. This corresponds to 594 number of zones up to column density 10^{26} cm^{-2}. The interpolation has been performed with a spline function and subsequently smoothed using a Savitzky-Golay filter. The Savitzky-Golay filter is a commonly used smoothing method performed by approximating sub-sets of adjacent data points by a low-order local polynomial, using a moving window technique.

I noticed that CLOUDY not always produces converged results at high densities, low temperatures and low radiation intensity regime. For a few of these non-converging models, I have used version c13 of CLOUDY. This version includes less chemical reactions with respect to the latest CLOUDY version c17, allowing to complete the simulations in a reasonable time. However, the most common problem characterising the high densities, low radiation intensity, and low temperatures regime in the CLOUDY simulations is the fact that the simulation stops at very low column density values. In this case, I have extrapolated the results by interpolating back from either the high temperatures or the high radiation intensity results. An example of the interpolation method adopted is shown in figure 2.4.

2.8 Key foundations of the RHD model - Summary

The previous sections have covered in detail all the assumptions forming the basis of the RHD model. Before moving to the actual simulations results, it useful provide a summary of the key foundations of the model:

- The RHD code implements SPH, a particle-based Lagrangian formulation of hydrodynamics, and uses the Barnes-Hut algorithm to group nearby particles and approximate them as a single body, hence reducing the number of pair interactions and speeding up the simulations.

- Self-gravity is included, which can produce gravitational instabilities. The simulations also implement a supernova feedback model.

- The central AGN engine is assumed to be the only (non-background) source of radiation, neglecting the contribution from the IR radiation pressure. The AGN flux is assumed to be anisotropic.

- The model implements a raytracing algorithm that calculates the optical depth between the central AGN and each gas particle. The internal properties of the gas particles and most of the details of radiative transfer are pre-calculated using a suite of CLOUDY models.

- The CLOUDY models include an AGN SED, a constant stellar background of 1000 Habing units, ISM gas-phases abundances, a dust grain model that includes graphites and silicates with sizes following the MRN distribution, and extinction from dust and gas (including molecules).

2.9 Small-scales RHD simulations

This set of hydrodynamic simulations have the specific aim to model the parsec-scales dynamics of the dusty disk, to ensure maximum resolution of the wind generation and its properties. For its computational cost, only the radiation pressure coming from the AGN is considered.

The AGN flux is assumed to be anisotropic, following

$$F(r,\theta) = \frac{L}{4\pi r^2} f(\theta) \quad , \tag{2.15}$$

where L is the luminosity of the AGN, r is the distance from the AGN, θ is the angle from the polar axis of the AGN, and the asymmetry function $f(\theta)$ is defined to be

$$f(\theta) = \frac{1 + a\cos\theta + 2a\cos^2\theta}{1 + 2a/3} \quad . \tag{2.16}$$

where $a = (\eta_a - 1)/3$, introducing the parameter η_a as the "asymmetry factor", equal to the ratio between the polar flux and the equatorial flux. This is an arbitrary generalisation of the "classic" angle-dependence of Netzer (1987a), to account for deviations from perfect limb-darkening of a geometrically thin disk. This chosen generalisation produces only a small variation in polar flux with η_a, despite a large variation in equatorial flux. The asymmetry factor η_a is not well constrained by observations, and strongly depends on the model assumed for the accretion disk and corona. It is likely to vary by wavelength, as emission from the corona should be more isotropic than emission from the accretion disk. In the RHD model, η_a is assumed for simplicity to be independent of wavelength, as this allows to assume a constant SED before extinction is included. η_a is a free parameter and varies between the simulations.

2.9.1 Results

All of the runs follow a similar evolution, and so here I present as an example the properties and evolution of a model where $\lambda = 0.01$, $\eta_a = 10^2$ which is shown in figure 2.5. The gas disk remains thin and cool, because the heating from the AGN is deposited only in a thin skin at the inner edge of the disk, and is not re-radiated inwards. Gravitational instabilities are visible as ring and spiral patterns, but these do not significantly thicken the disk. Instead, my cooling function causes these overdensities to cool further, and sometimes to collapse and form stars.

The thin skin region on the inner edge of the disk receives strong radiation pressure in addition to heating, causing the inner gas to be pushed outwards as a warm wind. The thermal pressure of the gas pushes it vertically, thickening the outflow. Although the gas of this wind reaches temperatures of $10^3 - 10^4$ K, the dust component is significantly cooler, and is not destroyed by sublimation or sputtering. The opacity of the gas therefore remains large, and the gas continues to be pushed outwards. Overall, the outflow produced is more radial rather than polar. It is likely that the inclusion of re-radiation of infrared radiation between gas particles would provide an additional vertical force through radiation pressure (see the next chapter).

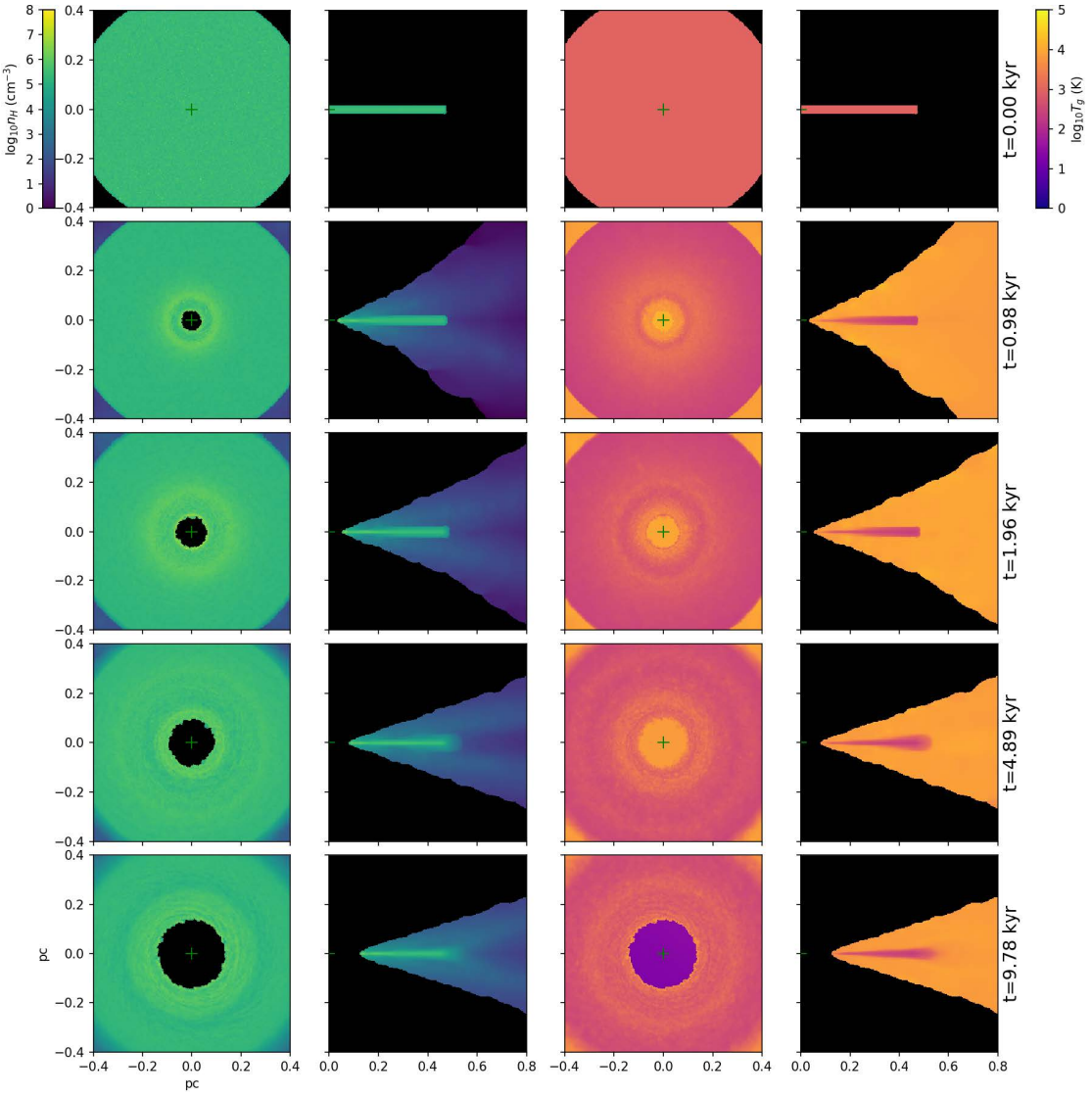

FIGURE 2.5: Figure taken from Williamson et al. (2019): Evolution for $\eta_a = 10^2$ and $\lambda_{\rm Edd}$=0.1. Left: face-on and edge-on mass weighted mean densities. Right: face-on and edge-on mass-weighted mean temperatures.

The inner radius of the disk slowly expands throughout the simulation. This is partially a result of the inner edge of the disk being ablated through heating and radiation pressure, but is also a result of the net momentum deposition on the disk as a whole from radiation pressure. Most of the deposited momentum is carried off in the wind, but some is transferred to the bulk of the disk, pushing the disk outwards.

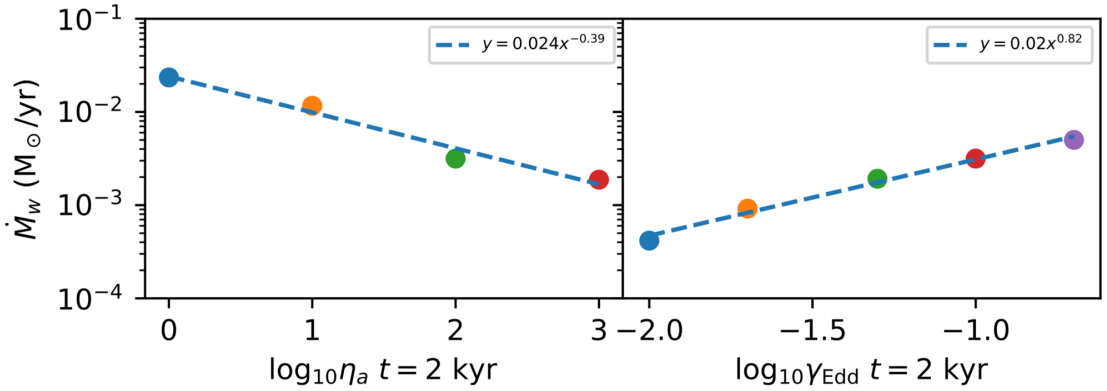

FIGURE 2.6: Figure taken from Williamson et al. (2019). Outflow rate varying the anisotropy factor η_a and the Eddington ratio, denoted here as γ_{Edd}.

2.9.1.1 Effect of anisotropy

A number of simulation parameters are varied between the runs. In figure 2.6 is shown the dependency of the mass outflow rate on the anisotropy factor and the Eddington ratio at t = 2 kyr. The mass outflow rate is defined as the rate at which gas particles join the wind, i.e. reach a velocity greater than the escape velocity from the gravitational potential within 5 pc. This cut-off radius is used so that particles that join the wind earlier in the simulations do not affect the results. Considering the runs varying the Eddington ratio it is shown that a greater $\lambda_{\rm Edd}$ produces a higher mass outflow rate, following a power-law trend with index ~ 0.8. More critically, it is found a strong dependence of the mass outflow rate on the anisotropy, showing a power-law trend with index ~ 0.4. Here, the more isotropic the radiation field the more flux enters the equatorial plane of the disk, blowing out the wind more rapidly. This demonstrates that the anisotropy factor should not be neglected when studying the wind evolution, as the sensitivity of the outflow rate is of similar strength to the sensitivity of the Eddington factor, within a factor of 2. Additionally, in Williamson et al. (2019) it is shown how both anisotropy and Eddington factor are equally important in shaping the wind. As expected, at lower anisotropies the wind is pushed outwards more radially, because the radiation pressure increases while the gas maintains a similar thermal pressure. Similarly, at higher Eddington ratio the gravitational potential remains the same, while the radiation pressure is higher and the outflow becomes more radial. This again emphasizes the importance of the anisotropy factor, which can have a dramatic effect on the outflow properties as

much as the Eddington ratio.

2.9.1.2 Obscuration properties

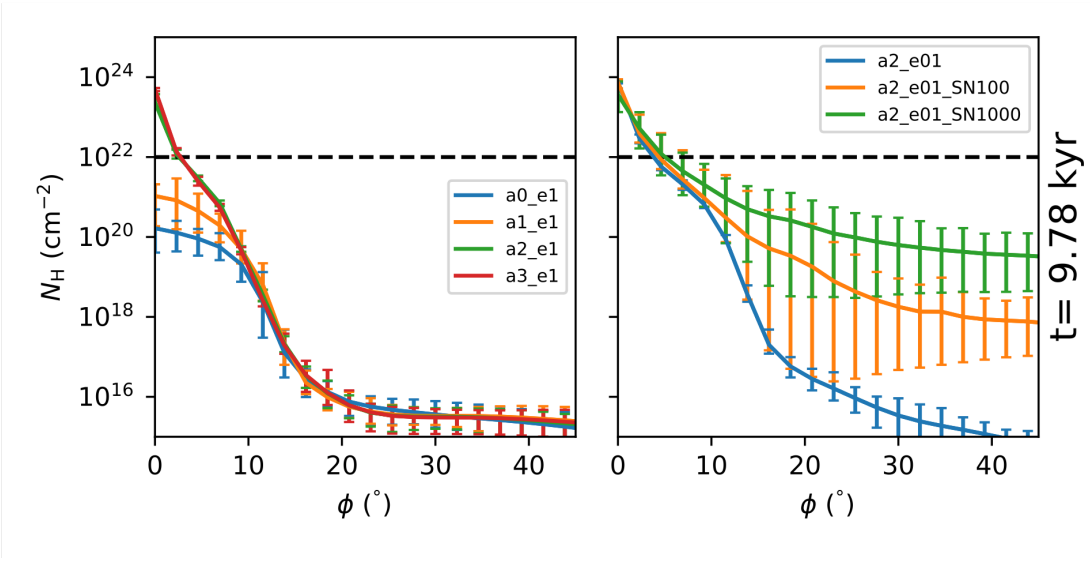

FIGURE 2.7: Figure taken from Williamson et al. (2019). Mean column densities at t = 9.78 kyr as a function of inclination from the disk plane ϕ.

One question that might arise is whether or not the wind produced by the simulations respects the toroidal obscuration properties required by AGN unification theories. The column density for each angle can be calculated by tracing rays from the center of the simulation outwards, and summing the contribution to column density across all particles that intersect the ray. The mean, maximum, and minimum of each set of rays for all runs at t = 9.78 kyr are plotted in Figure 2.7. The runs including supernovae feedback are labeled using *SN* in the naming scheme. Supernovae do have an effect at more polar angles, propelling small amounts of gas and dust to large heights about the disk. However this effect does not greatly change at lower inclination. Overall, the simulations all have remarkably similar column density profiles, with differences between runs appearing for a very small amount of the gas. It is noticed that the obscuration produced is not enough to represent the thicker 'torus' we expect from the high covering fractions found in observations. This provides additional support to the idea that the infrared radiation, not included in the RHD model, could be a necessary ingredient to puff up the torus and get the extinction required by AGN unification.

2.9.1.3 Kinematics

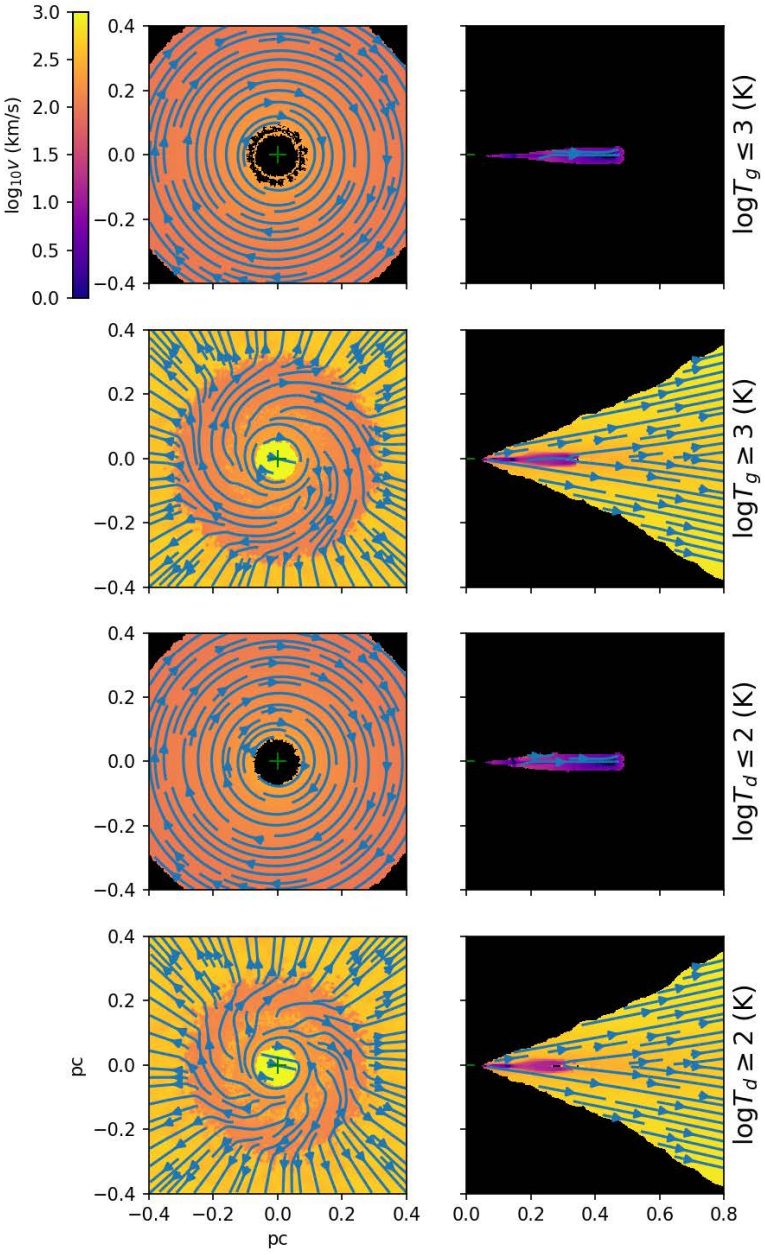

FIGURE 2.8: Figure taken from Williamson et al. (2019). Mass-weighted mean velocities of dust and gas temperature above and below threshold temperatures, for run having $\eta_a = 10^2$ and $\lambda_{Edd} = 0.01$ at t = 1.96 kyr. Left column: face-on view. Right-column: azimuthally wrapped view. The color-map gives the magnitude of the velocity, and the streamlines give the direction.

With the aid of phase plot diagrams, it has been shown that the disk phase can be isolated by applying cuts using either gas or dust temperature. T_d = 100 K and T_g = 1000 K have been selected as threshold temperatures. The plot the velocity of gas above and below these thresholds is shown in figure 2.8. Both the gas and dust temperature cuts

select qualitatively similar velocities, which is expected as there is a correlation between dust and gas temperature, at low gas temperature. Material with temperature below either cut shows strong rotation, while material above either cut is strongly outflowing. This suggests that observational tracers of hot/cold gas will respectively trace hot/cold dust and vice versa, and that tracers of hot material should observe outflowing gas, and of cold material should observe indicators of rotation.

2.10 Large-scales RHD simulations

The large-scale simulations are presented in Williamson et al. (2020). It is a complementary work of Williamson et al. (2019), extending the parsec scales model to a larger physical domain, 1-100 pc, so that results can be directly compared to observations, specifically to the large-scale images obtained with ALMA (see section 1.6.2). This approach can furthermore provide insights into whether or not the diversity of small-scale simulations leads to a diversity of large-scale outflows scenarios. At the same time, it tests the outflows geometries invoked by radiative transfer to explain the observed spectra.

Like the first small-scale model, the basic dynamical picture is a dusty gas disk, impacted by the radiation pressure of an AGN that emits anisotropically. In this set of simulations, the scales at which winds are produced are now unresolved and the wind is artificially injected in the inner regions. The dynamical evolution of the dusty disk is modeled using the SPH method described in section 2.2.1 and the set of Cloudy models described in section 2.4. The main difference with respect to the small-scale model is the wind injection model and the inclusion of sub-grid physics. The generation of the wind is based on a number of parameters. These are the mass generation rate, the initial radial velocity, the radius where winds are injected, the inclination of the center of the generation region and the (unresolved) wind launching radius. The sub-grid model corresponds to the unresolved "inner torus" region where internal radiative transfer effects (such as vertical support from infrared radiation pressure) are more significant.

Sub-grid extinction is assumed to be axisymmetric. The optical depth follows a split linear function. This is given by:

$$\tau = \begin{cases} \tau_0 - \phi/\alpha_E & \phi \leq \phi_T \\ \tau_0 - \phi_T/\alpha_E - (\phi - \phi_T)/\beta_E & \phi \geq \phi_T \end{cases} \tag{2.17}$$

where τ_0 is the optical depth along the inner torus plane, α_E is the optical depth slope for the dense equatorial part of the inner torus, β_E is the optical depth slope for the higher inclination region of the inner torus, and ϕ_T is the inclination of the transition between these two regimes. This type of profile is produced in the small-scale simulations (see figure 2.5). The parameters are adjusted to represent the thicker 'torus' we expect from infrared radiation pressure, using a larger ϕ_T and a lower α_E than predicted by the small-scale model where infrared radiation pressure is not included.

2.10.1 Results

The simulations are performed varying a number of parameters between runs, specifically the anisotropy of the input radiation field, the sub-grid extinction profile, the wind mass input rate, the initial velocity of the input wind, and the range of inclinations of wind particles.

The ensemble of runs which has been performed shows that the polar extended infrared emission is almost ubiquitous, as inferred by observations (Asmus, 2019). Figure 2.9, 2.10 and 2.11 show the typical evolution of the wind. An outflow can evolve into a polar wind after being accelerated by the anisotropic radiation of the AGN accretion disk. Provided the initial outflow speed does not vastly exceed the escape velocity, the equatorial component of the wind tends to 'fail', as it receives less radiation pressure from the accretion disk. The gas flows can penetrate each other as the wind falls back down to the disk, forming clumps. The vertical component always persists, even with near-zero initial outflow speeds. Vertical winds therefore do not strongly depend on the initial wind launching mechanism, and polar extensions of dusty gas should be expected to be common. The wind evolves into a hollow-cone structure, consistent with the

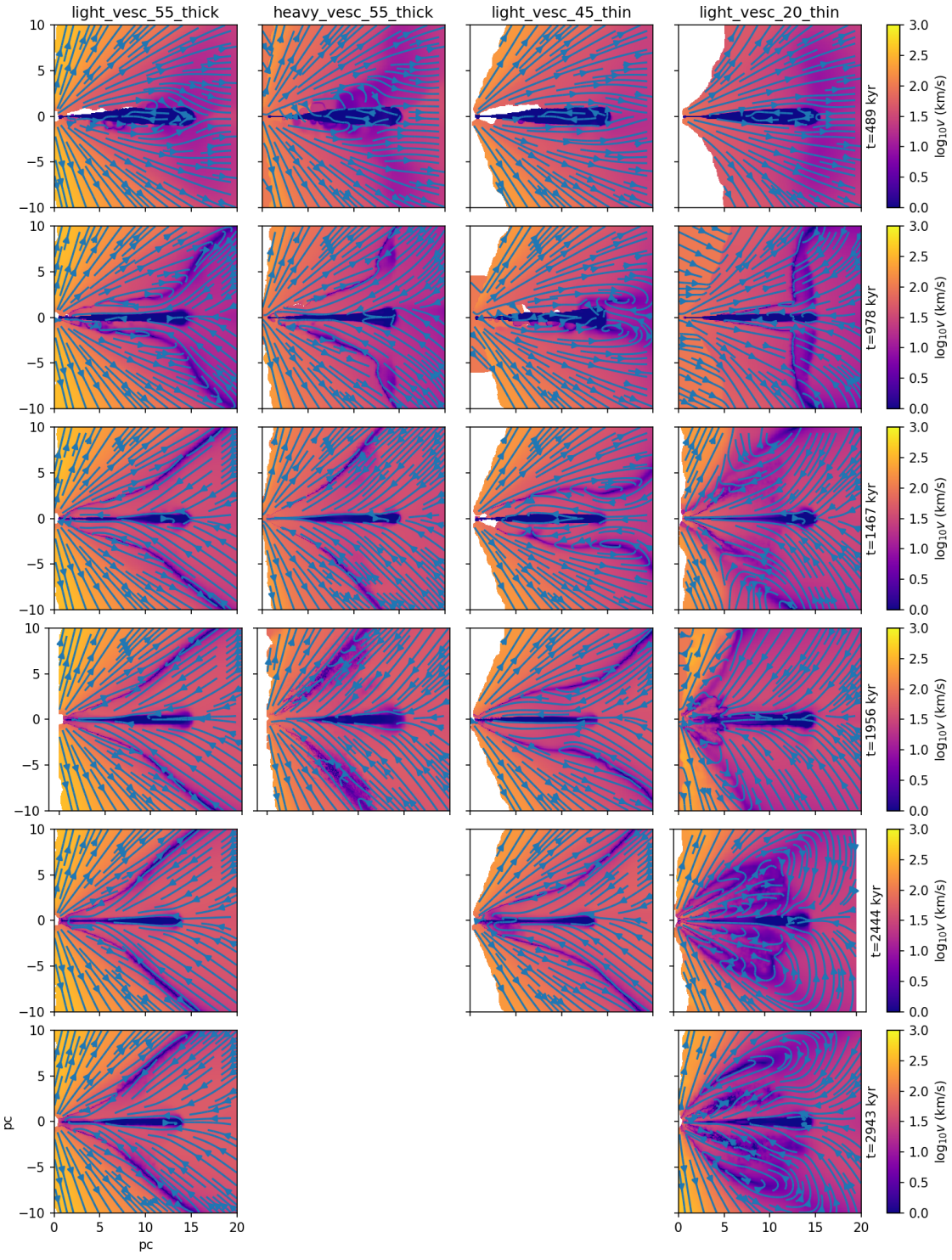

FIGURE 2.9: Evolution of azimuthally averaged velocity fields of four sample full-scale runs. Figure taken from Williamson et al. (2020).

assumptions made from RT models of observations, providing justification for the use of disk+wind geometries invoked to explain the observed IR emission. The cone has a parabolic shape, while some RT models imply a hyperbolic structure (Stalevski et al., 2019), which may require the inclusion of infrared radiation pressure from the AGN's

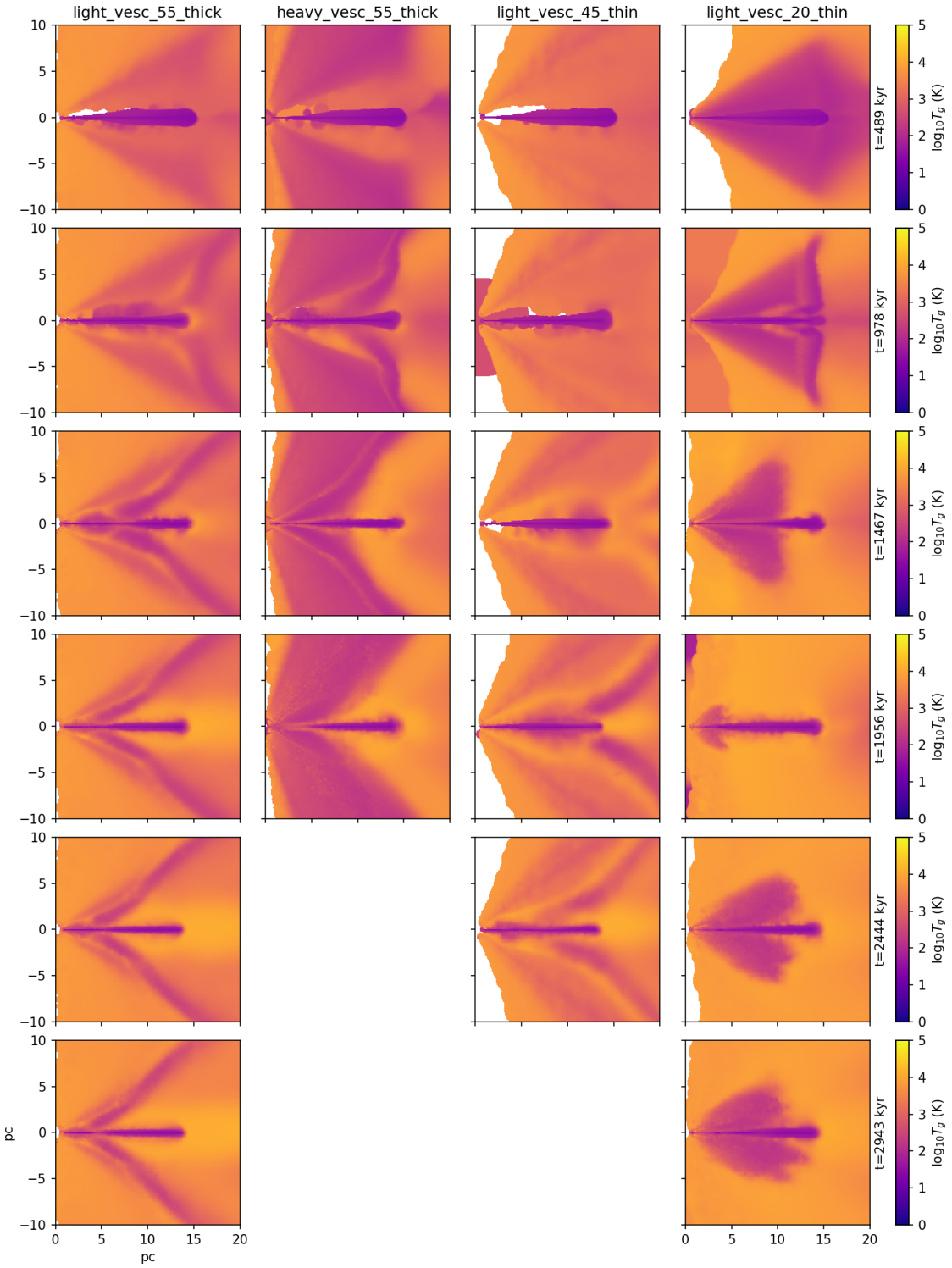

FIGURE 2.10: Evolution of azimuthally averaged temperature distribution of four sample full-scale runs. Figure taken from Williamson et al. (2020).

dusty disk to be produced. The velocity maps of the simulations are complex, even when the simulation geometry is fairly simple. From the plot of the mean line-of-sight-velocities (figure 2.12) it is possible to note apparent 'counter-rotating' features, as found

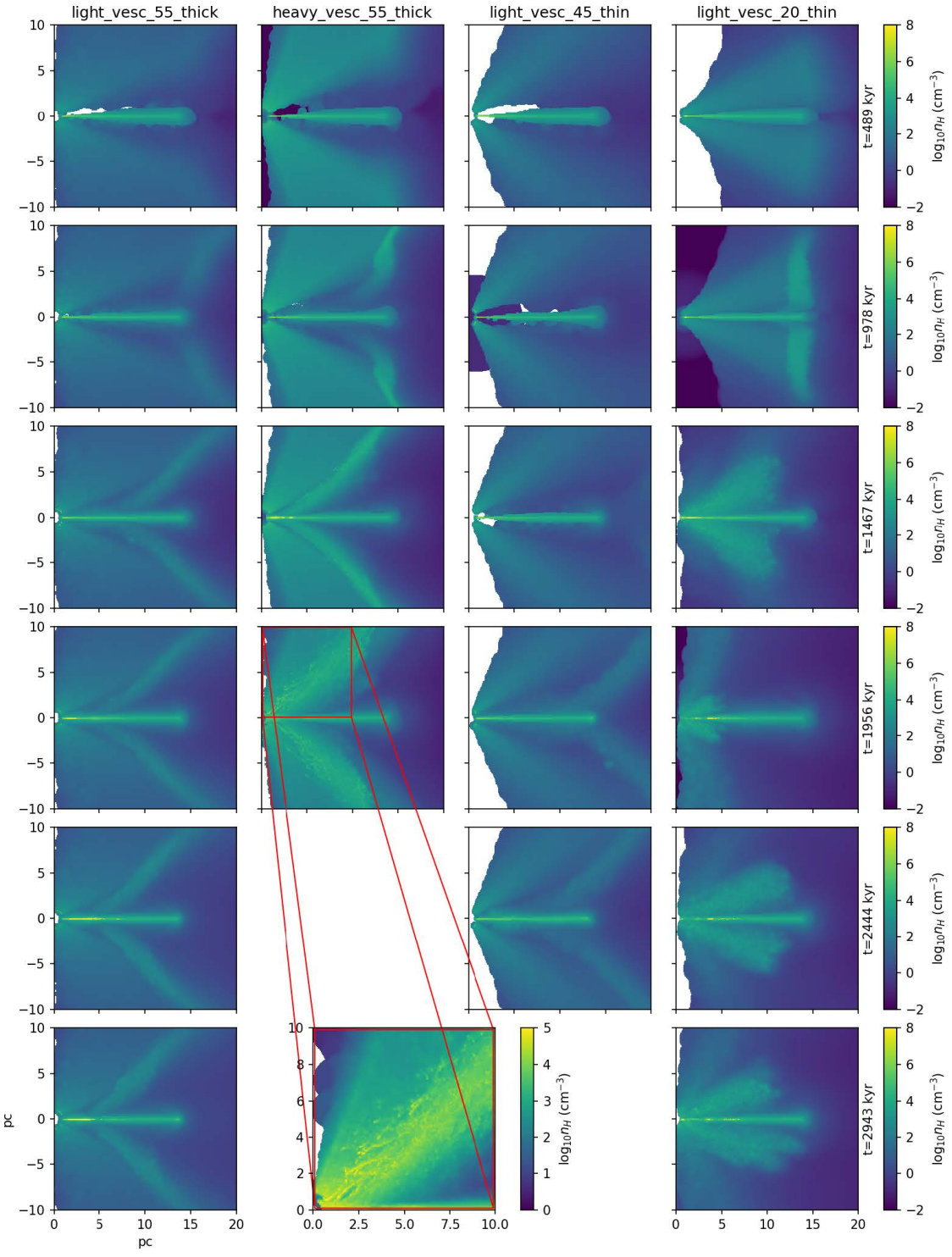

FIGURE 2.11: Evolution of azimuthally averaged density distribution of four sample full-scale runs. A zoom panel shows the clumpy structure in one run (note the different color scale). Figure taken from Williamson et al. (2020).

in observations. However, it is noted that there is no a real counter-rotating component, as this results from inflows superimposed on outflows through the line-of-sight.

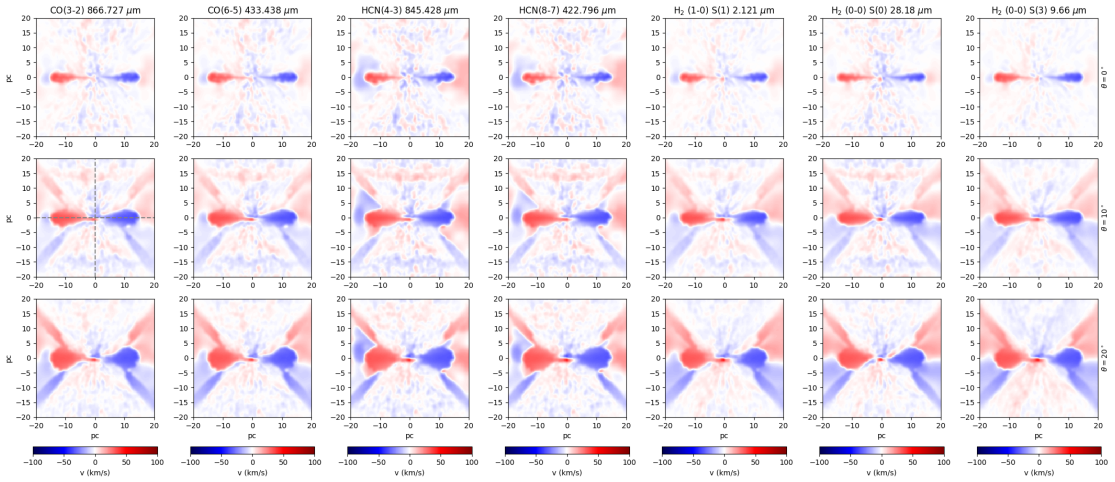

FIGURE 2.12: Mean los velocities at t = 2 Myr. Figure taken from Williamson et al. (2020).

2.11 Coolants in the small-scales simulations

The goal of this section is to highlight one powerful application of the CLOUDY tables I produced for the RHD model, in a context non exclusively relevant to hydrodynamics simulations. In the following, I use the CLOUDY tables to predict the dominant coolants emerging in the dusty environment of AGN.

The calculations use the small-scales RHD to select the range of physical conditions relevant to the disk and wind phase. Specifically, they consider the typical density, temperature and column density characterising SPH particles at a given radial distance from the AGN. This set of parameters allows finding the corresponding CLOUDY run and search for the dominant coolants in the output file.

Figure 2.13 summarises the result of this study with a schematic diagram on the top to facilitate the reading. Note that the labels in the legend are generated by the CLOUDY code, and hence it follows its naming convention scheme as specified in the caption.

To perform the calculation, I adopt a polar coordinates system and the cooling contributions in the radial direction are averaged in thin angular slices. It worth noticing that the cooling contribution is not necessarily associated with a strong line emission, as the number of particles used to compute the mean varies in each point, with a higher concentration in the innermost regions. I use the run 'a2_e01' of the RHD model and focus the analysis on the central pc. The domain of the polar coordinate θ is $0° \leqslant \theta \leqslant 12°$ where $\theta = 12°$ is the maximum angle reached by SPH particles for this particular simulation.

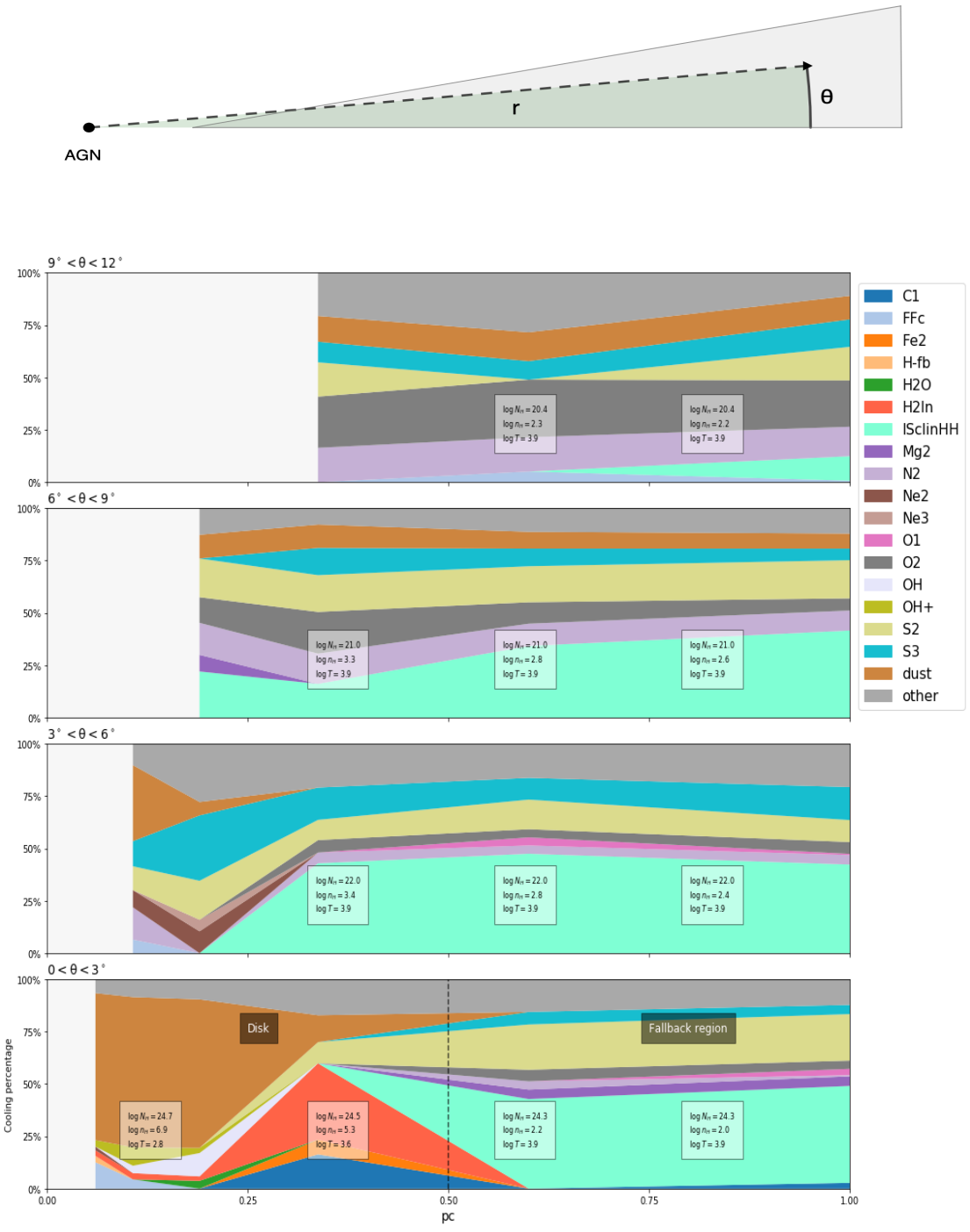

FIGURE 2.13: Dominant coolants in the wind launching regions with a schematic diagram at the top showing the calculation setup. Here, the labels in the legend are generated by reading the output from CLOUDY and hence following its naming convention scheme. This means that names such as "S2", "O2", etc. denote single-ionised species (S II, O II, etc.), while "C1", "O1", etc. denote neutral species.

Each row in the figure shows the average contribution of different coolants, and each colored area corresponds to a different cooling agent. The bigger the area, the bigger the contribution. The total of the stacked areas is always 100%. Contributors fainter than 0.05 of the total are grouped under the label "other".

2.11.1 Dominant coolants in the disk and fallback region

The bottom chart of figure 2.13 shows the major coolants in the disk and fall-back region - i.e. the gas which has been blown out of the system is falling back inward, forming a fountain or failed wind (see also Hönig, 2019). Their separation is highlighted by a dashed black line. Dust represents the major coolant in the inner sublimation region 1-5 r_{sub} (r<0.3 pc). There is also a significant contribution from free-free emission at the inner edge together with OH, OH^+ and S II. This is the densest region and there is some contribution from molecular species, H_2 and H_2O. Molecular hydrogen becomes dominant in the outer part of the disk $r \gtrsim 0.3$ pc ($r \gtrsim 5\ r_{sub}$) where the density is slightly lower density and the temperature hotter. Significant coolants in the outermost region of the disk are hydrogen (labelled under "ISclinHH"), S II and C I. Hydrogen becomes the dominant coolant in the hotter and less dense fallback region, although there is a persisting important contribution from S II. Additional contribution to the cooling is provided by S III and other low-ionisation species such as O II, N II and Mg II.

2.11.2 Dominant coolants in the wind and disk-wind transition region

Although there are some key trends, separating the outflow from the disk component is not straight-forward. The transitional region is most likely to lie in the region $3° < \theta < 6°$. This region presents a coherent significant contribution from S II and S III. Cooling from dust is confined to the innermost region, while hydrogen becomes the most important coolant at larger distances. Minor contributions come from O I, O II and N II. The wind layer $6° < \theta < 9°$ keeps featuring a strong contribution from the sulphur lines, S II and S III. In contrast with the transitional region, O II and N II become now the dominant coolants and the dust contribution is not confined to the innermost region, but remains significant throughout the outflow. Line cooling from hydrogen in

this region is still very prominent. This trend does not significantly change in the last layer of the wind, except for the hydrogen contribution which decreases drastically.

2.11.3 Discussion

The inner part of the dusty molecular disk has a strong contribution from dust. This region is also characterised by the largest number of particles so it is likely associated with a strong infrared emission and hence radiation pressure. Even if the infrared re-radiation is not included in the RHD simulations, this will tilt the wind more in the vertical direction, as shown in the next chapter. At r$\sim$5 r_{sub} the dominant coolant is represented by H_2. The hotter temperature and lower density will possibly provide a higher scale-height for H_2, as observed in (Hönig, 2019). The properties of the fall-back region are still not very well known, so it is interesting to discuss these as well. The density and temperature of this region are similar to the ones found in the wind, except that the column density is higher. As a consequence, the coolants in this region are also present in the wind, most noticeably S II, S III, O II and N II The only difference from the wind is the contribution to the cooling from Mg II which is coherently present throughout the fall-back region.

2.12 Summary and conclusions

I presented a new three-dimensional radiation hydrodynamics model of a dusty gas disk fully exposed to an AGN source, giving detail of how I contributed to the research work. The model considers only the radiation coming from the central AGN, neglecting the IR re-radiation. The dynamical evolution has been presented first in the small-scales regime ($\sim$ 1 pc), where the wind is produced, then in a larger scales model ($\sim$ 1-100 pc) where results have been compared to observations. The RHD code implements SPH, a particles-based Lagrangian formulation of hydrodynamics, used for the first time in simulations of AGN dusty tori. This numerical method has the ability to provide very high resolution in dense regions while simultaneously capturing large length scales accurately. In the RHD code, a number of physical properties such as radiative accelerations,

flux-weighted opacities, and radiative heating and cooling rates are calculated with a series of CLOUDY models, which I designed and tabulated for interpolation in the simulation. This represents my main contribution to the RHD model. It has involved learning to work with the CLOUDY software, finding strategies when a physical property requested by the RHD code is not explicitly printed out (as in the case of the radiative accelerations and opacities) and working out the best interpolation method to deal with non-converging solutions.
Here I summarize some of the key findings from both the small and large-scales RHD model.

- The small-scales RHD model produces a two-phase structure consisting of a hot outflowing component and a cool rotating component. The hot/cold gas component corresponds to the hot/cold dust component, although the gas temperature is hotter than the dust temperature. This suggests that observational tracers of one species (gas or dust) in a certain temperature range (hot/cold) will also trace the other species (dust or gas).

- At constant luminosity, the anisotropy of radiation field is the key factor in governing the dynamics of the outflow and the disk is the flux in the plane of the disk. This emphasizes the importance of constraining the anisotropy of the radiation field of the central engine of the AGN - the outflow rate is sensitive to the anisotropy factor almost as much as it is sensitive to the Eddington factor.

- In the small-scale model, supernovae only have a modest effect in increasing the covering fraction of the wind.

- In the large-scale model, polar extended infrared emission results to be almost ubiquitous. An outflow can evolve into a polar wind after being accelerated by the anisotropic radiation of the AGN accretion disk. Provided the initial outflow speed does not vastly exceed the escape velocity, the equatorial component of the wind tends to 'fail', as it receives less radiation pressure from the accretion disk. The vertical component always persists, even with near-zero initial outflow speeds. Vertical winds therefore do not strongly depend on the initial wind launching mechanism, and polar extensions of dusty gas should be expected to be common.

- The large-scale model produces a hollow-cone structure, consistent with the results from RT models of observations. Overall, the large-scale 3D RHD simulations provide the physical justification for the use of disk+wind RT models that show a universally better match to the observed SEDs and interferometry than classical torus models (Hönig and Kishimoto, 2017; Stalevski et al., 2017, 2019).

- The velocity maps of the simulations are complex and simulations reproduce 'counter-rotating' features, as found in observations (Impellizzeri et al., 2019).

Both small and large-scale simulations results emphasise the importance of IR the radiation pressure in shaping the appearance of the outflows to match observations. I will address this topic in the next Chapter.

Finally, I demonstrated how the use of my CLOUDY can be extended beyond the RHD simulations. In particular, I determined the dominant coolants emerging in the dusty environment of AGN and discussed properties of regions that are still not very well known, as the wind fall-back region.

Chapter 3

The role of infrared radiation pressure in shaping dusty winds in AGN

> "Most of the fundamental ideas of science are essentially simple, and may, as a rule, be expressed in a language comprehensible to everyone."
>
> Albert Einstein

This chapter is based on my first author paper Venanzi et al. (2020) I conceived, carried out, and wrote up all the work myself.

3.1 Overview and Context

The RHD simulations only consider the central AGN engine as source of radiation and neglect the effect of the IR emission by dust. The reason behind this choice is the noticeable computational cost that the inclusion of the IR re-radiation involves. Only very few groups have attempted to include an approximate form of the IR re-radiation

(Dorodnitsyn et al., 2016; Chan and Krolik, 2016). In this section I lay out a simplified semi-analytical framework to calculate the effect of infrared radiation pressure on dusty gas. I assume the gas to be clumpy and treat the clumps as "test particles" with physical properties obtained by photoionisation simulations. This approximation allows to characterise the role of IR radiation pressure on the distribution of material around the AGN. The simulations include a treatment of gravity, radiation pressure from the AGN and the re-radiation from the hot dust itself using an ad-hoc geometric setup. The goal is to reproduce qualitative and quantitative properties of the dusty region and compare them to observations

3.2 The model

In this section I lay out my analytical framework to quantitatively assess the spatial distribution of the forces acting in the parsec-scale dusty environment of an AGN. The basic setup of the model is shown in figure 3.1. In the following, I consider a geometrically thin disk consisting of dense clumps of gas and dust. The physical properties of these clumps are inspired by Namekata et al. (2014), who performed RHD simulations of gas clouds exposed to AGN radiation. It has been shown that dust clumps or clump fragments can survive under such extreme conditions if they have hydrogen density values in the range $10^{6.5}$ - 10^{8} cm^{-3}. Throughout this work, I assume a hydrogen number density of $n_H = 10^7\,\mathrm{cm}^{-3}$.

I consider column densities from 10^{22} to 10^{24} cm^{-2}. The lower limit of 10^{22} cm^{-2} corresponds to the regime where $\tau_{NIR} \sim 1$, which is a condition required in order to have effective infrared radiation driving (Krolik, 2007, and references therein). I stop at $N_H = 10^{24}$ cm^{-2} because any larger column density value cannot be efficiently accelerated by the radiation pressure and would exhibit similar behaviour to $N_H = 10^{24}$ cm^{-2}, as we shall see below. Under these assumptions, I then consider the radiation and gravity force terms acting on individual clouds that sit at a certain distance from the AGN and the disk. Each of these clouds is approximated as a dusty test particle, and so I will use the terms "cloud" and "dusty particle" interchangeably.

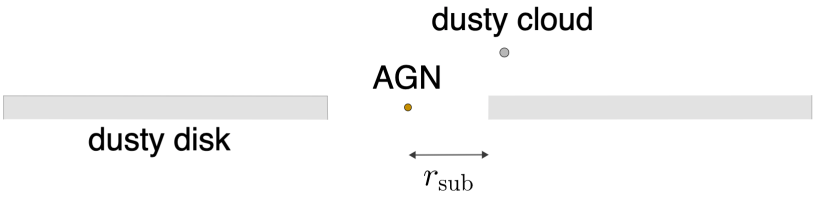

FIGURE 3.1: Schematic setup of the model. The main two components are the AGN and the dusty disk, both generating a radiation pressure on a dusty cloud and acting against the gravity force of the AGN.

3.2.1 AGN radiation field

The most dynamically important component of radiation transfer in a dusty environment is the absorption of strong optical/UV radiation from the accretion disk by dust.

A radiation field with a given monochromatic flux F_ν at frequency ν exerts an acceleration $k_\nu F_\nu/c$, where k_ν is the opacity with dimensions of area per unit mass. For a cloud sitting at a certain distance d, the monochromatic flux has the form

$$F_\nu = \frac{L_{\rm AGN;\nu}}{4\pi d^2} \tag{3.1}$$

where $L_{\rm AGN}$ is the bolometric luminosity of the AGN. Then, the net acceleration experienced by the cloud is

$$a_{\rm AGN} = \frac{\int_{\rm OUV} k_\nu L_{\rm AGN;\nu} d\nu}{4\pi c d^2} \tag{3.2}$$

where OUV denotes the optical/UV frequencies range of interest here. In a dense cloud dust and gas are tightly coupled via collisions, so that the radiation pressure force on the dust will be transferred to the cloud as whole. Accordingly, I treat the cloud as a single entity and further approximate the frequency-dependent opacity as the entire opacity of the cloud. If the cloud has radius $R_{\rm cl}$ and mass $m_{\rm cl}$, then the opacity of the cloud $k_{\rm cl}$ can be expressed as

$$k_{\rm cl} = \frac{\pi R_{\rm cl}^2}{m_{\rm cl}} \tag{3.3}$$

i.e. the cloud geometrical area divided by its mass. Therefore, Eq. (3.2) reduces to

$$a_{\rm AGN} = k_{\rm cl} \frac{L_{\rm AGN}}{4\pi c d^2} \tag{3.4}$$

allowing a direct proportionality between the radiative acceleration from the central AGN and its total luminosity. The cloud mass $m_{\rm cl}$ can be written as $m_{\rm cl} = m_{\rm p} n_{\rm H} \frac{4}{3} \pi R_{\rm cl}^3$, with $n_{\rm H}$ being the hydrogen number density of the cloud. At the same time the radius of the cloud $R_{\rm cl}$ can be estimated as $R_{\rm cl} = N_{\rm H}/2n_{\rm H}$. Then,

$$k_{\rm cl} = \frac{3}{2} \frac{1}{m_{\rm p} N_{\rm H}} \quad . \tag{3.5}$$

3.2.2 Gravity

The gravitational acceleration has the same d^{-2}-dependence as the AGN radiation pressure, but pointing in the opposite direction, i.e. towards the central black hole. Therefore, it is convenient to express these two kinds of central forces in terms of their strength ratio.

In doing so, I recall some important classical definitions I defined in section 1.2. One is the Eddington limit, defined as the luminosity capable of balancing the gravity of a mass M

$$L_{\rm Edd} = 4\pi c G M \frac{1}{k} \quad . \tag{3.6}$$

For a fully ionised gas, the opacity k can be expressed as $k = \sigma_{\rm T}/m_{\rm p}$, where $\sigma_{\rm T}$ is the Thomson cross section. Also, I assume that gravity is dominated by the black hole mass so that $M = M_{\rm BH}$. Then, one can introduce the Eddington ratio

$$\lambda_{\rm Edd} = \frac{L_{AGN}}{L_{\rm Edd}} \tag{3.7}$$

allowing to express the ratio between the AGN radiative acceleration and gravity as

$$\frac{a_{\rm AGN}}{a_{\rm g}} = \frac{3}{2} \frac{\lambda_{\rm Edd}}{\sigma_{\rm T} N_{\rm H}} \quad . \tag{3.8}$$

This relatively simple equation highlights one fundamental point: clouds in the force field of an AGN are accelerated in a way that depends only on the ratio $\frac{\lambda_{\rm Edd}}{N_{\rm H}}$ (for optically thick clouds that are only partially ionised). In particular, the more powerful the AGN (*i.e.* the higher $\lambda_{\rm Edd}$), the more likely it is to drive a wind. Second, the more material

sits in the cloud (*i.e.* the higher $N_{\rm H}$), the less prone is the cloud to be uplifted, being more subjected to gravity.

With the use of Eq. (3.4) and Eq. (3.8) we can start to visualize the field of the AGN. Figure 3.2 shows the resulting distribution in a 2D grid in the plane above the disk. The disk is traced by the grey area and each point in the grid represents a dusty cloud. The acceleration in cm s^{-2} experienced by this cloud is displayed by varying its column density $N_{\rm H}$ and the Eddington ratio $\lambda_{\rm Edd}$ of the AGN system.

Using the fact that the flux at the sublimation radius $r_{\rm sub}$ is constant (Ivezic and Elitzur, 1997), all the distances are scaled with respect to $r_{\rm sub}$, allowing us to make my model actually independent of the luminosity.

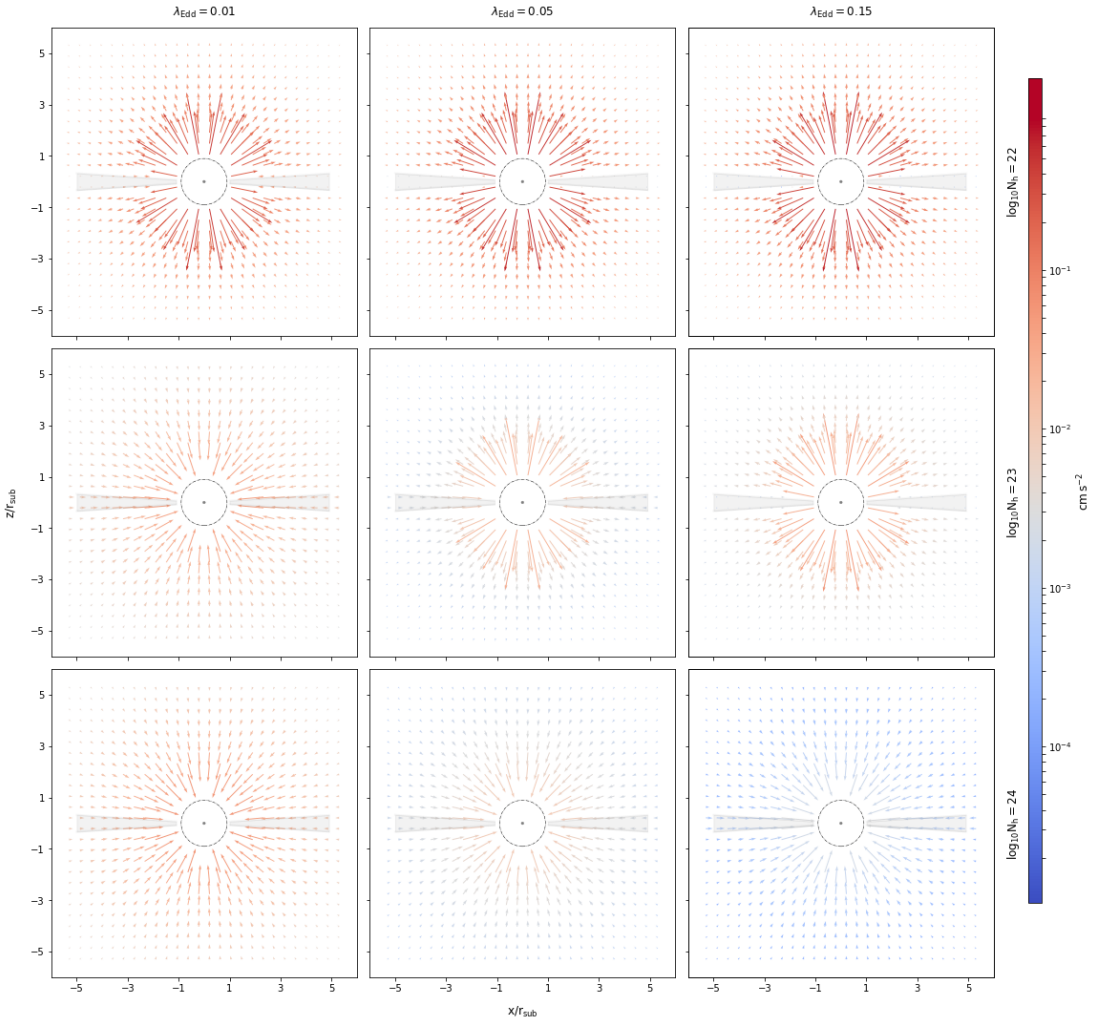

FIGURE 3.2: Spatial distribution of the optical/UV radiative + gravity acceleration field in the plane perpendicular to the disk, traced by the grey region.

3.2.3 The disk model

I assume that the AGN is surrounded by a geometrically thick dusty disk, as suggested by the disk+wind model (Hönig and Kishimoto, 2017). The disk absorbs the OUV radiation from the central AGN and re-emits in the IR. I will focus my treatment on the immediate environment close to the sublimation temperature as this is the region where the dust is hottest and has the greatest flux. Lower local temperatures and obscuration will significantly reduce the effect of the infrared radiation pressure at larger scales.

3.2.3.1 Temperature profile

Following Hönig and Kishimoto (2011), the luminosity absorbed by a dust grain at a distance r from a source of radiation is

$$L_{\rm abs} = 16\pi r^2 Q_{\rm abs;P}(T)\sigma_{SB}T^4 \tag{3.9}$$

where the $Q_{\rm abs;P}(T)$ is the plank mean absorption efficiency. For astronomical dust, the latter has a temperature power-law in the infrared of the type $Q_{\rm abs;P}(T) \propto T^{1.6}$. For clouds directly exposed to the AGN radiation pressure, I can solve for the grain temperature and obtain

$$T(r) = T_{\rm sub}\left(\frac{r}{r_{\rm sub}}\right)^{-2/5.6} \tag{3.10}$$

3.2.4 Opacities

In order to derive the infrared emission from the disk, it is necessary to know the opacities of the dusty clouds. For this, I used again the photoionisation code Cloudy. For the input spectra I adopted a modified version of the AGN Cloudy's built-in command, as in Williamson et al. (2019). The intensity assumed is the intensity at the sublimation radius. This has been determined in the same way I did in section 2.4, i.e. by running several Cloudy simulations with fixed luminosity (I used $L_{\rm AGN} = 2.2 \times 10^{43}$ erg s^{-1}) and finding the distance of the cloud for which the illuminated face is at $T_{\rm sub} = 1750$ K, characteristic of large graphite grains. The value obtained for the incident sublimation

intensity is $I_0 = 5.6 \times 10^7$ erg cm^{-2} s^{-1}, corresponding to a sublimation radius of $r_{\rm sub} = 0.03$ pc. Once the shape and intensity of the incident radiation field has been set, I vary the column density of the illuminated medium and obtain the corresponding set of opacities.

3.2.5 Obscuration

Assuming that the disk is clumpy, I can use the formalism of Nenkova et al. (2002) to address obscuration affecting its re-emission.

For simplicity, I assume that all clouds are identical with constant hydrogen density $n_{\rm H} = 10^7\,{\rm cm}^{-3}$, varying only the column density for each model. My disk extends from $r_{\rm sub}$ to the outer radius $r_{\rm out}$ (in units of $r_{\rm sub}$). The number of clouds per unit length $N_{\rm c}(r, z)$ can be expressed in a cylindrical coordinate system with separable functions of the vertical height z and the radial distance r. The resulting distribution has the form

$$N_{\rm c}(r, z) = \mathcal{C}\eta(z)N_0 r^{-1} \tag{3.11}$$

where $\mathcal{C} = 1/\ln r_{\rm out}$ is a normalization constant, N_0 is the number of clouds along the equatorial plane of the disk, and $\eta(z)$ represents the vertical distribution of the clouds. The latter is assumed to have a smooth boundary in a form of a Gaussian as

$$\eta(z) = e^{-z^2/2H^2} \tag{3.12}$$

mimicking an isothermal disk. To minimize the number of free parameters, I have explicitly fixed the radial power-law exponent to -1, $N_0 = 7$, $r_{\rm out} = 30\ r_{\rm sub}$ and $H = 0.3\ r_{\rm sub}$. This choice will not affect the general conclusion I am driving. If I define $\mathcal{N}(s^{'}, s) = \int_s^{s'} N_{\rm c} ds$, the probability that a photon travelling from s' to s is absorbed through his path will be then $P_{\rm esc} \simeq \exp(-\mathcal{N}\tau_\nu)$ for an optical depth $\tau_\nu < 1$ (such as infrared photons) and $P_{\rm esc} \simeq \exp(-\mathcal{N})$ in the opposite limit $\tau_\nu > 1$ (UV photons). It means that the radiative acceleration acting on a cloud will be modeled differently depending on wavelength.

On the scales I am considering, I will assume that most of the emission and obscuration originates from large grains as implied by observations and modeling of the dust sublimation region (e.g. Kishimoto et al., 2007, 2011a,b; Hönig and Kishimoto, 2017; García-González et al., 2017). Thus, within the clumpy disk, the radiation is absorbed according to

$$\begin{cases} a_{\rm AGN} \rightarrow a_{\rm AGN}\ e^{-\mathcal{N}} \\ \\ a_{\rm ir} \rightarrow a_{\rm ir}\ e^{-0.1\mathcal{N}} \end{cases} \tag{3.13}$$

The factor of 0.1 for $a_{\rm ir}$ accounts for the fact that the opacities of large grains (about 1μm in size) in the near-IR are typically about a factor of 10 lower than in the optical/UV regime. Accordingly, the temperatures profile will be modified as $T(r) = T_{\rm sub}\left(\frac{r}{r_{\rm sub}}\right)^{-2/5.6} e^{-\mathcal{N}/5.6}$. The resulting curve is displayed in figure 3.3. It presents a sharp drop after 5 $r_{\rm sub}$ and is nearly constant throughout the rest of the disk.

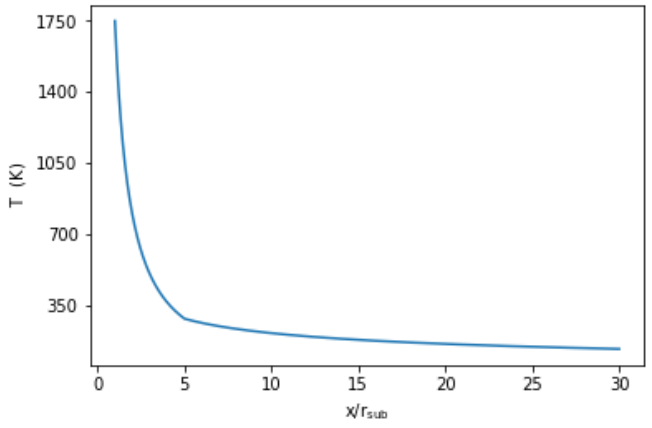

FIGURE 3.3: Temperature variation inside the disk accounting for self-shielding.

3.2.6 The infrared radiation field

Given the disk geometry of the emitting medium, one expects to break the radial symmetry of AGN radiation and gravity. To investigate this behavior, I model the dusty disk as a sequence of infinitesimally small annuli of width dr radiating as a black body, with the temperature vary radially according to eq. (3.10). The calculations have a similar setup as in Tajima and Fukue (1998). The cloud is assumed to be a point P

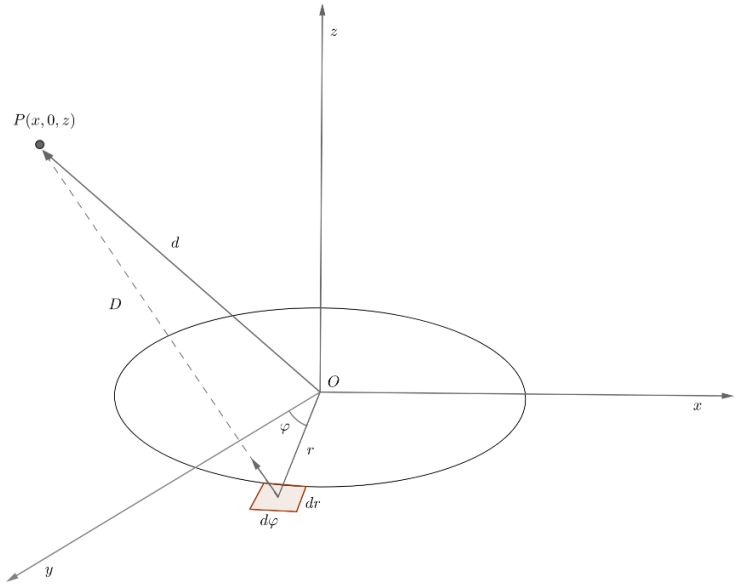

FIGURE 3.4: Geometry for the infrared emitting disk.

with corresponding (Cartesian) coordinates $(x, 0, z)$ as shown in figure 3.4. Consider an infinitesimal element of the dusty disk with polar coordinates $(r, \varphi, 0)$. The distance D from the element to the point P is

$$D = \sqrt{r^2 + x^2 + z^2 - 2\,x\,r\cos\varphi} \quad . \tag{3.14}$$

Then, the force component per unit frequency and for a single annulus of size $d\varphi dr$ are

$$da_{\mathrm{ir,x}} = \frac{k_\nu \pi B_\nu(T)\, r}{4\pi c D^2}\,\frac{(x - r\cos\varphi)\, d\nu\, d\varphi\, dr}{D} \tag{3.15}$$

$$da_{\mathrm{ir,y}} = \frac{k_\nu \pi B_\nu(T)\, r}{4\pi c D^2}\,\frac{(y - r\sin\varphi)\, d\nu\, d\varphi\, dr}{D} \tag{3.16}$$

$$da_{\mathrm{ir,z}} = \frac{k_\nu \pi B_\nu(T)\, r}{4\pi c D^2}\,\frac{z\, d\nu\, d\varphi\, dr}{D} \quad . \tag{3.17}$$

I numerically integrate expressions (3.15),(3.16),(3.17) for fixed points and visualize them in figure 3.5. It stands clear now that the radial symmetry is broken, with the disk geometry causing a vertical component at the inner radius. Additionally, this is the strongest component because the thermal emission at the sublimation radius is the strongest. At larger distances, obscuration effects significantly reduce the disk emission strength. I then add the disk contribution to the gravity + AGN radiation field derived

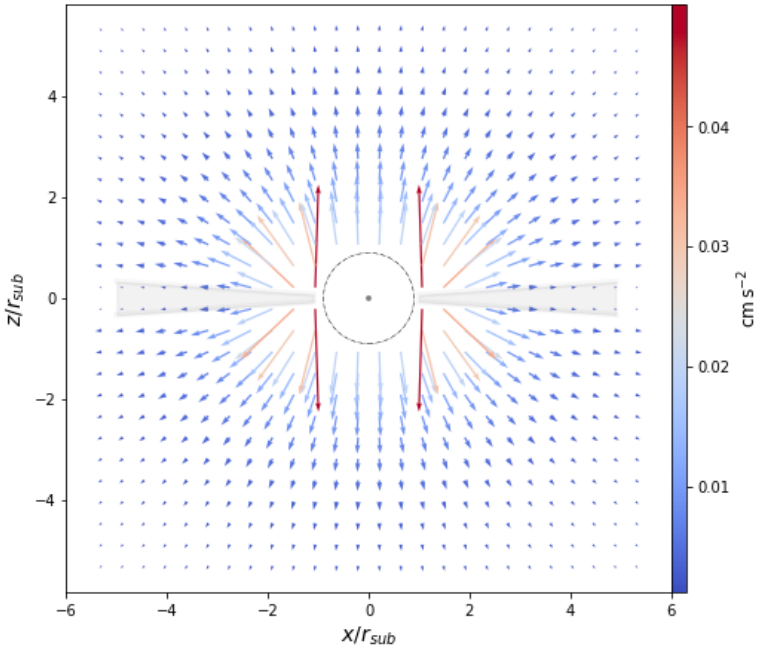

FIGURE 3.5: Spatial distribution and strength in cm s^{-2} of the radiative acceleration due to the infrared emission of the dusty disk.

in section 3.2.1 and discuss the consequences in the next section.

3.2.7 The prevalence of polar dusty winds

Combining gravity, AGN radiation pressure, and IR radiation pressure leads to a force field as shown in figure 3.6. This needs to be compared to figure 3.2 without the IR radiation pressure to appreciate the influence of the IR radiation field.

Overall, it is noted that dusty particles with $N_{\rm H} = 10^{22}$ cm^{-2} are strongly accelerated by the AGN radiation with its characteristic radial profile, and that the infrared contribution is not significantly affecting this scenario. At $N_{\rm H} = 10^{23}$ cm^{-2} and for $\lambda_{\rm Edd} = 0.05$ we observe the emergence of a wind from particles at the base of the disk that are driven more vertically instead of radially, indicating that the infrared radiation is initiating the wind, rather than the AGN. Furthermore, a wind starts to weakly emerge for column densities of $N_{\rm H} = 10^{24}$ cm^{-2} and $\lambda_{\rm Edd} = 0.15$ where we do not observe any outflow without the dust re-radiation.

I investigate more quantitatively the observed change in configuration, favouring the disk contribution, for the regions [$\lambda_{\rm Edd} = 0.05$, $N_{\rm H} = 10^{23}$ cm^{-2}] and [$\lambda_{\rm Edd} = 0.15$,

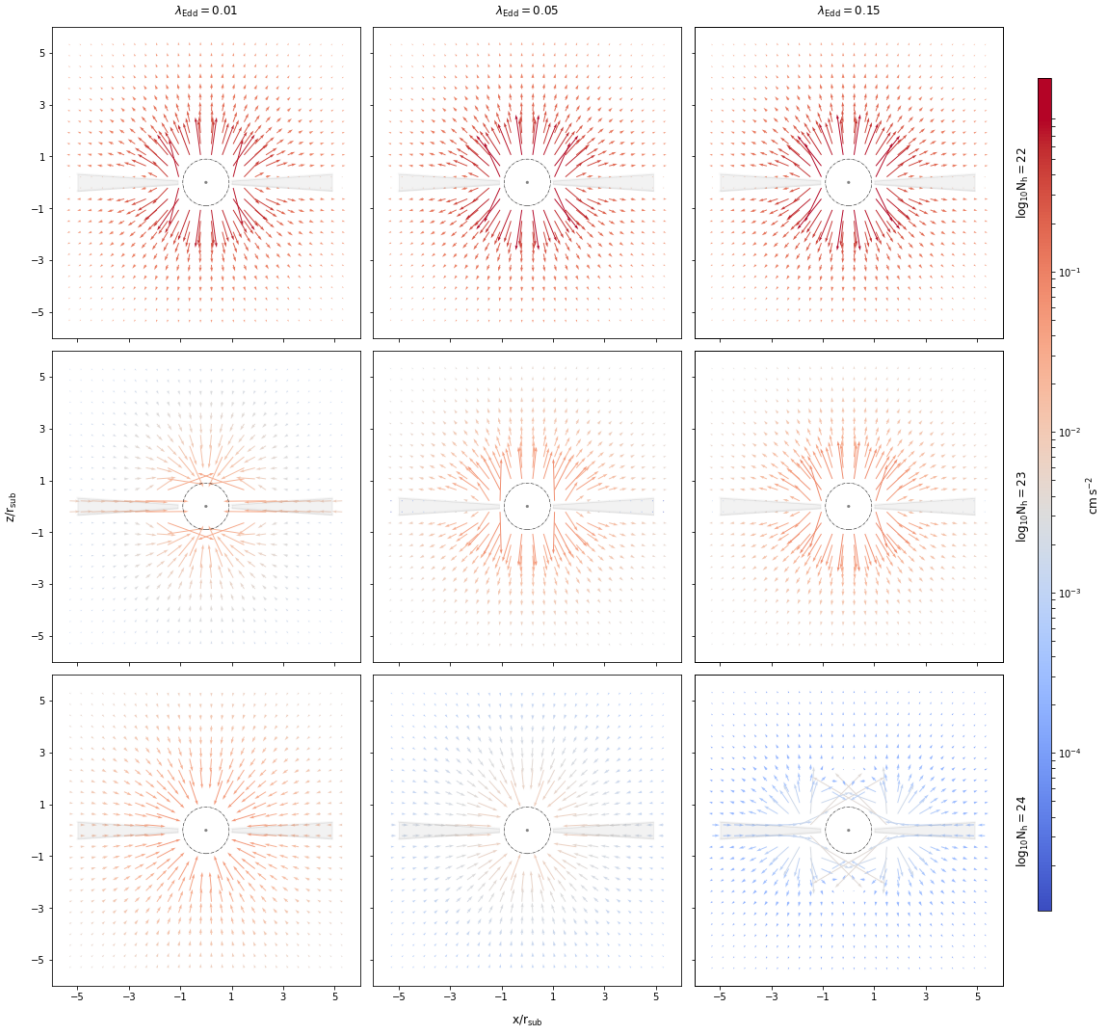

FIGURE 3.6: Acceleration field accounting for the total gravity + AGN and IR radiation.

$N_{\rm H} = 10^{24}$ cm^{-2}]. In fact, one can show these values are close to the limit where the radiative acceleration from the AGN balances gravity, so that only the infrared dominates. To highlight the parameter space for which this balance happens, I can use Eq. (3.8) and equate it to unity, obtaining a linear relationship between $\lambda_{\rm Edd}$ and $N_{\rm H}$

$$\frac{a_{\rm AGN}}{a_{\rm g}} \equiv 1 \quad \rightarrow \quad \lambda_{\rm Edd}\left(N_{\rm H}\right) = \frac{2}{3}\sigma_{\rm T} N_{\rm H} \tag{3.18}$$

Results are displayed in figure 3.7 and are coherent with my hypothesis. I only show the column densities range to corresponding Eddington ratios falling in the Seyfert regime. The reader has to keep in mind that, while these sets of values might represent an infrared initiated dusty wind, one has to perform numerical simulations to capture the

final structure, which is the subject of the next session.

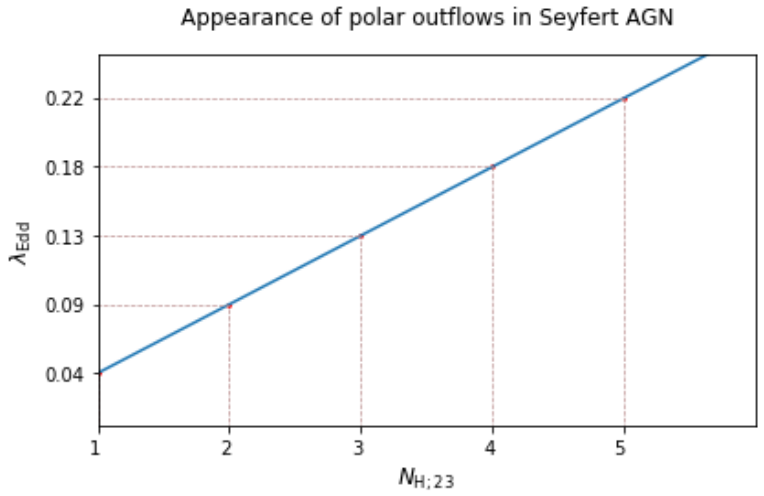

FIGURE 3.7: Critical values of Eddington ratios and column densities for which $a_{\rm AGN} \equiv a_{\rm g}$ and the disk component dominates as the only net resultant force. Here $N_{\rm H;23} = N_{\rm H}/10^{23}$ cm^{-2}.

3.3 3D radiation-dynamical simulations

With the full 3D component of the total acceleration derived in the previous sections, I can take a step further investigate how the dusty gas clouds moves in the dusty environment of AGN. The equations of motions for a cloud at distances d from the AGN are

$$\ddot{x} = -\frac{GM_{\rm BH}}{d^2} + k_{cl}\frac{L_{AGN}}{4\pi c d^2} + \frac{1}{c}\int k_\nu F_\nu^{\rm ir} d\nu. \tag{3.19}$$

where $F_\nu^{\rm ir}$ is the net infrared flux due to the disk, as derived in section 3.2.6.

The dynamics equations have been integrated using the standard leapfrog algorithm. I tested its accuracy in reproducing stable orbits against higher order integration methods and found it was performing equally well. I used an adaptive time step $dt = \eta\sqrt{\frac{4\pi}{3}\frac{d}{\max(a_i)}}$, for i running over all the three acceleration: gravity, AGN, infrared. This is just a generalisation of the commonly used time step for systems interacting with d^{-2} forces. The assumption is that $dt = \eta t_c = \eta/\sqrt{G\,\rho} = \eta(4\pi d/3a)^{1/2}$, where t_c is the characteristic timescale of interaction, η is a scaling factor, ρ is the mass density, G the gravitational constant, d is the distance to the mass and a is the acceleration, which

refers to gravity in this case. In my case, I consider the smallest interaction scaled out of gravity and radiative forces and I fix $\eta = 0.003$.

3.3.1 Radiation pressure induced sub-Keplerian rotation

I balance the initial velocity profile for the dusty particles by including the contribution of both AGN and IR radiation pressure. The azimuthal velocity as a function of the cylindrical coordinate $r = \sqrt{x^2 + y^2}$ is

$$v_\phi = \sqrt{\frac{GM_{BH}}{r} - r\ a_{\mathrm{rad};r}} \tag{3.20}$$

where $a_{\mathrm{rad};r}$ includes both AGN and infrared radiative acceleration.

Note that there are no stable orbits when radiative acceleration exceeds gravitational acceleration. Particle trajectories in this case are more likely to be driven outward in a way that depends on the combined influence of the disk and the AGN contribution for moderately to very high column density, and fully radial for the specific light obscuration case $N_{\mathrm{H}} = 10^{22}$ cm^{-2} where the AGN force strongly dominates. If I define the rotation curve as $v_\phi \propto r^{-\beta}$, I can find an analytical expression for the velocity exponent β

$$\beta \equiv -\frac{\partial \ln v_\phi}{\partial \ln r} = \frac{1}{2}\left[1 - \frac{\partial \ln}{\partial \ln r}\left(1 - \frac{a_{\mathrm{rad};r}}{a_{\mathrm{g};r}}\right)\right] \tag{3.21}$$

which reduces to the Keplerian exponent 0.5 when $a_{\mathrm{rad}} = 0$ and has no solution when $a_{\mathrm{rad};r} > a_{\mathrm{g};r}$. Trajectories in this case are are discarded from the simulations.

In figure 3.8 I plot the resultant curve for a column density $N_{\mathrm{H}} = 10^{24}$ cm^{-2}. A general property met at this column density value is that velocities are very small going closer to $\mathrm{r_{sub}}$ and this behaviour is further emphasized at higher λ_{Edd}. This trend is inverted at 1.6 $\mathrm{r_{sub}}$ where there is a remarkable departure from the Keplerian motion, in a way that again is strongly enhanced with the Eddington ratio. The value approached for $\lambda_{\mathrm{Edd}} = 0.15$ at large distances is $\beta = 0.39$.

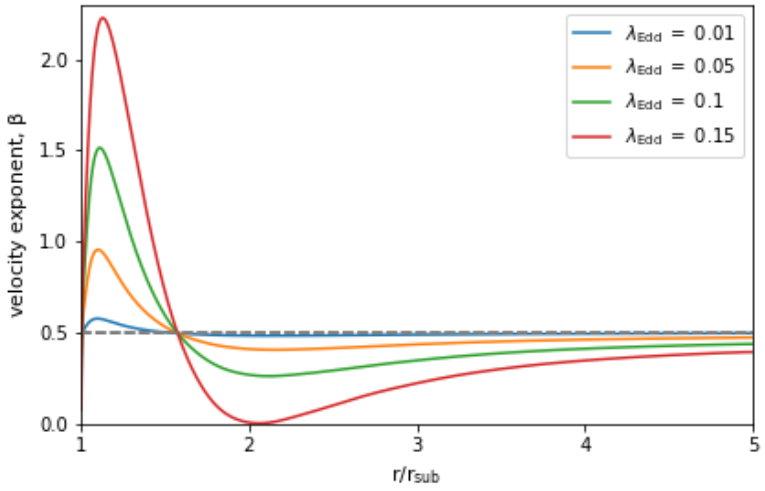

FIGURE 3.8: Velocity exponent β at the equatorial plane for column density $\log N = 24$ cm^{-2} and different values of $\lambda_{\rm Edd}$. The grey dashed line traces the Keplerian value $\beta = 0.5$. All the curves intersect and turns into sub-Keplerian at a distance 1.6 $r_{\rm sub}$.

3.4 Results

3.4.1 Impact of infrared radiation pressure

The inclusion of the IR emitting disk has two major effects. It introduces a more geometrically complex force term, featuring a strong vertical component which breaks the radial symmetry. This is due to both the disk geometry itself and the strong local temperature variation, with the hottest contribution being at the sublimation radius. It also boosts the outflow acceleration, making a wind emerge even for high column density material.

In figure 3.9 I run a set of simulations considering one of the "typical" parameters for which the vertical accelerations dominate over the radial accelerations, taking as example $\lambda_{\rm Edd} = 0.09$ and $N_{\rm H} = 2 \times 10^{23}$ cm^{-2} (see section 3.2.7). I also show how changes in the parameter values lead to different structures. The aim is to provide a feeling of the diversity of the possible dynamical configurations and it will be helpful to create a relationship between the model and observations.

At lower Eddington ratios, $\lambda_{\rm Edd} = 0.04$ and $N_{\rm H} = 2 \times 10^{23}$ cm^{-2}, material is driven away radially, being more prominently subjected to radiation pressure from the AGN. The

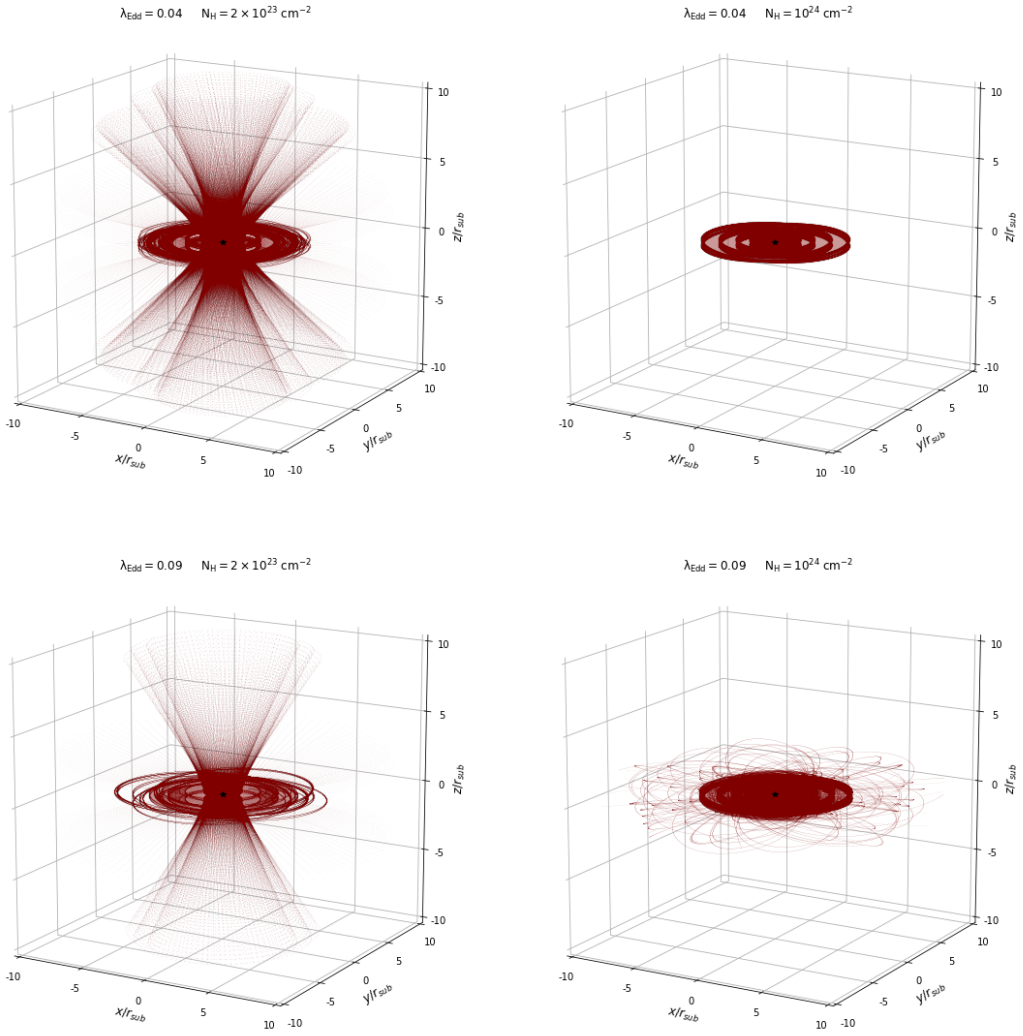

FIGURE 3.9: Example of dust and gas configuration for different values of Eddington ratio and column density.

uplift is suppressed at higher column density $N_{\rm H} = 10^{24}$ cm^{-2}, where gravity strongly dominates and all orbits are confined in a compact thick structure.

The typical scenario giving an infrared dominated wind appears when $\lambda_{\rm Edd} = 0.09$ and $N_{\rm H} = 2 \times 10^{23}$ cm^{-2}, but the final configuration is true for any values coinciding or close to the parameter space derived in section 3.2.7. The cone assumes a funnel like shape, rising vertically from the inner edge of the disk. At the same time, the dust re-radiation puffs up the disk in the region $1 - 5$ $r_{\rm sub}$. At higher column densities $N_{\rm H} = 10^{24}$ cm^{-2}, most of the orbits are bound but the higher Eddington ratio (and

hence radiation pressure) causes them to accelerate to higher scale-heights or eventually to escape radially after 1-2 orbits.

3.4.2 Sub-Keplerian motion on parsec scales

I employed an initially sub-Keplerian velocity profile that takes into account radiation pressure corrections to the gravitational potential. My logic is similar to Chan and Krolik (2016, 2017) who showed that sub-Keplerian rotation is necessary for maintaining a long-living torus in the presence of strong radiation pressure. In the present work I systematize this idea by establishing a prescription for the velocity profile based on the relative strength of the total infrared+AGN radiation pressure with respect to gravity.

A consequence of my approach is that some trajectories are naturally ruled out, as the initial velocity in Eq. (3.20) is defined by a square-root whose argument cannot be negative. This occurs every time the radiative acceleration experienced by the clouds is stronger than gravity, i.e for material with very light column density or very high accretion state. Orbits in this case are unstable, likely turning into a wind.

In figure 3.8 I have shown the resultant profile for $N_{\rm H} = 10^{24}$ cm^{-2} as the high gravitational force allows the orbits to remain bound within the disk for a large range of Eddington ratios. At this column density value, my simulations show that orbits maintain a sub-Keplerian rotation in the region 1.6-5 $r_{\rm sub}$ and they get even more sub-Keplerian as $\lambda_{\rm Edd}$ increases. The velocity exponent at large distances is $\beta \simeq 0.39$ for $\lambda_{\rm Edd} = 0.15$, consistent with the rotation curve of maser spots observed at the sub parsec scales in NGC 1068 (Greenhill et al., 1996). The inner part $r < 1.6\ r_{\rm sub}$ is characterized by very small velocities so that the actual force field will initiate an outflowing or inflowing motion. Specifically for this example and based on my previous analysis, $\lambda_{\rm Edd} \gtrsim 0.15$ is then required to observe an outflow for clouds with $N_{\rm H} = 10^{24}$ cm^{-2}.

3.4.3 Effects of anisotropic accretion disk

In the previous sections, the model assumed isotropic radiation from the central AGN. In more realistic situations, the flattened geometry of the central radiation source causes the

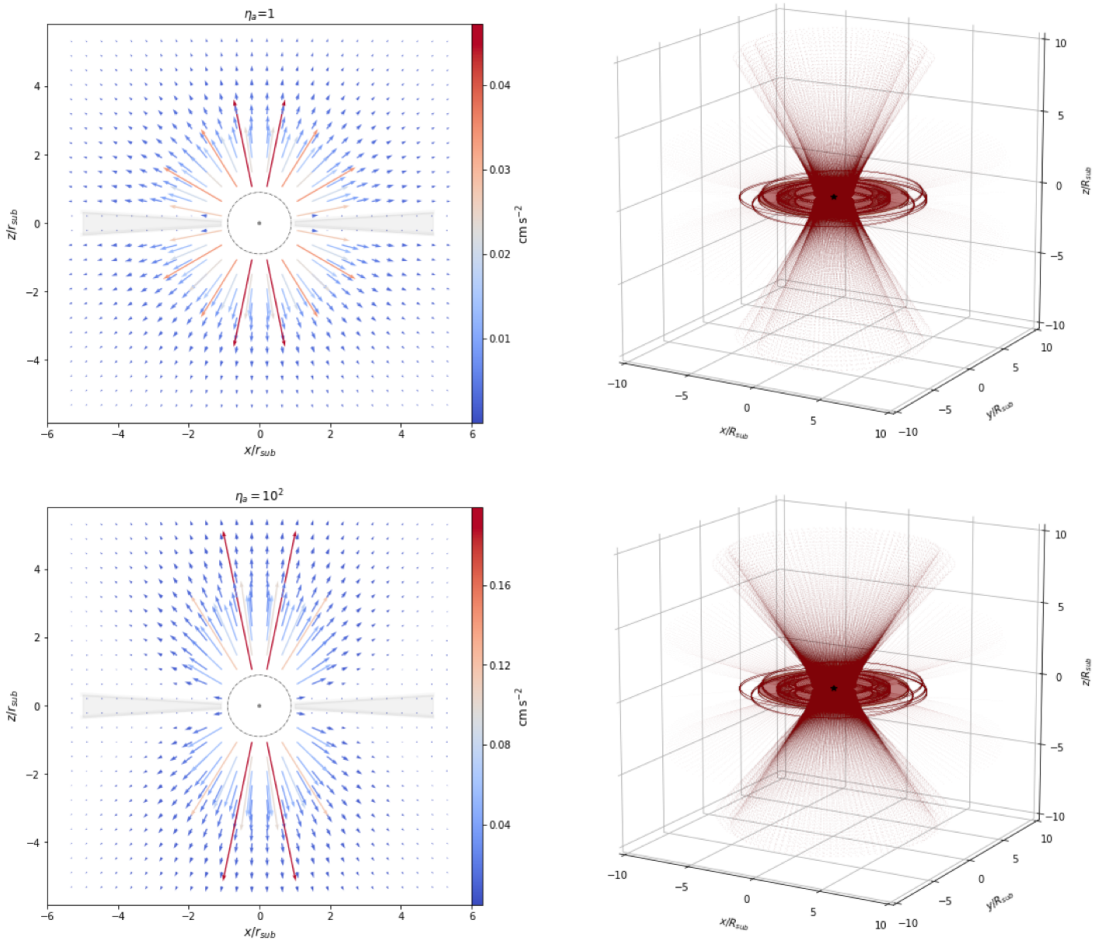

FIGURE 3.10: Comparison of the isotropic and anisotropic radiation field with $\eta_a = 10^2$. On the left panel it is shown the AGN radiation field for $N_H = 3 \times 10^{23}$ cm^{-2} for the istropic (top) and anisotropic case (bottom). In the right panel I show the corresponding simulations taking as example $\lambda_{Edd} = 0.13$.

emission to emerge anisotropically (e.g Netzer, 1987b). The radiation hydrodynamical simulations we have presented in chapter 2 suggest that the anisotropy of the AGN can be equally important as the Eddington ratio in determining the dynamics of the outflow and disk, emphasizing the importance of evaluating the effects of the anisotropy. Recently, Ishibashi (2020) used a static, analytic scheme to link the geometry of nuclear outflows to the anisotropy as determined by the black hole spin. Using my radiation-dynamical simulations, I can investigate the impact of anisotropic AGN radiation on the emergence of dusty winds.

Similarly to what has been done in section 2.9, I modify the AGN acceleration

$$a_{\rm AGN} \rightarrow a_{\rm AGN} f(\theta) \tag{3.22}$$

where $f(\theta)$ is the anisotropy function, defined as

$$f(\theta) = \frac{1 + a\cos\theta + 2a\cos^2\theta}{1 + 2a/3} \tag{3.23}$$

with $a = (\eta_a - 1)/3$, introducing the parameter η_a as the "anisotropy factor", equal to the ratio between the polar flux and the equatorial flux. In the left panel of figure 3.10 I show how the radial profile of the AGN radiation pressure is modified when $\eta_a = 10^2$ for $\rm N_H = 3 \times 10^{23}$ cm^{-2}, while in the right panel I show the corresponding full simulations, i.e. infrared+AGN radiation pressure and gravity, for $\lambda_{\rm Edd} = 0.13$.

The introduction of the anisotropic AGN radiation field produces a change in the outflow opening angle, featuring a wider cone with respect to the isotropic case. This is caused by two effects: first, as the AGN radiation is reduced in the plane of the dusty disk, the sublimation radius moves closer to the AGN and the AGN radiation pressure at this inner radius remains the same. As the dusty disk retains its temperature profile (the inner radius is still equivalent to the sublimation temperature), the IR radiation field also remains the same. Second, when a particle is swept upwards, the AGN radiation pressure starts to increase because of the θ-dependence of the radiation profile, introducing a stronger radial component at the same scaled position as compared to the isotropic case. Therefore, the radial radiation pressure component from the AGN will be stronger than the more vertical component of the infrared radiation pressure, resulting in a wider cone.

The disk configuration is not significantly modified, as the AGN radiation pressure does not penetrate deeply. Therefore, even though the gravitational force at the sublimation radius is larger in the anisotropic than in the isotropic case, the disk dynamics remain similar.

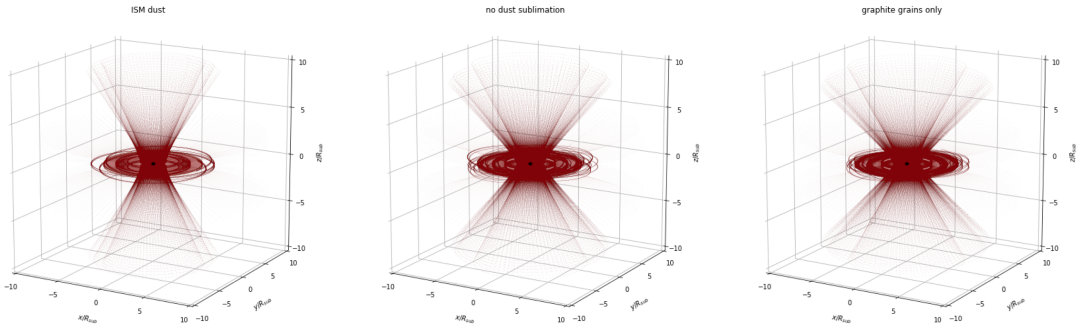

FIGURE 3.11: Simulations for $N_H = 3 \times 10^{23}$ cm^{-2} and $\lambda_{Edd} = 0.13$ for test runs of different dust properties.

3.4.4 Effect of different dust properties

The infrared emission, and hence the infrared radiation pressure strength, is determined by the physical properties of the dust. Throughout this work, I adopted the standard interstellar medium (ISM) dust grain model as set in CLOUDY. It consists of graphites and silicates with sizes following the MRN distribution (Mathis et al., 1977). The grain model also accounts for dust sublimation. In the following, I will examine how my assumptions on the dust composition influence the properties of the dusty wind. For that, I set $N_H = 3 \times 10^{23}$ cm^{-2} and $\lambda_{Edd} = 0.13$.

As a first test, I perform a simulation where I turn off the dust sublimation. In this "no sublimation" run, I allow dust to overheat and exist beyond its critical sublimation temperature. In figure 3.11, I compare the standard ISM simulation (left) with the case of no dust sublimation (middle panel). As dust can heat to higher temperatures as before, the emitted infrared flux (and hence the infrared radiation pressure) will dramatically increase, since $p_{rad} \propto T^{4+\gamma}$ (with γ being the power-law index of the drop of dust absorption efficiency in the near-IR as defined by Barvainis, 1987b). With respect to the "ISM dust" run where dust sublimation is included, the disk appears much thicker as the orbits of particles are puffed up to larger scale heights. At the same time, the wind cone becomes wider as particles at further distance from the sublimation radius are (mostly radially) driven into the wind.

Second, I consider a dust model that accounts for sublimation but includes large graphite grains only. This is motivated by near-infrared observations of nearby AGN that find

high dust emissivities (e.g. Kishimoto et al., 2011b; Gravity Collaboration et al., 2020). Results are shown in figure 3.11 (right panel). Since graphites have on average larger opacities than the corresponding ISM dust composition, this will result in an enhanced infrared radiation pressure in both the disk and wind as more radiation is re-emitted for the same temperature. This causes a stronger radial pressure and a wider cone, similarly to the run without dust sublimation, as the launching region becomes larger in the same manner. The disk is also thicker than the standard ISM case, but the dynamics are less affected than in the "no sublimation" case.

3.5 Discussion

3.5.1 Comparison to radiation-regulated obscuration models of AGN

A recent X-ray study of a large sample of local AGN found that the obscuration covering factor strongly depends on the Eddington ratio (Ricci et al., 2017). They conclude that radiation pressure on dusty gas is the main mechanism driving the distribution of the circumnuclear material, favouring a unifying radiation-regulated obscuration model (see also Hönig, 2019). In particular, a constant Compton thick obscuration ($N_{\rm H} > 10^{24}\ cm^{-2}$) is found with a small covering factor and a Compton thin obscuration varying with the Eddington ratio. The latter has a large covering factor when $\lambda_{\rm Edd} < 10^{-1.5}$ and then drops at larger $\lambda_{\rm Edd}$, with most of the material found in the form of an outflow.

In the framework of Seyfert-like Eddington ratios, the elements emerging from my simulations strongly favours the obscuration structure proposed by Ricci et al. (2017) and can be examined using figure 3.9 as a reference.

My choice to have a velocity profile dependent on radiation affects low column density material the most. Indeed, it is not possible to have bound orbits within the disk for $r \lesssim 5\ r_{\rm sub}$ when $N_{\rm H} \simeq 10^{22}\ {\rm cm}^{-2}$ since those particles are strongly subjected to the AGN radiation pressure and the square-root term in Eq. (3.20) would become negative. In such a strong AGN radiation field, particles are likely to be driven radially outward

and so giving a larger covering factor of low column density material as observed in Ricci et al. (2017).

At moderate column density $N_{\rm H} \simeq 10^{23}$ cm^{-2} the infrared radiation pressure becomes effective and polar outflows start to emerge. At the same time, higher column density material experiences a stronger gravitational pull, which keeps material bound within the disk, rotating according to the previously discussed sub-Keplerian profile.

At larger $N_{\rm H}$, the uplift is effectively suppressed in cases where the Eddington is in the Seyfert regime or below. Matter with $N_{\rm H} \simeq 10^{24}$ cm^{-2} will generally settle in the disk plane, forming a low covering factor of very Compton thick material, as observed by Ricci et al. (2017).

The idea that radiation pressure regulates the AGN obscuration properties has been further investigated (Ricci et al., 2017) by analysing how the observational data populate the "$N_{\rm H}$-$\lambda_{\rm Edd}$" plane, defined by the column density versus the Eddington ratio (e.g Fabian et al., 2008). AGN seem to avoid a wedge-like region starting at $\lambda_{\rm Edd} \sim 10^{-1.5}$ and $N_{\rm H} \sim 10^{22}$ cm^{-2}. Ishibashi et al. (2018) used an analytic model of AGN and infrared radiation pressure based on a spherical wind (and an approximation for the effect on clouds) and found that the forbidden region is dominated by strong radiation pressure, probably clearing out the material from around the AGN. I can test these analytic results with my dynamical model. Indeed, as shown in the previous sections, the parameter range of the "forbidden region" agrees with the parameters for which I found infrared-induced outflows to emerge.

3.5.2 Comparison to observations and models of Circinus

The idea that radiative feedback is driving the obscuration in AGN also affects the emitting dusty outflow structure, not just the obscuration properties. The clear detection of polar emission in Circinus (Tristram et al., 2014) and other sources served as key motivation for the presented study. The latest radiative transfer model of the high angular resolution data of Ciricinus is based on a compact dusty disc with a dusty, hyperbolic cone (Stalevski et al., 2017, 2019).

I tested the hyperboloid wind scenario of Circinus using the $\lambda_{\rm Edd}$ and $N_{\rm H}$ inferred in Stalevski et al. (2019). The authors assume a line-of-sight column density of $N_{\rm H} \gtrsim 10^{24}$ cm^{-2}. I consider single clumps with $N_{\rm H} = 5 \times 10^{23}$ cm^{-2}, with a number of clouds along the equatorial plane being $N_0 = 7$. This provides a value consistent with the one estimated in Stalevski et al. (2019). The Eddington ratio reported is $\lambda_{\rm Edd} = 0.2$. Based on the arguments given in section 3.2.7, my simulation will specifically consider $\lambda_{\rm Edd} = 0.22$ as this illustrates the domain where the infrared radiation pressure dominates for clouds with $N_{\rm H} = 5 \times 10^{23}$ cm^{-2}.

Results of my simulations are shown in figure 3.12 with different inclination with respect to the disk plane. Overall, the structure achieved agrees well with the disk + hyperboloid polar wind scenario as depicted in Stalevski et al. (2019). The half opening angle I found is 26° and the disk flaring angle is $\simeq 4°$, both consistent with observations. The outer wall of the hyperboloid wind $r_{\rm out}^{hyp}$ is located in my simulations at 1.27 $r_{\rm sub}$ which corresponds to 0.05 pc.[1] The latter is roughly 10 times lower than the value found in Stalevski et al. (2017). I argue that the wind boundary I found can be pushed further away to at least 0.2 pc as I do observe an unstable wind region up to 5 $r_{\rm sub}$, where the trajectories receive a significant puff up from radiation pressure or escape outward. This argument links back to the temperature profile assumed for the disk (sec. 3.3). The distance 5 $r_{\rm sub}$ corresponds to a typical temperature $\simeq 700$ K which, as per Wien law, corresponds in turns to an emission peaking at 5 μm. This traces exactly a key observational features in AGN, namely the 3-5 μm bump. Beyond 5-7 $r_{\rm sub}$ the temperature drops, which causes the infrared radiation pressure to drop as a consequence so that any uplift is suppressed.

Finally, Circinus is well known for its maser disk emission seen at $\sim 0.1 - 0.4$ pc (Greenhill et al., 2003) with the disk rotation marginally sub-Keplerian. The observationally derived velocity exponent is roughly $\beta \sim 0.45$. Interestingly, the distance at which these masers are found corresponds approximately to the region where I start to find bound orbits, i.e. 5 $r_{\rm sub}$, which can be considered a first consistency with observations. The

[1] Knowing that the inferred luminosity for Circinus is $L_{\rm Circ} = 3.9 \times 10^{43}$ erg s^{-1} (Tristram et al., 2014) I can estimate the sublimation radius for Circinus to be 0.04 pc.

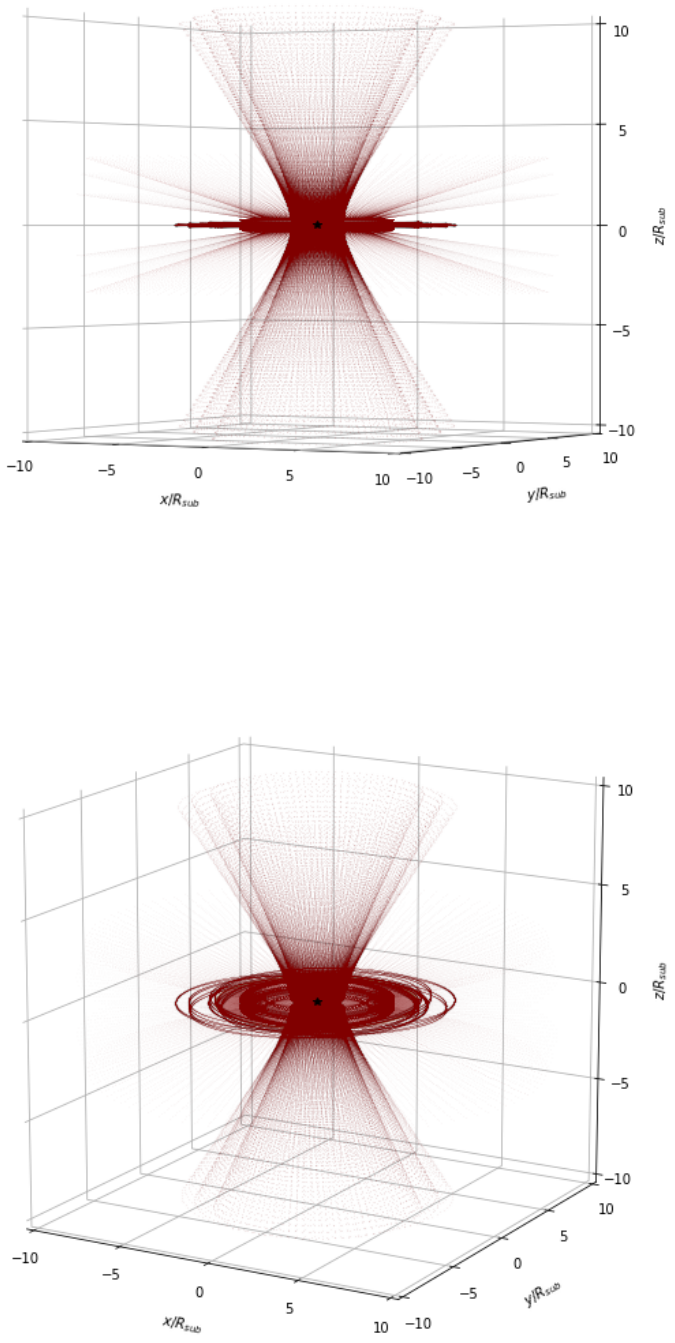

FIGURE 3.12: Three-dimensional views of the proposed configuration for the Circinus-like structure, for the edge-on case (*Top*) and an inclination above the disk plane of 15° (*Bottom*). I used $\lambda_{\rm Edd} = 0.22$ and a column density of $\rm N_H = 5 \times 10^{23}$ cm^{-2}.

value for the velocity exponent β I find at 5 $r_{\rm sub}$ radius is $\beta \sim 0.33$ and gradually approaches the Keplerian value at larger distances, producing approximately the observed mean velocity for the distances where most of the masers are located. These findings

suggest that radiation pressure may affect the dynamics of the maser disks, which might explain the observed sub-keplerian rotation velocities.

3.5.3 Relation to outflows emerging from dust-free regions

The presented dusty wind configuration might also create a link to the structure of outflows observed in AGN at much smaller, dust-free, scales.

Interestingly, a very similar Circinus-like geometry of a funnel-shaped wind has been derived empirically by Elvis (2000) to explain the structure of outflows inside the sublimation radius. Additionally, it has been noted that the structure is subjected to luminosity-dependent changes, reducing the cylindrical part of the outflow or modifying its half opening angle. As suggested in Hönig (2019), both the high opacity and mass content of the dust characterising the outflow at parsec-scales are likely to define the boundary of the material closer to the accretion disk.

If this is the case, the wind geometry reproduced by my simulations might as well provide insights into the observed outflows emerging from dusty free regions, making them dependent on the Eddington ratio, rather than the luminosity.

3.6 Summary and conclusions

I have presented the results of 3D numerical simulations of dusty gas clouds moving around an AGN and considering the infrared re-radiation of the hot dust itself. The aim of this work is to offer insights on the obscuration properties of AGN, with particular reference to the emergence of radiatively driven dusty winds. I first proposed a semi-analytical model based on a dense clumpy disk circumnuclear to a central AGN. Then I consider the radiation pressure from the AGN in the optical/UV, gravity from the central black hole and the radiation pressure in the infrared coming from the dusty disk. From my investigation, I have found several results:

- Infrared radiation pressure from a hot disk is sufficient to produce a polar wind in the hot inner regions of AGN and an overall puff-up along the entire disk surface.

- The IR radiation pressure is most effective at launching a wind around a critical limit where the AGN radiation pressure approximately balances gravity from the central black hole, so that the IR pressure from the disk is the dominant component of the effective force.

- Radiation-dynamical simulations show that it is possible to have a stable rotating structure if initial sub-Keplerian velocities are assumed. Those sub-Keplerian disk velocities are a consequence of both optical and infrared radiation pressure.

- My model favors radiation-regulated obscuration scenarios: the amount of material observed and the covering factor are shaped by the combination of the Eddington ratio and column density of dusty clouds in the AGN vicinity.

- I have been able to qualitatively reproduce high-angular infrared observations and radiative transfer modeling of the AGN in the Circinus Galaxy. Specifically, I replicate the hyperboloid shape of the wind proposed by Stalevski et al. (2019).

- I discussed the impact of anisotropic radiation field. This mainly affects the outflow configuration, resulting in a wider cone, while the disk remains unchanged.

- The dust model assumed is a fundamental factor to determine the disk and wind configuration, as this affects the local infrared radiation field strength.

The model presented here has deliberately been kept simple in order to highlight the role of infrared radiation pressure in shaping the AGN environment. An account of fragmentation processes of optically thick clouds under radiation pressure is a separate issue which is beyond the scope of this work. It is likely that dust clumps with the physical properties adopted in this work can survive in the strong radiation field of an AGN, as implied by Namekata et al. (2014). Hence, the basic characteristics of the resulting outflow should not significantly change by more elaborate considerations.

Chapter 4

Unifying UV and IR outflows

"We build too many walls, and not enough bridges"

Isaac Newton

4.1 Overview and context

AGN activity is believed to be accompanied by outflows in a variety of forms and in a widespread range of distances. The discovery of dusty winds at parsec scales is only one example of the various outflow manifestations. Outflows are considered the major agents in the feedback processes that regulate the observed co-evolution of the SMBHs and their environment, connecting the small scales of the central black hole to the large scales of the host galaxy. The AGN outflows can in fact have a strong impact on the AGN host galaxy, as they drive gas out of the galaxies and significantly affect star formation, chemical enrichment of the intergalactic medium, and cooling flows in galaxy clusters (e.g. review by Fabian, 2012). One possible outcome of these feedback mechanisms is the observed correlation between the mass of the SMBH and the velocity dispersion of stars in the galaxy bulge (Magorrian et al., 1998; Ferrarese and Merritt, 2000; Gebhardt et al., 2000; Kormendy and Ho, 2013). Feedback from outflows may also regulate the overall mass and size of the host galaxy (e.g. Silk and Rees, 1998;

King, 2003; Ostriker et al., 2010). Hence, outflows are widely invoked in analytical models and large-scale cosmological simulations to reproduce the observed black hole-host galaxy correlations. Outflows morphology spans from narrowly collimated radio jets to wide-angle winds. These winds are often identified through their broad, blue-shifted absorption features in the X-ray and ultraviolet spectra. According to these observations, AGN-driven outflows have a variety of properties, suggesting that several mechanisms may be involved. Examples include the warm X-ray absorbing gas (known as "warm absorbers"), studied simultaneously with the ultraviolet resonance absorption lines, and ultra-fast outflows (UFO) which are thought to originate in the inner accretion disk and are detected via their broad, highly blue-shifted Fe K features. Recent additions to the list of known AGN wind manifestations are the newly discovered obscuring outflows, which will be the focus of this Chapter. This kind of outflows show strong soft X-ray absorption associated with broad, fast, blue-shifted UV absorption lines. Sources with detected obscuring outflows are NGC 5548 (Kaastra et al., 2014), Mrk 335 (Longinotti et al., 2013), NGC 985 (Ebrero et al., 2016), and most recently, NGC 3783 (Mehdipour et al., 2017; Kriss et al., 2019). In the case of X-ray obscuring outflows, the gas appears to be mildly ionised and has high column density values ($10^{22} - 10^{23}$ cm^{-2}). Continuum absorption by the obscurer is too strong to produce detectable X-ray absorption lines that allow diagnostics of the kinematics or ionisation state of the gas. The crucial element in all cases cited above is the availability of contemporaneous UV spectra. The UV absorption lines that appear in these events provide the necessary diagnostics that show gas outflowing (blue-shifted) with velocities (few thousand km s^{-1}) and ionisation states consistent with an origin in, or interior to the broad-line region (BLR). To gain a better understanding of obscuring outflows, Mehdipour et al. (2017) undertook a monitoring campaign using *Swift* (Gehrels et al., 2004) to find potential X-Ray obscuring events that can then be studied trough simultaneous multiwavelength observations using XMM-Newton (Jansen et al., 2001), NuSTAR (Harrison et al., 2013) and the Hubble Space Telescope (HST). One successful monitored source as part of the program is NGC 3783. They found that the obscuring gas is located in the outer of the broad line region of the AGN. Detailed modeling of the UV and optical spectra has been performed by Kriss et al. (2019). They found blue-shifted UV lines absorption associated with Lyα, N V, Si

IV and C IV.

The goal of this chapter is to test the possible connections of obscuring outflows with dusty winds, using the C IV emission line profile in NGC 3783. As already discussed in section 3.5.3, the similarity between the wind geometries of dusty winds and outflows originating from dust-free regions, suggests that the dusty winds are likely to define the boundary of the outflows closer to the accretion. Then, inevitably the question arises whether or not the obscuring outflows in NGC 3783 trace the skin of its well-known dusty wind. In the following sections I will describe the obscuring outflows observations in NGC 3783, referring to the work of Mehdipour et al. (2017) and Kriss et al. (2019). I will then focus on the C IV emission line profile and construct a photoionisation model to reproduce the absorption observed. Results show very significant correlations to the dusty winds in NGC 3783, giving support to the suggestion of a global, stratified wind scenario.

4.2 Obscuring outflows observation in NGC 3783

Obscuring winds can be detected with Swift by studying the X-ray spectral hardness ratio, and subsequent joint observations with XMM-Newton, NuSTAR, and HST. The hardness ratio (HR) is defined as $(H-S)/(H+S)$, where H and S are the $Swift$'s X-Ray Telescope (XRT) counts in the hard (1.5-10 KeV) and soft (0.3-1.5 KeV) bands, respectively. X-ray absorption by obscuring events increases HR. While most AGN show stable HR throughout the year, NGC 3783 showed significant X-ray spectral hardening in 2016 lasting 32 days (see figure 4.1). During this period, multiwalenghts observations with $XMM-Newton$, $NuSTAR$ and HST have been executed by a large team of astronomers, including the authors in Mehdipour et al. (2017).

Figure 4.2 compares the unobscured and obscured spectrum of NGC 3783. Heavy X-ray absorption is evident in the 2016 data, with the 0.3−2 KeV flux dropping by a factor of 8.0 (11 Dec 2016) and 4.5 (21 Dec 2016). This X-ray absorption coincides with an increase in the UV flux (see figure 4.1, upper panel). This interplay between the two phenomena has been observed also in Mrk 335 (Longinotti et al., 2013) and NGC 985 (Ebrero et al., 2016) and has been interpreted as produced by a disk wind (Ebrero et al.,

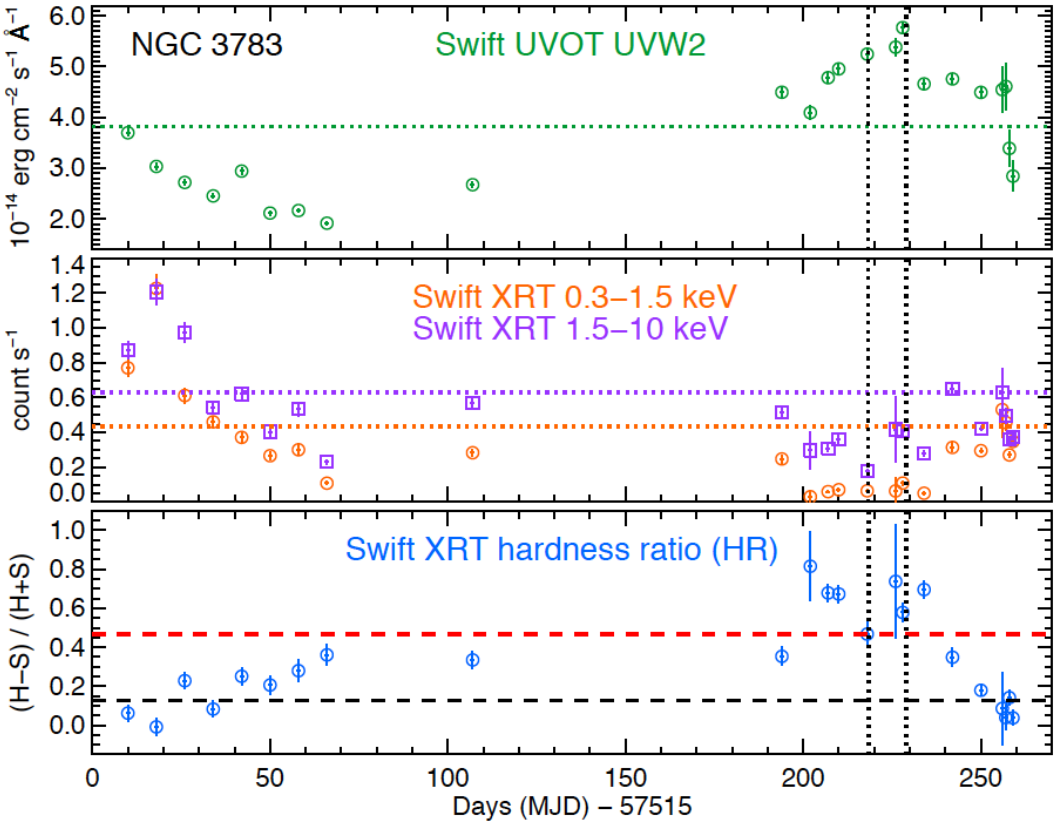

FIGURE 4.1: *Swift* lifhtcurve of NGC 3783 from 17 May 2016 to 21 January 2017. The horizonatal dotted lines in the two upper panels show the all-time average *Swift* flux levels. The dashed black line in the bottom panel indicates the average quiescent hardness ratio (HR) for unobscured data. The dashed red line is HR limit for triggering obscurations event. Figure taken from Mehdipour et al. (2017).

2016). As can be seen in figure 4.3, strong line absorption affects the blue side of the C IV line, with a maximum depth at -3000 km $^{-1}$ and highest velocities at -6200 km s^{-1}, which suggests that the obscuring wind has origin in or near the BLR. From the analysis from Mehdipour et al. (2017), the obscurer in NGC 3783 partially covers the central source with a column density on the order of 10^{23} cm^{-2} and is outflowing with a range of velocities up to 6000 km s^{-1}. The obscuration is produced by an inhomogeneous and clumpy medium, and, as inferred in their paper, it is probably a disk wind at the outer broad-line region of the AGN.

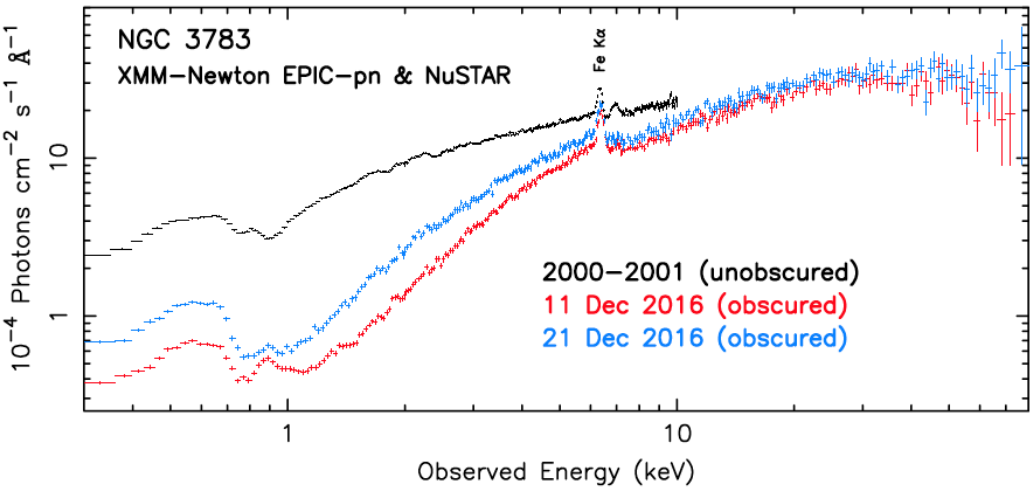

FIGURE 4.2: Figure taken from Mehdipour et al. (2017). NGC 3783 spectra from broad-band x-Ray instruments (EPIC-pn - the European Photon Imaging Camera-pn) on XMM-*Newton* and *Nu*STAR.

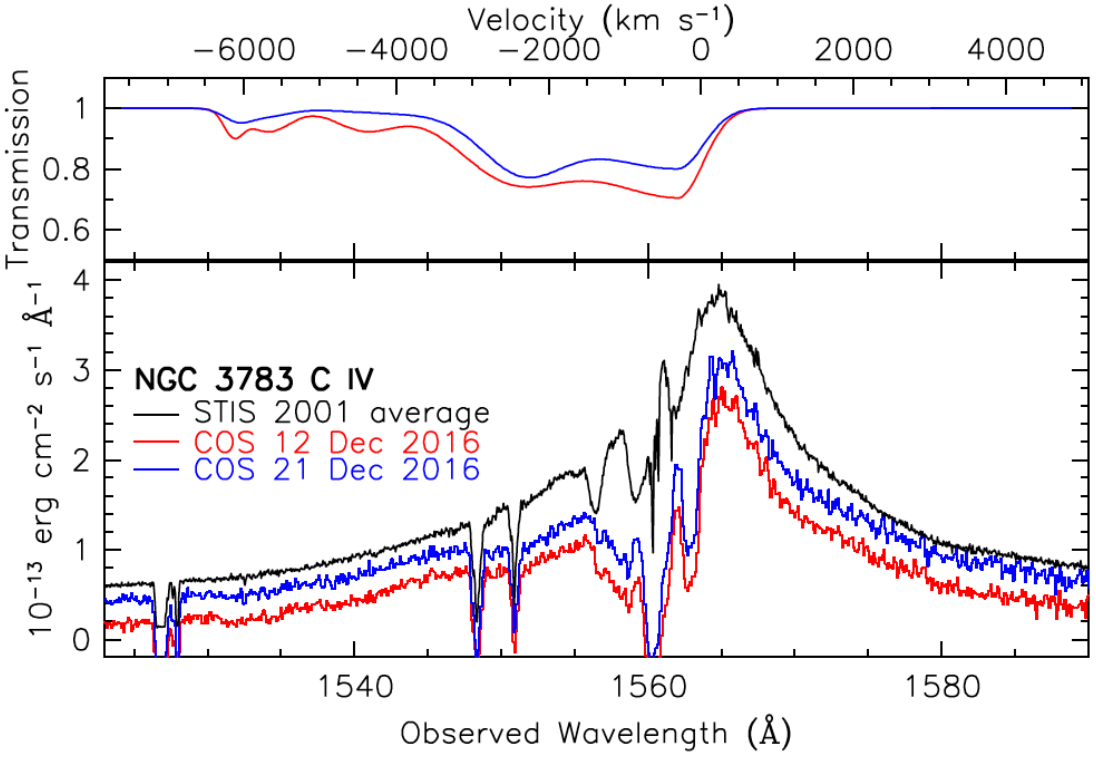

FIGURE 4.3: Figure taken from Mehdipour et al. (2017). NGC 3783 HST COS and STIS spectra near the C IV line. The line transmission model for the new broad C IV absorption component in 2016 is shown in the top panel. The displayed spectra are continuum subtracted and then offset vertically by 2.5×10^{-14} erg cm^{-2} s^{-1} Å^{-1} for each epoch so that the weaker changes in the absorption are more visible.

4.3 Connection to dusty outflows

As we have seen, the spectra of the C IV line is characterised by a wide range of velocities. The part that caught my attention and motivated this work is the lowest end of the range, where $v \sim 10^{-2}$ km s^{-1}, as velocity of a few hundreds km s^{-1} typically observed in dusty winds. In this section I am going to model the intrinsic properties of the UV obscurer using the unobscured C IV line. I then analyse the depth of the absorption features and generate a series of CLOUDY photoionisation models to derive the corresponding column density values.

4.3.1 Modeling the unobscured C IV profile

To model the emission line of C IV in the unobscured state, I use the data extracted by Kriss et al. (2019) who fitted in detail the C IV profile. The best fit consists of 4 Gaussians: a narrow component with FWHM $\sim$ 900 km s^{-1}, a medium-broad component (FWHM $\sim$ 2500 km s^{-1}), a broad component (FWHM $\sim$ 4500 km s^{-1}) and a very broad component (FWHM $\sim$ 10 000 km s^{-1}). Apart from the very broad emission contribution which is represented by one single component, any additional Gaussian is in turn decomposed into a blue and red component, giving a total of 7 Gaussians. It worth noting that the single components do not necessarily correspond to distinct portion of the line-emitting region and are only included to fit the unobscured C IV line profile. I report for convenience in table 4.1 the best fit emission-line parameters given in Kriss et al. (2019) which I will be using to reconstruct and analyse the fiducial C IV line profile in the absence of the absorbing material. These properties are the vacuum rest wavelength of the spectral feature λ_0 (in Å), the integrated flux F_0 in units of 10^{-14} erg cm^{-2} s^{-1}, the systematic velocity v_{sys} (in km s^{-1}) relative to a redshift of $z = 0.00973$ (a value determined in Theureau et al. (1998)), the full-width at half-maximum (km s^{-1}). The total flux can be expressed as

$$F = \sum A_i e^{-\frac{(\lambda - \lambda_{obs,\,i})^2}{2\sigma_i^2}} \tag{4.1}$$

TABLE 4.1: Emission line parameters extracted by Kriss et al. (2019) to model the unobscured C IV line profile.

	λ_0	F_0	v_{sys}	FWHM
C IV blue	1548.19	40	-60	940
C IV red	1550.77	40	-60	940
C IV blue	1548.19	80	140	2840
C IV red	1550.77	80	140	2840
C IV blue	1548.19	84	-950	4580
C IV red	1550.77	84	-950	4580
C IV	1549.48	310	60	10030

with

$$\lambda_{obs,\,i} = \frac{\lambda_0}{v_{sys,i}/c + 1}, \qquad \sigma_i = FWHM \frac{\lambda_{obs,\,i}}{c\ 2\ \sqrt{2 \ln 2}}, \qquad A_i = \frac{F_{0,\,i}}{\sigma_i \sqrt{2\pi}}. \tag{4.2}$$

Figure 4.4 shows the resulting profile, as well as the Gaussian components.

4.3.2 Modeling the properties of the absorbing material

To analyse the properties of the absorbing material, I manually measure the depth and width of the absorption features as they appear in the unobscured line profile of C IV. I take figure 4.3 as a reference and model the 5 most prominent absorption lines. In the following, I will be using the superscript $*$ to denote the quantities that have been measured "by hand" from the image. These quantities are the full-width at half-maximum FWHM*, the flux of the continuum, the flux of the minimum value of the feature, the velocity shift $v^*_{\rm shift}$ and the observed wavelength of the absorption feature λ^*_{obs}. These are first in pixels from the image and then converted to flux units using the binning in the image. I model the shape of the absorption line as a normal function of the type

$$f(\lambda) = F_{abs}\ e^{-\frac{1}{2}\frac{(\lambda-\lambda^*_0)^2}{\sigma^2}} \tag{4.3}$$

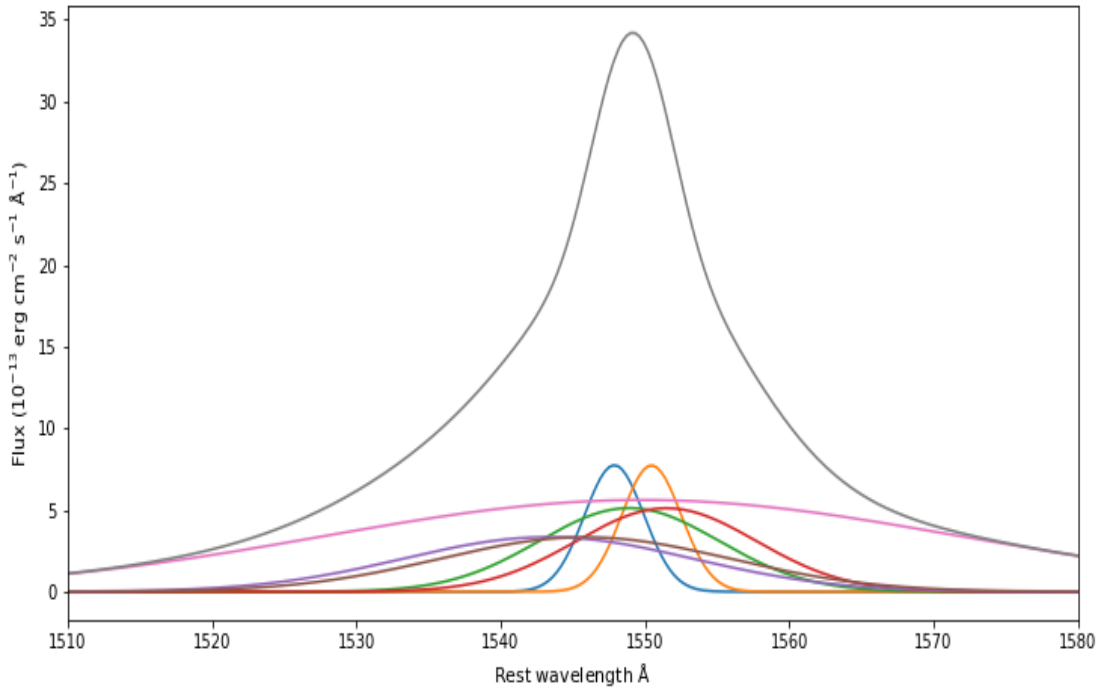

FIGURE 4.4: Reconstruction from a Gaussian decomposition of the fiducial C IV using the data from Kriss et al. (2019).

where F_{abs} is the depth of the line. σ^* is related to the FWHM by

$$\sigma^* = FWHM^*/2.35 \tag{4.4}$$

I then fix the line centers at their rest wavelength value with

$$\lambda_0^* = \frac{\lambda_{obs}^*}{\mathrm{v}_{\mathrm{shift}}^*/c + 1} \tag{4.5}$$

The amount of flux absorbed F_{abs} can be calculated as $F_{abs} = (F_{abs}^*/F_0^*)\ F_0$, where F_0 denotes here the flux of the continuum at the specific wavelength of the absorption feature. Figure 4.5 shows the resulting line model that will be using in the following section.

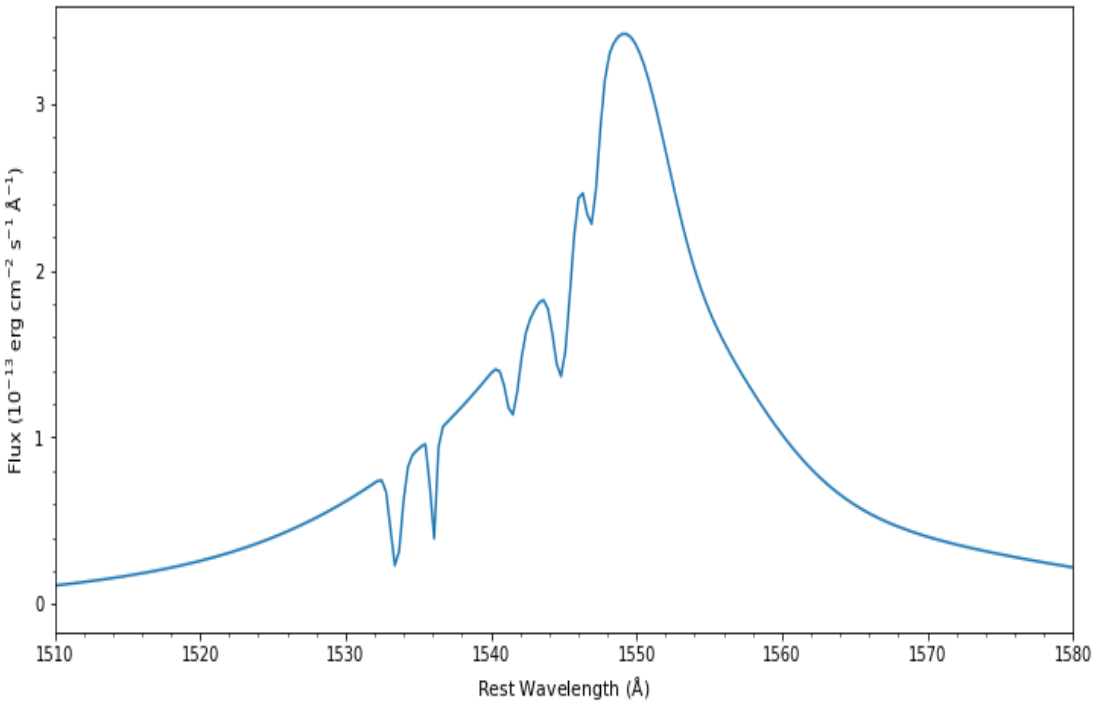

FIGURE 4.5: Emission line model reproducing the shape of the C IV profile.

4.3.3 Cloudy model of the absorbing medium

The ratio of the flux absorbed to the continuum allows extracting the optical depth of the line as

$$\tau = -\ln(F_{abs}/F_0). \tag{4.6}$$

Knowing the optical depth of the material causing the absorption allows in turn to set up a CLOUDY model and derive the corresponding column density. I denote by A_i each of the absorbing features and show in figure 4.6 the corresponding optical depth and velocities. Note that, as per equation (4.6), when the ratio of the flux absorbed to the continuum $\ll 1$, τ increases. By contrast, when $F_{abs}/F_0 \to 1$, then τ becomes smaller. In formulas,

$$F_{abs}/F_0 \ll 1 \quad : \quad \tau \to \infty \tag{4.7}$$

$$F_{abs}/F_0 \to 1 \quad : \quad \tau \to 0 \tag{4.8}$$

This explains why, i.e., $\tau_{A_5} \gg \tau_{A_1}$. Next, I construct several CLOUDY photoionisation models with the following assumptions. First, I adopt the same custom AGN SED used

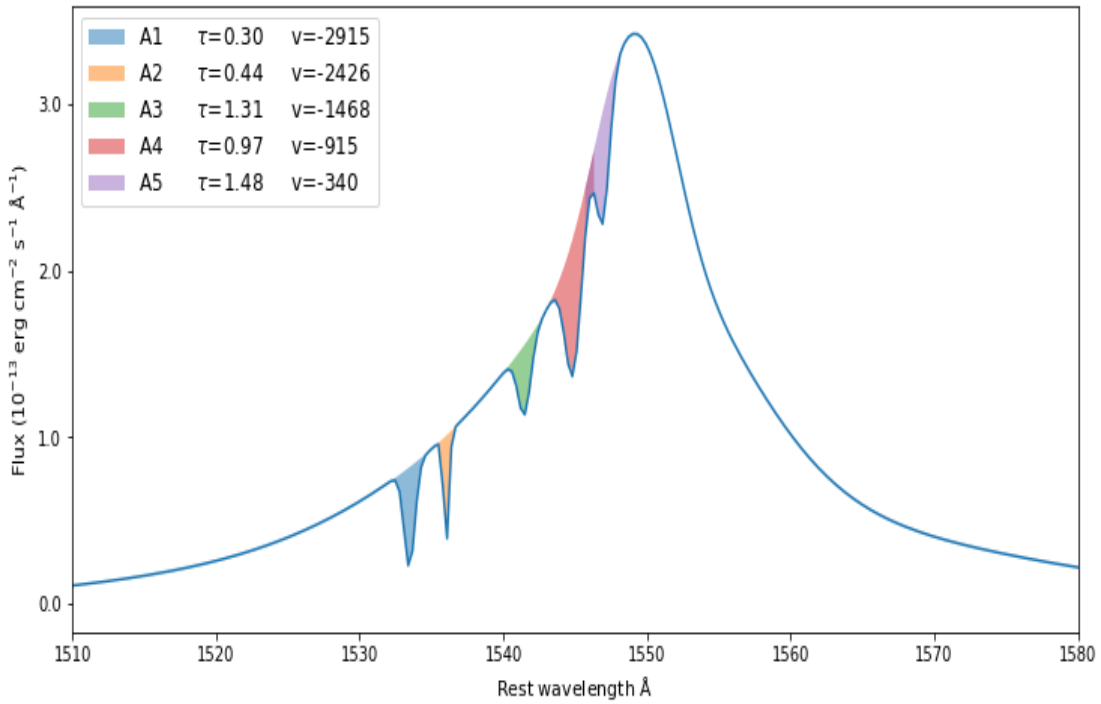

FIGURE 4.6: Naming scheme adopted to model the absorbing features in the C IV line profile and corresponding velocity and optical depth.

as base of the CLOUDY calculations of the RHD model presented in Chapter 2 (see section 2.4.1.2). Then, I assume that the obscurer originates near or interior to the BLR and spatially extends into the "torus region". Therefore, I arbitrary choose as inner radius 0.2 r_{sub} and outer radius 20 r_{sub} and turn on the sublimation function. Following Dehghanian et al. (2019), the density at the base of the obscurer is likely to be higher than at larger distances, so I consider a density power-law profile of the type

$$n_H(r) = n_0 \left(\frac{r}{r_0}\right)^{\alpha}, \tag{4.9}$$

where the initial density is fixed to $n_0 = 10^9$ (as typical in the BLR) and $\alpha = -1$.

Finally, I run 5 CLOUDY simulations for each of the absorbing features and stop the calculation at the corresponding continuum absorption optical depth set by the measured depth. Then, I extracted the column density at the end of the run as shown in table 4.2. The typical column density is found to be $\sim 4 \times 10^{23}$. From the model constructed in Chapter 3, this is typically associated with the emergence of a dusty wind for AGN in the Seyfert regime. This initial consistency encourages further investigation into the

TABLE 4.2: Column density extracted by CLOUDY photoionisation models of the absorbing material.

name	τ	v (km s^{-1})	N$_H$ (cm $^{-2}$)
A1	0.30	-2915	3.64×10^{23}
A2	0.44	-2426	3.76×10^{23}
A3	1.31	-1468	4.33×10^{23}
A4	0.97	-915	4.12×10^{23}
A5	1.48	-340	4.43×10^{23}

idea of a unified wind scenario. Now, considering that the absorption feature A5 is also found having velocities consistent with those observed in dusty winds, I decided to analyse more in detail this feature and use the work presented in Chapter 3 to simulate how dusty particles having this particular column density behaves in NGC 3783.
Figure 4.7 shows the configuration found when N_H =4.43×10^{23} and taking λ_{Edd} = 0.07, as found in NGC 3783 (Summons et al., 2007). The velocities are a combination of rotation and outflows and range from ∼200 to ∼ 500 km s^{-1}. For this particular simulation, the mean velocity value is 339 km s^{-1}, which is surprisingly close to the observed velocity value of the low-velocity UV absorber.

Since CLOUDY predicts the continuum emerging from the material causing the absorption, the last test I wish to perform is to check whether or not the X-ray absorber could be associated with a local infrared emission peak as this is typically observed in dusty winds. Figure 4.8 shows the spectrum for the two low-velocity features with labels denoting several of the various absorption lines. From the figure we can see that the spectrum is characterised by a distinct emission bump. This suggests that, at least qualitatively, the spectral features of these two kinds of outflows also appear to be shared, although further analysis would be necessary to reproduce in detail the infrared bump observed in NGC 3783.

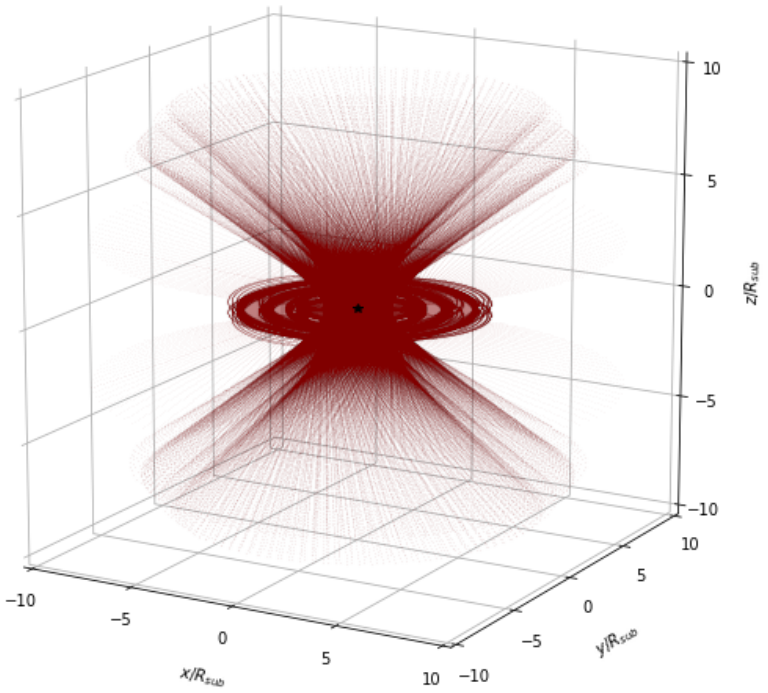

FIGURE 4.7: 3D radiation dynamical simulations for particles having $N_{\rm H} = 4.43 \times 10^{23}$ cm $^{-2}$ and $\lambda_{\rm Edd} = 0.07$.

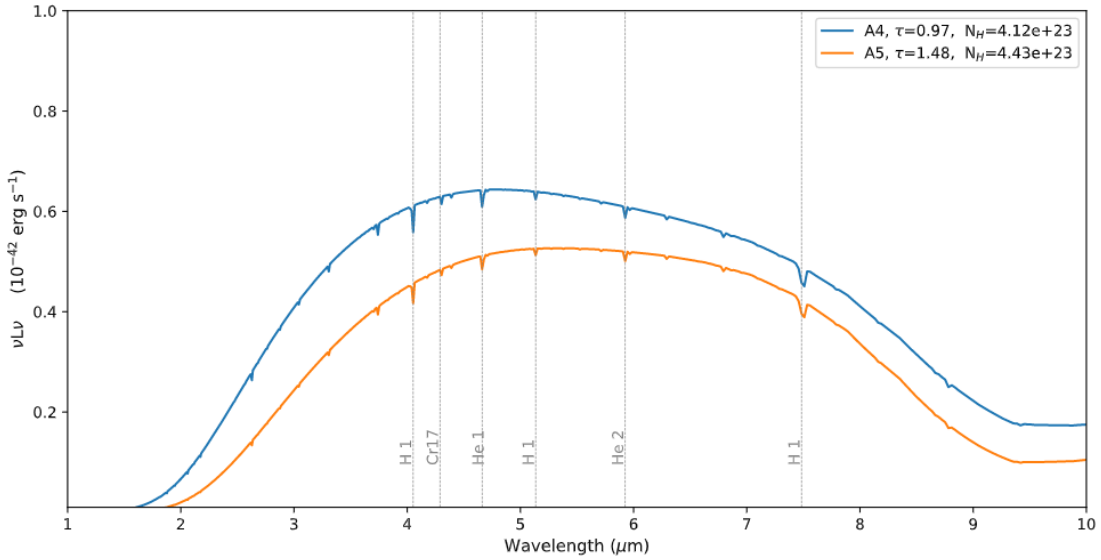

FIGURE 4.8: Infrared spectra for each of the absorbing features in the C IV line profile.

4.4 Summary and conclusions

In this work, I investigate the properties of the UV outflows observed in NGC 3783 and study their potential relationship to dusty winds. These UV outflows produce strong absorption of the X-ray continuum, in addition to the appearance of blue-shifted and broad UV absorption lines that allow diagnostics of the kinematics or ionisation state of the gas. A detailed analysis of the UV spectrum has been performed in Mehdipour et al. (2017) and Kriss et al. (2019). I have used their data as a starting point to explore the possible correlations between these UV and dusty outflows. In particular, I reconstructed the fiducial C IV line profile and measured the depth of the absorption features. These features have a range of velocities, from $\sim$ 350 to $\sim$3000 km s^{-1}. The ones that triggered this work were the low velocities absorption lines. I set up a CLOUDY model for an absorbing material located interior to the BLR and extending up to the dusty winds regions. I stopped the calculation at the observed optical depth and calculated the corresponding column density. In particular, for the absorption features having v = $-$340 km s^{-1} and optical depth $\tau = 1.48$ I found a photoionisation solution with $N_{\rm H} = 4.43{\times}10^{23}$ cm^{-2}. Consistent velocities are found in the 3D radiation dynamical simulation for dusty particles having $N_{\rm H} = 4.43{\times}10^{23}$ cm^{-2} and exposed to the radiation field of an AGN with the accretion state of NGC 3783. In addition, these absorption features might also be associated with an infrared emitting structure, as seen from the qualitative analysis of the infrared spectrum. To summarize, the very significant correlations of this set of parameters, such as ionisation, column density, velocity, distance and spectral properties between dusty winds and the low-velocity part of the UV outflows strongly suggest that these two phenomena could actually represent layers of a single, multiphase structure observed at different locations along the line of sight.

Chapter 5

Summary of the Thesis and Outlook

> "I should have liked to have closed these lectures by leading up to some great climax. But perhaps it is more in accordance with the true conditions of scientific progress that they should fizzle out with a glimpse of the obscurity which marks the frontiers of present knowledge. I do not apologize for the lameness of the conclusion, for it is not a conclusion. I wish I could feel confident that it is even a beginning."
>
> Lectures, Arthur Eddington

The aim of this Thesis was to gain further insights into the physical state and dynamics of the torus, with particular reference to the role and origin of dusty winds. I addressed this problem from several points of views.

In chapter 2 a new 3-dimensional radiation hydrodynamics model has been presented

to explore the role of radiatively-driven winds. The model consists of a dusty disk fully exposed to the AGN radiation pressure and neglect the re-radiation of IR photons from dust. The dynamical evolution has been presented first in the small scales regime ($\sim$ 1 pc), where the wind is produced, then in a larger scales model ($\sim$ 1-100 pc) where results can be compared to observations. The RHD simulations are based on a Lagrangian formulation of hydrodynamics, able to provide a unique angle of view with respect to previous simulations of AGN dusty tori and particularly efficient in capturing the production and evolution of the wind. I used the photoionisation code CLOUDY to generate a very large number of cloud models, spanning over a wide range of volumetric density of the cloud, the incident AGN radiation field and the temperature of the gas. This grid of models has been stored in form of lookup tables, so that the relevant properties can be easily accessed during the simulations. This has involved working out the best solution when the physical quantity requested by the RHD simulations is not directly printed out by CLOUDY or the regime explored is too extreme to produce converging solutions. The physical quantities which have been tabulated are the heating and cooling rate, the temperature of the dust, the dust to gas mass ratio, the radiative acceleration due to the continuum, the flux-weighted opacities and optical depth, emissivities for two CO lines, two HCN lines and three vibrational transitions of H_2.

Having the CLOUDY tables as its foundation, the RHD model produced a number of interesting results. In particular, the small scale model revealed a two-components structure, a cool rotating disk and a hot wind, although the outflow is radial rather than polar, likely due to the lack of radiation pressure from hot dust. An important finding of this first model is that the anisotropy of the radiation field is as important as the Eddington ratio in governing the dynamics of the disk and outflow. Finally, supernovae do not appear to be efficient at launching material high above the disk, emphasizing again the importance of the infrared radiation to reproduce the obscuration properties observed in AGN.

The large scale model uses additional sub-grid physics to inject the wind, as its production is now unresolved. Results from the large scales 3D RHD simulations agree with the ubiquity of polar extended mid-IR emission, and the general hollow-cone wind geometry predicted by radiative transfer models, although the wind has a parabolic

structure, rather than the hyperbolic configuration predicted by observations, and this again might be due to the lack of the IR radiation pressure. Finally, the velocity maps of the large scale RHD model can reproduce many features of observations, including apparent "counter-rotation".

The chapter concluded by demonstrating how the CLOUDY tables I constructed can be used to determine the dominant coolants emerging in the dusty regions of AGN. In particular, it has been possible to predict the coolants emerging in the wind fall-back region, whose physical properties are still unconstrained.

In a future work, the RHD can be improved by implementing a form of infrared radiation pressure, whose importance has been emphasized in both the small and large scale model. This can involve producing an algorithm that repetitively reads as input the radiation field predicted from a previous CLOUDY calculation to form a much larger table. However, the high number of possible interactions between particles makes this type of calculation extremely complex to implement. One solution might be to limit this approach only to the regions where the infrared radiation has major contributions, such as close to the sublimation radius.

In chapter 3 the role of the infrared radiation pressure in launching and shaping dusty winds in AGN has been studied through a semi-analytical model and 3D simulations. The model consists of an AGN and an infrared radiating dusty disk, the latter being the primary mass reservoir for the outflow. I calculate the trajectories of dusty gas clumps in this environment, accounting for both gravity and the AGN radiation as well as the re-radiation by the hot dusty gas clouds themselves. It is shown that infrared radiation pressure from the disk is sufficient to produce a polar wind and an overall puff-up along the entire disk surface. The IR radiation is most effective at launching a wind around the critical limit where the AGN radiation pressure approximately balances the gravity from the central black hole. The morphology in this case consists of a disk of material that orbits with sub-Keplerian velocities and a hyperboloid polar wind launched at the inner edge of the dusty disk, and I have been able to replicate the structure observed in the local Circinus galaxy (Stalevski et al., 2019). The strength of the wind and its orientation depend on the Eddington ratio and the column density of the dusty clumps,

which is in agreement with proposed radiation regulated obscuration models developed for the X-ray obscuring material around AGN.
In future work, this model can be tailored to the needs of the RHD model to understand which regions have a major contribution from the IR radiation pressure and which behaviour to expect, so that the computational cost of the inclusion of this secondary source of radiation can be significantly reduced.

In Chapter 4 I examine the possibility of a unifying scenario that connects dusty winds and UV outflows observed in NGC 3783. These UV outflows produce strong X-ray absorption associated with broad, fast, blue-shifted UV absorption lines. Using the data from Mehdipour et al. (2017) and Kriss et al. (2019), I analysed the properties of the C IV emission line profile and construct a CLOUDY photoionisation model to reproduce the absorption observed. Using the 3D dynamical model derived in chapter 3, my analysis finds significant correlations between the properties of dusty winds and the low-velocity part of the UV absorption lines. In particular, I found that the ionisation, column density, velocity, distance and spectral properties are consistent with the suggestion of a unified wind scenario. These pieces of evidence give motivation to further investigate the idea of a single, stratified outflow, which is left for future work. In particular, the next step could be to reproduce in detail the infrared bump observed in NGC 3783 with a grid of CLOUDY models, to better constrain the properties of the absorber and its relationship with dusty winds.

Bibliography

A. Alonso-Herrero, S. García-Burillo, M. Pereira-Santaella, R. I. Davies, F. Combes, M. Vestergaard, S. I. Raimundo, A. Bunker, T. Díaz-Santos, P. Gandhi, I. García-Bernete, E. K. S. Hicks, S. F. Hönig, L. K. Hunt, M. Imanishi, T. Izumi, N. A. Levenson, W. Maciejewski, C. Packham, C. Ramos Almeida, C. Ricci, D. Rigopoulou, P. F. Roche, D. Rosario, M. Schartmann, A. Usero, and M. J. Ward. Nuclear molecular outflow in the Seyfert galaxy NGC 3227. , 628:A65, August 2019.

A. Alonso-Herrero, M. Pereira-Santaella, S. García-Burillo, R. I. Davies, F. Combes, D. Asmus, A. Bunker, T. Díaz-Santos, P. Gandhi, O. González-Martín, A. Hernán-Caballero, E. Hicks, S. Hönig, A. Labiano, N. A. Levenson, C. Packham, C. Ramos Almeida, C. Ricci, D. Rigopoulou, D. Rosario, E. Sani, and M. J. Ward. Resolving the Nuclear Obscuring Disk in the Compton-thick Seyfert Galaxy NGC 5643 with ALMA. , 859(2):144, June 2018.

R. Antonucci. Unified models for active galactic nuclei and quasars. , 31:473–521, 1993.

R. R. J. Antonucci and J. S. Miller. Spectropolarimetry and the nature of NGC 1068. , 297:621–632, October 1985.

D. Asmus. New evidence for the ubiquity of prominent polar dust emission in AGN on tens of parsec scales. , 489(2):2177–2188, October 2019.

D. Asmus, S. F. Hönig, and P. Gandhi. The Subarcsecond Mid-infrared View of Local Active Galactic Nuclei. III. Polar Dust Emission. , 822:109, May 2016.

Anelise Audibert, Françoise Combes, Santiago García-Burillo, and Philippe Salomé. Probing the gas fuelling and outflows in nearby AGN with ALMA. *Frontiers in Astronomy and Space Sciences*, 4:58, December 2017.

Eduardo Bañados, Bram P. Venemans, Chiara Mazzucchelli, Emanuele P. Farina, Fabian Walter, Feige Wang, Roberto Decarli, Daniel Stern, Xiaohui Fan, Frederick B. Davies, Joseph F. Hennawi, Robert A. Simcoe, Monica L. Turner, Hans-Walter Rix, Jinyi Yang, Daniel D. Kelson, Gwen C. Rudie, and Jan Martin Winters. An 800-million-solar-mass black hole in a significantly neutral Universe at a redshift of 7.5. , 553 (7689):473–476, January 2018.

Josh Barnes and Piet Hut. A hierarchical O(N log N) force-calculation algorithm. , 324 (6096):446–449, December 1986.

Richard Barvainis. Hot Dust and the Near-Infrared Bump in the Continuum Spectra of Quasars and Active Galactic Nuclei. , 320:537, September 1987a.

Richard Barvainis. Hot Dust and the Near-Infrared Bump in the Continuum Spectra of Quasars and Active Galactic Nuclei. , 320:537, September 1987b.

Matthew R. Bate and Andreas Burkert. Resolution requirements for smoothed particle hydrodynamics calculations with self-gravity. , 288(4):1060–1072, July 1997.

Misty C. Bentz, Jonelle L. Walsh, Aaron J. Barth, Nairn Baliber, Vardha Nicola Bennert, Gabriela Canalizo, Alexei V. Filippenko, Mohan Ganeshalingam, Elinor L. Gates, Jenny E. Greene, Marton G. Hidas, Kyle D. Hiner, Nicholas Lee, Weidong Li, Matthew A. Malkan, Takeo Minezaki, Yu Sakata, Frank J. D. Serduke, Jeffrey M. Silverman, Thea N. Steele, Daniel Stern, Rachel A. Street, Carol E. Thornton, Tommaso Treu, Xiaofeng Wang, Jong-Hak Woo, and Yuzuru Yoshii. The Lick AGN Monitoring Project: Broad-line Region Radii and Black Hole Masses from Reverberation Mapping of Hβ. , 705(1):199–217, November 2009.

H. Boehringer, W. Voges, A. C. Fabian, A. C. Edge, and D. M. Neumann. A ROSAT HRI study of the interaction of the X-ray emitting gas and radio lobes of NGC 1275. , 264:L25–L28, October 1993.

Davide Burlon, Marco Ajello, Jochen Greiner, Andrea Comastri, Andrea Merloni, and Neil Gehrels. Three-year Swift/BAT Survey of AGN: Reconciling Theory and Observations? In Jan-Uwe Ness and Matthias Ehle, editors, *The X-ray Universe 2011*, page 045, August 2011.

A. Capetti. Revisiting the census of low-luminosity AGN. , 535:A28, November 2011.

C.-H. Chan and J. H. Krolik. Radiation-driven Outflows from and Radiative Support in Dusty Tori of Active Galactic Nuclei. , 825:67, July 2016.

C.-H. Chan and J. H. Krolik. Geometrically Thick Obscuration by Radiation-driven Outflow from Magnetized Tori of Active Galactic Nuclei. , 843:58, July 2017.

J. Clavel, W. Wamsteker, and I. S. Glass. Hot Dust on the Outskirts of the Broad-Line Region in Fairall 9. , 337:236, February 1989.

F. Combes, S. García-Burillo, A. Audibert, L. Hunt, A. Eckart, S. Aalto, V. Casasola, F. Boone, M. Krips, S. Viti, K. Sakamoto, S. Muller, K. Dasyra, P. van der Werf, and S. Martin. ALMA observations of molecular tori around massive black holes. , 623: A79, March 2019.

F. Combes, S. García-Burillo, V. Casasola, L. Hunt, M. Krips, A. J. Baker, F. Boone, A. Eckart, I. Marquez, R. Neri, E. Schinnerer, and L. J. Tacconi. ALMA observations of feeding and feedback in nearby Seyfert galaxies: an AGN-driven outflow in NGC 1433. , 558:A124, October 2013.

F. Combes, S. García-Burillo, V. Casasola, L. K. Hunt, M. Krips, A. J. Baker, F. Boone, A. Eckart, I. Marquez, R. Neri, E. Schinnerer, and L. J. Tacconi. ALMA reveals the feeding of the Seyfert 1 nucleus in NGC 1566. , 565:A97, May 2014.

M. Dehghanian, G. J. Ferland, B. M. Peterson, G. A. Kriss, K. T. Korista, M. Chatzikos, F. Guzmán, N. Arav, G. De Rosa, M. R. Goad, M. Mehdipour, and P. A. M. van Hoof. A Wind-based Unification Model for NGC 5548: Spectral Holidays, Nondisk Emission, and Implications for Changing-look Quasars. , 882(2):L30, September 2019.

A. Dorodnitsyn, T. Kallman, and G. S. Bisnovatyi-Kogan. AGN Obscuration through Dusty, Infrared-dominated Flows. II. Multidimensional, Radiation-hydrodynamics Modeling. , 747:8, March 2012.

A. Dorodnitsyn, T. Kallman, and D. Proga. Parsec-scale Accretion and Winds Irradiated by a Quasar. , 819:115, March 2016.

Sergei Dyda, Randall Dannen, Tim Waters, and Daniel Proga. Irradiation of astrophysical objects - SED and flux effects on thermally driven winds. , 467(4):4161–4173, June 2017.

J. Ebrero, G. A. Kriss, J. S. Kaastra, and J. C. Ely. Discovery of a fast, broad, transient outflow in NGC 985. , 586:A72, February 2016.

Moshe Elitzur and Isaac Shlosman. The AGN-obscuring Torus: The End of the "Doughnut" Paradigm? , 648(2):L101–L104, September 2006.

M. Elvis. A Structure for Quasars. , 545:63–76, December 2000.

Jonas Eriksson. Evaluation of sph for hydrodynamic modeling, using dualsphysics, 2018.

A. C. Fabian. Observational Evidence of Active Galactic Nuclei Feedback. , 50:455–489, September 2012.

A. C. Fabian, R. V. Vasudevan, and P. Gandhi. The effect of radiation pressure on dusty absorbing gas around active galactic nuclei. , 385(1):L43–L47, March 2008.

B. L. Fanaroff and J. M. Riley. The morphology of extragalactic radio sources of high and low luminosity. , 167:31P–36P, May 1974.

G. J. Ferland, M. Chatzikos, F. Guzmán, M. L. Lykins, P. A. M. van Hoof, R. J. R. Williams, N. P. Abel, N. R. Badnell, F. P. Keenan, R. L. Porter, and P. C. Stancil. The 2017 Release Cloudy. *Revista Mexicana de Astronomia y Astrofisica*, 53:385–438, October 2017.

G. J. Ferland, R. L. Porter, P. A. M. van Hoof, R. J. R. Williams, N. P. Abel, M. L. Lykins, G. Shaw, W. J. Henney, and P. C. Stancil. The 2013 Release of Cloudy. , 49: 137–163, April 2013.

Laura Ferrarese and David Merritt. A Fundamental Relation between Supermassive Black Holes and Their Host Galaxies. , 539(1):L9–L12, August 2000.

Jack F. Gallimore, Moshe Elitzur, Roberto Maiolino, Alessandro Marconi, Christopher P. O'Dea, Dieter Lutz, Stefi A. Baum, Robert Nikutta, C. M. V. Impellizzeri,

Richard Davies, Amy E. Kimball, and Eleonora Sani. High-velocity Bipolar Molecular Emission from an AGN Torus. , 829(1):L7, September 2016a.

Jack F. Gallimore, Moshe Elitzur, Roberto Maiolino, Alessandro Marconi, Christopher P. O'Dea, Dieter Lutz, Stefi A. Baum, Robert Nikutta, C. M. V. Impellizzeri, Richard Davies, Amy E. Kimball, and Eleonora Sani. High-velocity Bipolar Molecular Emission from an AGN Torus. , 829(1):L7, September 2016b.

S. García-Burillo, F. Combes, C. Ramos Almeida, A. Usero, M. Krips, A. Alonso-Herrero, S. Aalto, V. Casasola, L. K. Hunt, S. Martín, S. Viti, L. Colina, F. Costagliola, A. Eckart, A. Fuente, C. Henkel, I. Márquez, R. Neri, E. Schinnerer, L. J. Tacconi, and P. P. van der Werf. ALMA Resolves the Torus of NGC 1068: Continuum and Molecular Line Emission. , 823:L12, May 2016.

S. García-Burillo, F. Combes, A. Usero, S. Aalto, M. Krips, S. Viti, A. Alonso-Herrero, L. K. Hunt, E. Schinnerer, A. J. Baker, F. Boone, V. Casasola, L. Colina, F. Costagliola, A. Eckart, A. Fuente, C. Henkel, A. Labiano, S. Martín, I. Márquez, S. Muller, P. Planesas, C. Ramos Almeida, M. Spaans, L. J. Tacconi, and P. P. van der Werf. Molecular line emission in NGC 1068 imaged with ALMA. I. An AGN-driven outflow in the dense molecular gas. , 567:A125, July 2014.

J. García-González, A. Alonso-Herrero, S. F. Hönig, A. Hernán-Caballero, C. Ramos Almeida, N. A. Levenson, P. F. Roche, O. González-Martín, C. Packham, and M. Kishimoto. A mid-infrared statistical investigation of clumpy torus model predictions. , 470:2578–2598, September 2017.

C. M. Gaskell and E. S. Klimek. Variability of Active Galactic Nuclei from Optical to X-ray Regions. *Astronomical and Astrophysical Transactions*, 22(4-5):661–680, August 2003.

Karl Gebhardt, Ralf Bender, Gary Bower, Alan Dressler, S. M. Faber, Alexei V. Filippenko, Richard Green, Carl Grillmair, Luis C. Ho, John Kormendy, Tod R. Lauer, John Magorrian, Jason Pinkney, Douglas Richstone, and Scott Tremaine. A Relationship between Nuclear Black Hole Mass and Galaxy Velocity Dispersion. , 539(1): L13–L16, August 2000.

N. Gehrels, G. Chincarini, P. Giommi, K. O. Mason, J. A. Nousek, A. A. Wells, N. E. White, S. D. Barthelmy, D. N. Burrows, L. R. Cominsky, K. C. Hurley, F. E. Marshall, P. Mészáros, P. W. A. Roming, L. Angelini, L. M. Barbier, T. Belloni, S. Campana, P. A. Caraveo, M. M. Chester, O. Citterio, T. L. Cline, M. S. Cropper, J. R. Cummings, A. J. Dean, E. D. Feigelson, E. E. Fenimore, D. A. Frail, A. S. Fruchter, G. P. Garmire, K. Gendreau, G. Ghisellini, J. Greiner, J. E. Hill, S. D. Hunsberger, H. A. Krimm, S. R. Kulkarni, P. Kumar, F. Lebrun, N. M. Lloyd-Ronning, C. B. Markwardt, B. J. Mattson, R. F. Mushotzky, J. P. Norris, J. Osborne, B. Paczynski, D. M. Palmer, H. S. Park, A. M. Parsons, J. Paul, M. J. Rees, C. S. Reynolds, J. E. Rhoads, T. P. Sasseen, B. E. Schaefer, A. T. Short, A. P. Smale, I. A. Smith, L. Stella, G. Tagliaferri, T. Takahashi, M. Tashiro, L. K. Townsley, J. Tueller, M. J. L. Turner, M. Vietri, W. Voges, M. J. Ward, R. Willingale, F. M. Zerbi, and W. W. Zhang. The Swift Gamma-Ray Burst Mission. , 611(2):1005–1020, August 2004.

Gravity Collaboration, J. Dexter, J. Shangguan, S. Hönig, M. Kishimoto, D. Lutz, H. Netzer, R. Davies, E. Sturm, O. Pfuhl, A. Amorim, M. Bauböck, W. Brandner, Y. Clénet, P. T. de Zeeuw, A. Eckart, F. Eisenhauer, N. M. Förster Schreiber, F. Gao, P. J. V. Garcia, R. Genzel, S. Gillessen, D. Gratadour, A. Jiménez-Rosales, S. Lacour, F. Millour, T. Ott, T. Paumard, K. Perraut, G. Perrin, B. M. Peterson, P. O. Petrucci, M. A. Prieto, D. Rouan, M. Schartmann, T. Shimizu, A. Sternberg, O. Straub, C. Straubmeier, L. J. Tacconi, K. Tristram, P. Vermot, I. Waisberg, F. Widmann, and J. Woillez. The resolved size and structure of hot dust in the immediate vicinity of AGN. , 635:A92, March 2020.

L. J. Greenhill, R. S. Booth, S. P. Ellingsen, J. R. Herrnstein, D. L. Jauncey, P. M. McCulloch, J. M. Moran, R. P. Norris, J. E. Reynolds, and A. K. Tzioumis. A Warped Accretion Disk and Wide-Angle Outflow in the Inner Parsec of the Circinus Galaxy. , 590:162–173, June 2003.

L. J. Greenhill and C. R. Gwinn. VLBI Imaging of Water Maser Emission from a Nuclear Disk in NGC 1068. , 248(1-2):261–267, February 1997.

L. J. Greenhill, C. R. Gwinn, R. Antonucci, and R. Barvainis. VLBI Imaging of Water Maser Emission from the Nuclear Torus of NGC 1068. , 472:L21, November 1996.

P. W. Guilbert and M. J. Rees. 'Cold' material in non-thermal sources. , 233:475–484, July 1988.

Tanmayee Gupte. Smoothed particle hydrodynamics. 2018.

J. P. Halpern. Variable X-ray absorption in the QSO MR 2251-178. , 281:90–94, June 1984.

Fiona A. Harrison, William W. Craig, Finn E. Christensen, Charles J. Hailey, William W. Zhang, Steven E. Boggs, Daniel Stern, W. Rick Cook, Karl Forster, Paolo Giommi, Brian W. Grefenstette, Yunjin Kim, Takao Kitaguchi, Jason E. Koglin, Kristin K. Madsen, Peter H. Mao, Hiromasa Miyasaka, Kaya Mori, Matteo Perri, Michael J. Pivovaroff, Simonetta Puccetti, Vikram R. Rana, Niels J. Westergaard, Jason Willis, Andreas Zoglauer, Hongjun An, Matteo Bachetti, Nicolas M. Barrière, Eric C. Bellm, Varun Bhalerao, Nicolai F. Brejnholt, Felix Fuerst, Carl C. Liebe, Craig B. Markwardt, Melania Nynka, Julia K. Vogel, Dominic J. Walton, Daniel R. Wik, David M. Alexander, Lynn R. Cominsky, Ann E. Hornschemeier, Allan Hornstrup, Victoria M. Kaspi, Greg M. Madejski, Giorgio Matt, Silvano Molendi, David M. Smith, John A. Tomsick, Marco Ajello, David R. Ballantyne, Mislav Baloković, Didier Barret, Franz E. Bauer, Roger D. Blandford, W. Niel Brandt, Laura W. Brenneman, James Chiang, Deepto Chakrabarty, Jerome Chenevez, Andrea Comastri, Francois Dufour, Martin Elvis, Andrew C. Fabian, Duncan Farrah, Chris L. Fryer, Eric V. Gotthelf, Jonathan E. Grindlay, David J. Helfand, Roman Krivonos, David L. Meier, Jon M. Miller, Lorenzo Natalucci, Patrick Ogle, Eran O. Ofek, Andrew Ptak, Stephen P. Reynolds, Jane R. Rigby, Gianpiero Tagliaferri, Stephen E. Thorsett, Ezequiel Treister, and C. Megan Urry. The Nuclear Spectroscopic Telescope Array (NuSTAR) High-energy X-Ray Mission. , 770(2):103, June 2013.

S. F. Hönig. Redefining the torus: A unifying view of AGN in the infrared and sub-mm. *arXiv e-prints*, September 2019.

S. F. Hönig and T. Beckert. Active galactic nuclei dust tori at low and high luminosities. , 380(3):1172–1176, September 2007.

S. F. Hönig and M. Kishimoto. Constraining properties of dusty environments by infrared variability. , 534:A121, October 2011.

S. F. Hönig and M. Kishimoto. Dusty Winds in Active Galactic Nuclei: Reconciling Observations with Models. , 838:L20, April 2017.

S. F. Hönig, M. Kishimoto, R. Antonucci, A. Marconi, M. A. Prieto, K. Tristram, and G. Weigelt. Parsec-scale Dust Emission from the Polar Region in the Type 2 Nucleus of NGC 424. , 755:149, August 2012.

S. F. Hönig, M. Kishimoto, K. R. W. Tristram, M. A. Prieto, P. Gandhi, D. Asmus, R. Antonucci, L. Burtscher, W. J. Duschl, and G. Weigelt. Dust in the Polar Region as a Major Contributor to the Infrared Emission of Active Galactic Nuclei. , 771:87, July 2013.

Sebastian F. Hönig. *Tori, Discs, and Winds: The First Ten Years of AGN Interferometry*, volume 439 of *Astrophysics and Space Science Library*, page 95. 2016.

Philip F. Hopkins. A new class of accurate, mesh-free hydrodynamic simulation methods. , 450(1):53–110, June 2015.

Masatoshi Imanishi, Kouichiro Nakanishi, and Takuma Izumi. ALMA HCN and HCO+ J =3-2 Observations of Optical Seyfert and Luminous Infrared Galaxies: Confirmation of Elevated HCN-to-HCO+ Flux Ratios in AGNs. , 152(6):218, December 2016.

Masatoshi Imanishi, Kouichiro Nakanishi, Takuma Izumi, and Keiichi Wada. ALMA Reveals an Inhomogeneous Compact Rotating Dense Molecular Torus at the NGC 1068 Nucleus. , 853(2):L25, February 2018.

C. M. Violette Impellizzeri, Jack F. Gallimore, Stefi A. Baum, Moshe Elitzur, Richard Davies, Dieter Lutz, Roberto Maiolino, Alessandro Marconi, Robert Nikutta, Christopher P. O'Dea, and Eleonora Sani. Counter-rotation and High-velocity Outflow in the Parsec-scale Molecular Torus of NGC 1068. , 884(2):L28, October 2019.

W. Ishibashi. AGN anisotropic radiative feedback set by black hole spin. , 495(2): 2515–2523, May 2020.

W. Ishibashi, A. C. Fabian, C. Ricci, and A. Celotti. Revisiting the 'forbidden' region: AGN radiative feedback with radiation trapping. , 479(3):3335–3342, September 2018.

Z. Ivezic and M. Elitzur. Self-similarity and scaling behaviour of infrared emission from radiatively heated dust - I. Theory. , 287:799–811, June 1997.

Željko Ivezić, Kristen Menou, Gillian R. Knapp, Michael A. Strauss, Robert H. Lupton, Daniel E. Vanden Berk, Gordon T. Richards, Christy Tremonti, Michael A. Weinstein, Scott Anderson, Neta A. Bahcall, Robert H. Becker, Mariangela Bernardi, Michael Blanton, Daniel Eisenstein, Xiaohui Fan, Douglas Finkbeiner, Kristian Finlator, Joshua Frieman, James E. Gunn, Pat B. Hall, Rita S. J. Kim, Ali Kinkhabwala, Vijay K. Narayanan, Constance M. Rockosi, David Schlegel, Donald P. Schneider, Iskra Strateva, Mark SubbaRao, Aniruddha R. Thakar, Wolfgang Voges, Richard L. White, Brian Yanny, Jonathan Brinkmann, Mamoru Doi, Masataka Fukugita, Gregory S. Hennessy, Jeffrey A. Munn, Robert C. Nichol, and Donald G. York. Optical and Radio Properties of Extragalactic Sources Observed by the FIRST Survey and the Sloan Digital Sky Survey. , 124(5):2364–2400, November 2002.

F. Jansen, D. Lumb, B. Altieri, J. Clavel, M. Ehle, C. Erd, C. Gabriel, M. Guainazzi, P. Gondoin, R. Much, R. Munoz, M. Santos, N. Schartel, D. Texier, and G. Vacanti. XMM-Newton observatory. I. The spacecraft and operations. , 365:L1–L6, January 2001.

T. W. Jones, S. L. O'dell, and W. A. Stein. Physics of Compact Nonthermal Sources. I. Theory of Radiation Processes. , 188:353–368, March 1974.

J. S. Kaastra, G. A. Kriss, M. Cappi, M. Mehdipour, P. O. Petrucci, K. C. Steenbrugge, N. Arav, E. Behar, S. Bianchi, R. Boissay, G. Brand uardi-Raymont, C. Chamberlain, E. Costantini, J. C. Ely, J. Ebrero, L. Di Gesu, F. A. Harrison, S. Kaspi, J. Malzac, B. De Marco, G. Matt, K. Nand ra, S. Paltani, R. Person, B. M. Peterson, C. Pinto, G. Ponti, F. Pozo Nuñez, A. De Rosa, H. Seta, F. Ursini, C. P. de Vries, D. J. Walton, and M. Whewell. A fast and long-lived outflow from the supermassive black hole in NGC 5548. *Science*, 345(6192):64–68, July 2014.

J. S. Kaastra, R. Mewe, D. A. Liedahl, S. Komossa, and A. C. Brinkman. X-ray absorption lines in the Seyfert 1 galaxy NGC 5548 discovered with Chandra-LETGS. , 354:L83–L86, February 2000.

Shai Kaspi, Paul S. Smith, Hagai Netzer, Dan Maoz, Buell T. Jannuzi, and Uriel Giveon. Reverberation Measurements for 17 Quasars and the Size-Mass-Luminosity Relations in Active Galactic Nuclei. , 533(2):631–649, April 2000.

K. Kellermann, R. Sramek, D. Shaffer, R. Green, and M. Schmidt. Radio Emission from Optically Selected Quasars. In G. Swarup and V. K. Kapahi, editors, *Quasars*, volume 119, page 95, January 1986.

E. Y. Khachikian and D. W. Weedman. An atlas of Seyfert galaxies. , 192:581–589, September 1974.

Andrew King. Black Holes, Galaxy Formation, and the M_{BH}-σ Relation. , 596(1): L27–L29, October 2003.

M. Kishimoto, S. F. Hönig, R. Antonucci, R. Barvainis, T. Kotani, K. R. W. Tristram, G. Weigelt, and K. Levin. The innermost dusty structure in active galactic nuclei as probed by the Keck interferometer. , 527:A121, March 2011a.

M. Kishimoto, S. F. Hönig, R. Antonucci, F. Millour, K. R. W. Tristram, and G. Weigelt. Mapping the radial structure of AGN tori. , 536:A78, December 2011b.

M. Kishimoto, S. F. Hönig, T. Beckert, and G. Weigelt. The innermost region of AGN tori: implications from the HST/NICMOS type 1 point sources and near-IR reverberation. , 476:713–721, December 2007.

John Kormendy and Luis C. Ho. Coevolution (Or Not) of Supermassive Black Holes and Host Galaxies: Supplemental Material. *arXiv e-prints*, page arXiv:1308.6483, August 2013.

G. A. Kriss, M. Mehdipour, J. S. Kaastra, A. Rau, J. Bodensteiner, R. Plesha, N. Arav, E. Behar, S. Bianchi, G. Branduardi-Raymont, M. Cappi, E. Costantini, B. De Marco, L. Di Gesu, J. Ebrero, S. Kaspi, J. Mao, R. Middei, T. Miller, S. Paltani, U. Peretz,

B. M. Peterson, P. O. Petrucci, G. Ponti, F. Ursini, D. J. Walton, and X. Xu. HST/-COS observations of the newly discovered obscuring outflow in NGC 3783. , 621:A12, January 2019.

J. H. Krolik. AGN Obscuring Tori Supported by Infrared Radiation Pressure. , 661: 52–59, May 2007.

J. H. Krolik and M. C. Begelman. An X-ray heated wind in NGC 1068. , 308:L55–L58, September 1986.

J. H. Leftley, K. R. W. Tristram, S. F. Hönig, M. Kishimoto, D. Asmus, and P. Gandhi. New Evidence for the Dusty Wind Model: Polar Dust and a Hot Core in the Type-1 Seyfert ESO 323-G77. , 862:17, July 2018.

A. L. Longinotti, Y. Krongold, G. A. Kriss, J. Ely, L. Gallo, D. Grupe, S. Komossa, S. Mathur, and A. Pradhan. The Rise of an Ionized Wind in the Narrow-line Seyfert 1 Galaxy Mrk 335 Observed by XMM-Newton and HST. , 766(2):104, April 2013.

N. Lopez-Gonzaga, D. Asmus, F. E. Bauer, K. R. W. Tristram, L. Burtscher, A. Marinucci, G. Matt, and F. A. Harrison. VizieR Online Data Catalog: NGC1068 interferometric mid-IR measurements (Lopez-Gonzaga+, 2017). *VizieR Online Data Catalog*, pages J/A+A/602/A78, Jun 2017.

N. López-Gonzaga, L. Burtscher, K. R. W. Tristram, K. Meisenheimer, and M. Schartmann. Mid-infrared interferometry of 23 AGN tori: On the significance of polar-elongated emission. , 591:A47, June 2016.

N. Lopez-Gonzaga, W. Jaffe, L. Burtscher, K. R. W. Tristram, and K. Meisenheimer. VizieR Online Data Catalog: NGC1068 MIDI/VLTI observations (Lopez-Gonzaga+, 2014). *VizieR Online Data Catalog*, pages J/A+A/565/A71, Mar 2014.

D. Lynden-Bell. Galactic Nuclei as Collapsed Old Quasars. , 223(5207):690–694, August 1969.

John Magorrian, Scott Tremaine, Douglas Richstone, Ralf Bender, Gary Bower, Alan Dressler, S. M. Faber, Karl Gebhardt, Richard Green, Carl Grillmair, John Kormendy,

and Tod Lauer. The Demography of Massive Dark Objects in Galaxy Centers. , 115 (6):2285–2305, June 1998.

R. Maiolino, G. Risaliti, M. Salvati, P. Pietrini, G. Torricelli-Ciamponi, M. Elvis, G. Fabbiano, V. Braito, and J. Reeves. "Comets" orbiting a black hole. , 517:A47, July 2010.

F. Marin and R. W. Goosmann. A structure for quasars under the scope of polarization - I. The UV/optical polarization dichotomy of type-1 and type-2 AGN. , 436(3): 2522–2534, December 2013.

J. S. Mathis, W. Rumpl, and K. H. Nordsieck. The size distribution of interstellar grains. , 217:425–433, October 1977.

J. N. McCallum, S. P. Ellingsen, J. E. J. Lovell, C. J. Phillips, and J. E. Reynolds. Probing the microarcsecond structure of the Circinus megamasers through diffractive interstellar scintillation. , 392(4):1339–1362, February 2009.

M. Mehdipour, J. S. Kaastra, G. A. Kriss, N. Arav, E. Behar, S. Bianchi, G. Branduardi-Raymont, M. Cappi, E. Costantini, J. Ebrero, L. Di Gesu, S. Kaspi, J. Mao, B. De Marco, G. Matt, S. Paltani, U. Peretz, B. M. Peterson, P. O. Petrucci, C. Pinto, G. Ponti, F. Ursini, C. P. de Vries, and D. J. Walton. Chasing obscuration in type-I AGN: discovery of an eclipsing clumpy wind at the outer broad-line region of NGC 3783. , 607:A28, October 2017.

A. Merloni, A. Bongiorno, M. Brusa, K. Iwasawa, V. Mainieri, B. Magnelli, M. Salvato, S. Berta, N. Cappelluti, A. Comastri, F. Fiore, R. Gilli, A. Koekemoer, E. Le Floc'h, E. Lusso, D. Lutz, T. Miyaji, F. Pozzi, L. Riguccini, D. J. Rosario, J. Silverman, M. Symeonidis, E. Treister, C. Vignali, and G. Zamorani. The incidence of obscuration in active galactic nuclei. , 437(4):3550–3567, February 2014.

J. S. Miller and R. W. Goodrich. Spectropolarimetry of High-Polarization Seyfert 2 Galaxies and Unified Seyfert Theories. , 355:456, June 1990.

D. Namekata and M. Umemura. Sub-parsec-scale dynamics of a dusty gas disc exposed to anisotropic AGN radiation with frequency-dependent radiative transfer. , 460: 980–1018, July 2016.

D. Namekata, M. Umemura, and K. Hasegawa. On the evolution of gas clouds exposed to AGN radiation - I. Three-dimensional radiation hydrodynamic simulations. , 443 (3):2018–2048, September 2014.

M. Nenkova, Ž. Ivezić, and M. Elitzur. Dust Emission from Active Galactic Nuclei. , 570:L9–L12, May 2002.

Hagai Netzer. Quasar discs. II - A composite model for the broad-line region. , 225: 55–72, March 1987a.

Hagai Netzer. Quasar discs. II - A composite model for the broad-line region. , 225: 55–72, March 1987b.

I. D. Novikov and K. S. Thorne. Astrophysics of black holes. In *Black Holes (Les Astres Occlus)*, pages 343–450, January 1973.

D. E. Osterbrock. Seyfert galaxies with weak broad H alpha emission lines. , 249: 462–470, October 1981.

Donald E. Osterbrock and Gary J. Ferland. *Astrophysics of gaseous nebulae and active galactic nuclei*. 2006.

Jeremiah P. Ostriker, Ena Choi, Luca Ciotti, Gregory S. Novak, and Daniel Proga. Momentum Driving: Which Physical Processes Dominate Active Galactic Nucleus Feedback? , 722(1):642–652, October 2010.

Edward A. Pier and Julian H. Krolik. Infrared Spectra of Obscuring Dust Tori around Active Galactic Nuclei. II. Comparison with Observations. , 418:673, December 1993.

David Raban, Walter Jaffe, Huub Röttgering, Klaus Meisenheimer, and Konrad R. W. Tristram. Resolving the obscuring torus in NGC 1068 with the power of infrared interferometry: revealing the inner funnel of dust. , 394(3):1325–1337, April 2009.

Cristina Ramos Almeida and Claudio Ricci. Nuclear obscuration in active galactic nuclei. *Nature Astronomy*, 1:679–689, October 2017a.

Cristina Ramos Almeida and Claudio Ricci. Nuclear obscuration in active galactic nuclei. *Nature Astronomy*, 1:679–689, October 2017b.

M. J. Rees, J. I. Silk, M. W. Werner, and N. C. Wickramasinghe. Infrared Radiation from Dust in Seyfert Galaxies. , 223(5208):788–791, August 1969.

C. S. Reynolds. An X-ray spectral study of 24 type 1 active galactic nuclei. , 286(3): 513–537, April 1997.

C. Ricci, B. Trakhtenbrot, M. J. Koss, Y. Ueda, K. Schawinski, K. Oh, I. Lamperti, R. Mushotzky, E. Treister, L. C. Ho, A. Weigel, F. E. Bauer, S. Paltani, A. C. Fabian, Y. Xie, and N. Gehrels. The close environments of accreting massive black holes are shaped by radiative feedback. , 549:488–491, September 2017.

C. Ricci, Y. Ueda, M. J. Koss, B. Trakhtenbrot, F. E. Bauer, and P. Gandhi. Compton-thick Accretion in the Local Universe. , 815(1):L13, December 2015.

G. Risaliti and M. Elvis. *A Panchromatic View of AGN*, volume 308 of *Astrophysics and Space Science Library*, page 187. 2004.

G. Risaliti, M. Elvis, G. Fabbiano, A. Baldi, A. Zezas, and M. Salvati. Occultation Measurement of the Size of the X-Ray-emitting Region in the Active Galactic Nucleus of NGC 1365. , 659(2):L111–L114, April 2007.

D. B. Sanders, E. S. Phinney, G. Neugebauer, B. T. Soifer, and K. Matthews. Continuum Energy Distributions of Quasars: Shapes and Origins: Erratum. , 357:291, July 1990.

M. Schmidt. 3C 273 : A Star-Like Object with Large Red-Shift. , 197(4872):1040, March 1963.

Carl K. Seyfert. Nuclear Emission in Spiral Nebulae. , 97:28, January 1943.

N. I. Shakura and R. A. Sunyaev. Reprint of 1973A&A....24..337S. Black holes in binary systems. Observational appearance. , 500:33–51, June 1973.

Joseph Silk and Martin J. Rees. Quasars and galaxy formation. , 331:L1–L4, March 1998.

M. Stalevski, D. Asmus, and K. R. W. Tristram. Dissecting the active galactic nucleus in Circinus - I. Peculiar mid-IR morphology explained by a dusty hollow cone. , 472: 3854–3870, December 2017.

M. Stalevski, K. R. W. Tristram, and D. Asmus. Dissecting the active galactic nucleus in Circinus - II. A thin dusty disc and a polar outflow on parsec scales. , 484:3334–3355, April 2019.

D. P. Summons, P. Arévalo, I. M. McHardy, P. Uttley, and A. Bhaskar. Timing evidence in determining the accretion state of the Seyfert galaxy NGC 3783. , 378(2):649–656, June 2007.

Clive Tadhunter. An introduction to active galactic nuclei: Classification and unification. , 52(6):227–239, August 2008.

Y. Tajima and J. Fukue. Radiative Disk Winds under Radiation Drag II. , 50:483–493, October 1998.

G. Theureau, L. Bottinelli, N. Coudreau-Durand, L. Gouguenheim, N. Hallet, M. Loulergue, G. Paturel, and P. Teerikorpi. Kinematics of the local universe. VII. New 21-cm line measurements of 2112 galaxies. , 130:333–339, June 1998.

Konrad R. W. Tristram, Leonard Burtscher, Walter Jaffe, Klaus Meisenheimer, Sebastian F. Hönig, Makoto Kishimoto, Marc Schartmann, and Gerd Weigelt. The dusty torus in the Circinus galaxy: a dense disk and the torus funnel. , 563:A82, Mar 2014.

C. M. Urry. Grand Unification of Active Galaxies. In *American Astronomical Society Meeting Abstracts #202*, volume 202 of *American Astronomical Society Meeting Abstracts*, page 22.01, May 2003.

C. Megan Urry and Paolo Padovani. Unified Schemes for Radio-Loud Active Galactic Nuclei. , 107:803, September 1995.

Daniel E. Vanden Berk, Gordon T. Richards, Amanda Bauer, Michael A. Strauss, Donald P. Schneider, Timothy M. Heckman, Donald G. York, Patrick B. Hall, Xiaohui Fan, G. R. Knapp, Scott F. Anderson, James Annis, Neta A. Bahcall, Mariangela Bernardi, John W. Briggs, J. Brinkmann, Robert Brunner, Scott Burles, Larry Carey, Francisco J. Castander, A. J. Connolly, J. H. Crocker, István Csabai, Mamoru Doi, Douglas Finkbeiner, Scott Friedman, Joshua A. Frieman, Masataka Fukugita, James E. Gunn, G. S. Hennessy, Željko Ivezić, Stephen Kent, Peter Z. Kunszt, D. Q. Lamb, R. French

Leger, Daniel C. Long, Jon Loveday, Robert H. Lupton, Avery Meiksin, Aronne Merelli, Jeffrey A. Munn, Heidi Jo Newberg, Matt Newcomb, R. C. Nichol, Russell Owen, Jeffrey R. Pier, Adrian Pope, Constance M. Rockosi, David J. Schlegel, Walter A. Siegmund, Stephen Smee, Yehuda Snir, Chris Stoughton, Christopher Stubbs, Mark SubbaRao, Alexander S. Szalay, Gyula P. Szokoly, Christy Tremonti, Alan Uomoto, Patrick Waddell, Brian Yanny, and Wei Zheng. Composite Quasar Spectra from the Sloan Digital Sky Survey. , 122(2):549–564, August 2001.

Marta Venanzi, Sebastian Hönig, and David Williamson. The Role of Infrared Radiation Pressure in Shaping Dusty Winds in AGNs. , 900(2):174, September 2020.

K. Wada, M. Schartmann, and R. Meijerink. Multi-phase Nature of a Radiation-driven Fountain with Nuclear Starburst in a Low-mass Active Galactic Nucleus. , 828:L19, September 2016.

D. W. Weedman. Seyfert galaxies. , 15:69–95, January 1977.

D. Williamson, S. Hönig, and M. Venanzi. 3D Radiation Hydrodynamics of a Dynamical Torus. , 876:137, May 2019.

David Williamson, Sebastian Hönig, and Marta Venanzi. Radiation Hydrodynamics Models of Active Galactic Nuclei: Beyond the Central Parsec. , 897(1):26, July 2020.